

**COALESCENCE AND EVAPORATION DYNAMICS
OF MULTIPLE DROPLET IMPINGEMENT OVER A
HEATED SURFACE**

A THESIS

submitted by

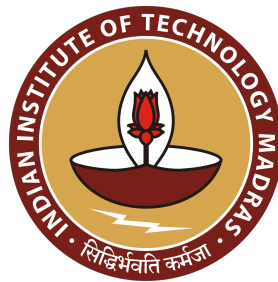
GUGGILLA GANESH

for the award of the degree

of

DOCTOR OF PHILOSOPHY

jointly with



**DEPARTMENT OF MECHANICAL ENGINEERING
INDIAN INSTITUTE OF TECHNOLOGY MADRAS
CURTIN UNIVERSITY AUSTRALIA**

MAY 2020

*Small steps in the right direction can turn out
to be the biggest step of your life*

– Anonymous

Dedicated to:

My Parents, Teachers and Friends

THESIS CERTIFICATE

This is to certify that the thesis titled **Coalescence and Evaporation Dynamics of Multiple Droplet Impingement over a Heated Surface**, submitted by **Guggilla Ganesh**, to the Indian Institute of Technology Madras, for the award of the degree of **Doctor of Philosophy**, is a bonafide record of the research work done by him under our supervision. The contents of this thesis, in full or in parts, have not been submitted to any other Institute or University for the award of any degree or diploma.

Dr. Arvind Pattamatta
Research Advisor
Associate Professor
Dept. of Mechanical Engineering
IIT Madras, Chennai-600036

Dr. Ramesh Narayanaswamy
Research Advisor
Associate Professor
Dept. of Mechanical Engineering
Curtin University, Bentley WA-6102,
Australia

Place: Chennai

Date: 26 May 2020

ACKNOWLEDGEMENTS

The journey of research is a sophisticated one, the achievements and the glory are momentary, while the curiosity is immortal. It is a privilege to talk about my journey of research and honor the people, without whose support, it would have been impossible to reach this stage.

First and foremost, I sincerely express my deep gratitude to my research advisors **Dr. Arvind Pattamatta** and **Dr. Ramesh Narayanaswamy** for the joint Ph.D. opportunity and visit to Curtin University. It is a fortunate blessing for me to receive experienced and enriched guidance from them. Their scholarly advice on academic matters, sympathetic understanding as well as friendly and parental care on personal matters have helped me remarkably in the progress of my research work with maintaining a calm and condensed psyche.

I want to express my gratitude to **Dr. Peter Stephan** from Technical University (TU) of Darmstadt, for providing me the opportunity to visit their lab. My special thanks to **Mr. Achim Bender**, Doctoral student, TU Darmstadt for his fruitful discussions on the numerical modelling. I want to acknowledge the financial support received from the **Indo-German Centre for Sustainability (IGCS)** for the TU Darmstadt visit.

I extend my heartwarming thanks to all my Doctoral Committee members **Dr. Prasad Patnaik B S V**, **Dr. Sateesh Gedupudi**, and **Dr. Srikrishna Sahu**, whose suggestions at various stages were very worthwhile.

The show never runs without a backstage support, I present my warm thanks to the technical support I received from Curtin University lab technicians **Mr. David Collier**, **Mr. Graeme Watson**, **Mr. Hamish Thava Narayanasamy**, and HTTP lab technicians **Mr. Sagaya Rajesh**, **Mr. Prabhakaran**, **Mr. Surendra** and **Mr. Deivasigamani**.

A comfortable workplace is like a flower-pot which nurtures the budding ideas. In this regard I was very much fortunate to have **Dr. Sangamesh.C.Godi**, **Dr. Sampath kumar Chinige**, **Kalichetty Srinivasa Sagar**, **Tejaswi Jyosula**, **Desh Deepak Dixit**, **A.R.Akash**, **Anand Prasanna**, **Pranit Joshi** and **Anand Takawale** as my research colleagues. Their motivation, advices and moral support during my Ph.D. have kept me strong in my belief. My sincere thanks to **Dr. Vishal Chaugule** and **Mr. Paw Chen Min (Tristan)** of Curtin University, and **Mr. Akhil Chowdary** of IIT Madras for their invaluable assistance during the experimental

studies.

There are people worthwhile to mention, when I remember my stay in IIT. I enjoyed awesome company of **Manideep Nomula, Nikhil Papetla, Dheeresh Reddi, Bharat, Mallikarjun Rao** and **Anjith Kumar** during food, outing and sports. I express my cordial thanks to them for their support and companionship.

My sincere thanks to **Aswathy Asokan Ajitha** and **Silpa Sangeeth L R** for always listening, encouraging and their great support. I am fortunate to have **Jayita Chakraborty** as a friend and companion during the tough times. My special thanks to my well wishers **Swapna Suryavamshi, Jyothsna Inti, Hasitha Jammi** and **Vijaya Lakshmi** for being there for me during this journey.

My sincere thanks to **Dr. Kartik Regulagadda** for his constant support and valuable suggestions through out the work.

In addition, I want to thank all my friends of IIT madras **Akhil, Dr.Harish, Pramod, Yugandhar, Nagaraju, Sandeep** and **Hari Srinivas** for their moral support during my stay.

Words would fall short to express my affectionate thanks and regards to my parents **Shri Ramanna Guggilla** and **Smt. Dhana Lakshmi Guggilla** for their constant support and warm care throughout my life and especially during my Ph.D. I want to thank my dearest brother **Venkatesh Guggilla** and my sister **Mounika Guggilla** for their adoration and support, which has helped me to stay constantly energetic during my Ph.D.

I express my sincere gratitude to all who have helped me in this venture.

GUGGILLA GANESH

ABSTRACT

KEYWORDS: Drop-on-drop impact; heated surface; evaporation; wetting surfaces; spread dynamics; droplet heat transfer; concentric droplet impact

As miniaturization of electronic components is rapidly increasing, efficient cooling techniques are a matter of concern in recent years. One such cooling mechanism is spray cooling, which has numerous industrial applications. To comprehend the spray cooling operation, the interpretation of relevant basic processes such as single droplet impact, drop coalescence and drop-on-drop collisions, etc., is required. The present work investigates the drop-on-drop impact of liquid droplets over a heated surface, both experimentally and numerically.

Initially, a numerical model is implemented in opensource CFD software OpenFOAM to simulate the droplet impact over the heated surface in a saturated vapour (single component) medium. Contact line evaporation near three-phase contact region and dynamic contact angle motion are considered during the simulations. Two configurations of impingement, single droplet, and drop-on-drop collisions are carried out and, the spread dynamics and heat transfer characteristics are compared for the same impact conditions. Later on, the effect of influential parameters, such as Weber number (We), Bond number (Bo), Jakob number (Ja) and the sessile droplet radius (taken as a radius ratio (R^*) of the sessile drop to impacting droplet), on drop-on-drop impact is studied. Analytical models predicting the maximum spread during the single droplet collision and corresponding input droplet heat transfer are identified from the literature and extended to drop-on-drop impingement

Following this, the experimental investigations of two consecutively impinging droplets over a heated surface are conducted. During the analysis, the phenomenon is perceived as two separate configurations as a single droplet (leading droplet) and drop-on-drop collision (the trailing droplet impact onto the settled leading drop on the surface). The preliminary experiments are carried out using De-ionised water, followed by FC-72

droplet impingement. A thin Inconel foil (thickness = 25 micron) is used as the target surface and is maintained at a constant temperature using a DC supply. The droplet spread is measured from the side-view images using high-speed photography, whereas the heat transfer is obtained by tracking the surface temperature (from the underside) using the Infrared thermography. For fixed impact conditions and droplet flow rate, different boiling regimes are identified based on the droplet heat transfer. During the leading and trailing droplet impingement, a comparison of droplet heat transfer is made in the observed regimes.

Subsequently, a numerical model is implemented in OpenFOAM to carry out the simulations of the droplet impingement over the heated surface in air-vapour (multicomponent) medium. The model is validated using the experimental observations of FC-72 single droplet impact over the heated Inconel surface. Later on, the time interval between the two consecutively impinging droplets is varied, and the effect on the spread and heat transfer characteristics is analysed.

Based on the numerical and experimental investigations, it is observed that the droplet spread and the corresponding heat transfer is affected by the impacting conditions and flow rate. During the drop-on-drop impact, the trailing droplet heat transfer is influenced by the surface area-to-volume ratio (spreading film thickness), the surface pre-cooling by leading droplet, and the droplet's cycle phase when the flow rate is of the order of cycle time. A cycle's time scale is in milliseconds and consists of advancing (spreading) and receding (retracting) phases.

TABLE OF CONTENTS

	Page
ACKNOWLEDGEMENTS	i
ABSTRACT	iii
LIST OF TABLES	viii
LIST OF FIGURES	ix
ABBREVIATIONS	xiv
NOTATION	xv
1 INTRODUCTION	1
1.1 Motivation	1
1.1.1 Droplet impingement: Nomenclature	2
1.1.2 Possible morphologies of droplet impact	4
1.2 Organization of the thesis	6
1.3 Closure	7
2 REVIEW OF LITERATURE	8
2.1 Introduction	8
2.2 Studies on droplet impact over non-heated surfaces	8
2.2.1 Single droplet impingement	9
2.2.2 Multiple droplet impingement	12
2.3 Studies on droplet impact over heated surfaces	14
2.3.1 Single droplet impingement	17
2.3.2 Multiple droplet impingement	20
2.4 Objectives of the present research work	22
2.5 Closure	23

3	NUMERICAL STUDY: DROPLET IMPACT OVER A HEATED SURFACE IN VAPOUR MEDIUM	24
3.1	Introduction	24
3.2	Numerical modelling	24
3.3	Mathematical formulation	25
3.3.1	Evaporation model	26
3.4	Validation of the model	28
3.4.1	Single droplet impact onto heated surface	29
3.4.2	Drop-on-drop impingement upon isothermal surface	30
3.5	Present simulation - Drop-on-drop impact onto heated surfaces	32
3.6	Results and Discussion	34
3.6.1	Drop-on-drop impingement onto heated surface	34
3.6.2	Comparison of drop-on-drop impingement to single drop impingement	36
3.6.3	Effect of influencing parameters on drop-on-drop impingement over heated surfaces	38
3.6.4	Analytical modelling	48
3.7	Closure	52
4	EXPERIMENTAL STUDY: DROPLET IMPACT OVER A HEATED SURFACE IN AIR-VAPOUR MEDIUM	53
4.1	Introduction	53
4.2	Experimental methodology	54
4.2.1	Impingement configuration	55
4.2.2	Image post-processing	56
4.2.3	Infrared image post-processing	58
4.2.4	Experimental methodology: Validation cases	62
4.3	Water droplet impingement	64
4.3.1	Results and Discussion	65
4.3.2	Analytical modelling	78
4.4	FC-72 liquid droplet impingement	84
4.4.1	Results and Discussion	85
4.4.2	Analytical modelling	92
4.5	Closure	93

5	NUMERICAL STUDY: DROPLET IMPACT OVER A HEATED SURFACE IN AIR-VAPOUR MEDIUM	94
5.1	Introduction	94
5.2	Numerical model	94
5.2.1	Evaporation model	96
5.3	Validation of the model	97
5.3.1	Sessile droplet evaporation	97
5.3.2	Single droplet impact over a heated surface	98
5.3.3	Parametric study: Two consecutively impinging droplets at different time intervals over a hot surface	105
5.3.4	Analytical modelling	110
5.3.5	Closure	111
6	CONCLUSIONS AND SCOPE FOR FUTURE WORK	113
6.1	Introduction	113
6.1.1	Numerical study: Droplet impact over a heated surface in vapour medium	113
6.1.2	Experimental study: Droplet impact over a heated surface in air-vapour medium	115
6.1.3	Numerical study: Droplet impact over a heated surface in air-vapour medium	117
6.2	Major conclusions of the present study	118
6.3	Suggestions for future work	119
6.4	Closure	120
	REFERENCES	121
	LIST OF PUBLICATIONS BASED ON THE RESEARCH	127

LIST OF TABLES

Table	Title	Page
3.1	Properties of FC-72 (Perfluorohexane) at saturation pressure of 1 bar	32
3.2	Percentage error in spread factor and heat transfer compared to grid size of 2-micron	33
3.3	Droplet configuration for different Weber number cases	40
3.4	Case details of different Jakob numbers	42
3.5	Case details of different Bond numbers	44
4.1	Thermo-physical properties of Inconel 600 alloy used in the present study.	64
4.2	Thermo-physical properties of Deionized water used in the present study, at 1 atm and ambient temperature of 22 ° C.	65
4.3	The experimental uncertainties associated with different parameters used in the study.	65
4.4	Experimental details of the considered literature cases in the analysis	83
4.5	Various surface temperatures used in the present study ($T_{sat} = 56\text{ °C}$)	87
5.1	Wagner coefficients for FC-72 and liquid Methanol	97
5.2	Grid independence study: Comparison of the outcomes with 4-micron grid size.	101
5.3	Summary of the constants and other conditions used in the analytical model	109

LIST OF FIGURES

Figure	Title	Page
1.1	Liquid cooling techniques	1
1.2	Spray cooling: Impingement configurations	2
1.3	Droplet behaviour post impingement: (a) Pre-impacting droplet (b) Advancing phase (c) Maximum spread (d) Receding phase (e) Sessile droplet	3
1.4	Single droplet impingement: Pre-impact and Post-impact scenario	3
1.5	Drop-on-drop impingement: Pre-impact and Post-impact scenario	3
1.6	Impingement morphologies over a dry wall. Image courtesy: Yarin (2006) and originally published in Rioboo <i>et al.</i> (2001)	5
2.1	Drop-on-drop impingement over non-heated Teflon surface for equal volume droplets and $We = 141$. Image courtesy: Wakefield <i>et al.</i> (2016)	13
2.2	Heat transfer regimes associated with a drop impinging a hot wall. Image courtesy: Liang and Mudawar (2017)	14
2.3	Regime diagram for ethanol drop impinging a heated sapphire wall, based on outcome of impact. Image courtesy: Staat <i>et al.</i> (2015)	15
2.4	The transition from nucleate boiling to film boiling of n-heptane droplet impact. Image courtesy: Chandra and Avedisian (1991)	17
3.1	Three-phase contact line region	27
3.2	Spread radius versus time	29
3.3	Heat flow versus time	29
3.4	Spread radius versus time	30
3.5	Input heat flow versus time	30
3.6	Grid independence study	31
3.7	Spread factor versus time	31
3.8	Drop-on-drop configuration	32
3.9	Numerical domain with boundary conditions	32
3.10	Spread factor versus time	33
3.11	Input heat flow versus time	33

3.12	Drop-on-drop impingement process with iso-surface ($\alpha = 0.5$) and temperature contours	35
3.13	Spread factor versus time	35
3.14	Spread factor versus time	36
3.15	Net spread factor versus time	36
3.16	Input heat flux versus time	37
3.17	STV ratio versus time	37
3.18	Spread factor versus time	40
3.19	Input heat versus time	40
3.20	Evaporation heat versus time	41
3.21	STV ratio versus time	41
3.22	Maximum spread diameter at different Jakob numbers	43
3.23	Spread factor versus time	43
3.24	Input heat versus time	43
3.25	Evaporation heat versus time	43
3.26	Spread factor versus time	45
3.27	Input heat versus time	45
3.28	Evaporation heat versus time	45
3.29	Sessile drop radius: Initial stage	46
3.30	Coalescing stage	46
3.31	Spread factor versus time	46
3.32	Net spread factor versus time	46
3.33	Input heat versus time	47
3.34	Evaporation heat versus time	47
3.35	STV ratio versus time	47
3.36	Energies associated with droplets at initial and maximum spread	48
3.37	Maximum spread factor: Analytical versus Simulation	51
3.38	Non-dimensional input heat: Analytical versus Simulation	52
4.1	Schematic showing the experimental apparatus used in the present study	54
4.2	Impingement configurations considered in the present work	55
4.3	Schematic showing the temporal change of spread diameter during the impact	56

4.4	Steps involved in image post-processing: (a) Grayscale (b) Binary (c) Region recognition	56
4.5	Droplet volume calculation	56
4.6	Contact angle measurement	57
4.7	(a) Raw image (T = 154 °C and t = 15 ms) (b) Filtered image (c) Droplet input heat flux distribution along the centreline X-X (d) Effectiveness	58
4.8	Heat transfer calculation: energy balance at a pixel element	59
4.9	Single droplet impact over the target surface (T = 154°C)	62
4.10	Comparison in advancing phase	62
4.11	Comparison in receding phase	62
4.12	Drop-on-drop impact over a non-heated surface	63
4.13	Single droplet impact over a heated surface (T = 120 °C)	64
4.14	Single droplet impingement over the foil surface (T = 154 °C) : (a) Side-view image (b) Foil surface temperature after impingement (c) Change in temperature (d) Heat flux distribution	66
4.15	Drop-on-drop impingement over the foil surface (T = 154 °C) : (a) Side-view image (b) Foil surface temperature after impingement (c) Change in temperature (d) Heat flux distribution	67
4.16	Spread factor versus time	68
4.17	Comparison of single droplet and drop-on-drop impact over the surface (T = 154 °C)	68
4.18	Maximum spread factor with surface temperature: Single drop and drop-on-drop impact	69
4.19	Dynamic contact angle versus time	70
4.20	Static contact angle versus temperature	71
4.21	Effective area recognition to calculate the average surface heat transfer rate	71
4.22	Droplet input heat transfer versus time	72
4.23	Effectiveness versus time	72
4.24	Comparison of single and drop-on-drop impact over the target surface (T = 154 °C)	73
4.25	Target surface center temperature versus time	73
4.26	Comparison of effective area for the target surface (T = 154 °C)	74
4.27	Surface mean temperature versus time	74
4.28	Comparison of single and drop-on-drop impact over the surface with temperature 154 °C	75

4.29	Comparison of dimensionless temperature ($T = 154\text{ }^{\circ}\text{C}$) (a) Single droplet impact (b) Drop-on-drop impact (c) Distribution along the centreline X-X	76
4.30	Effectiveness versus temperature	76
4.31	Post-impact behaviour over the target surface ($T = 154\text{ }^{\circ}\text{C}$; $t = 8\text{ ms}$)	77
4.32	Single drop impact: Maximum spread	78
4.33	Drop-on-drop impact: Maximum Spread	79
4.34	Maximum spread factor: Experimental versus theoretical	80
4.35	Effectiveness: Experimental versus theoretical	82
4.36	Validation: Experimental versus theoretical	83
4.37	FC-72 droplet behaviour ($t = 10\text{ ms}$) over a non-heated surface ($29\text{ }^{\circ}\text{C}$) and at Dynamic Leidenfrost temperature ($105\text{ }^{\circ}\text{C}$)	85
4.38	Droplet impingement over the surface at a temperature of $57\text{ }^{\circ}\text{C}$. .	86
4.39	Single droplet impingement over the surface at a temperature of $105\text{ }^{\circ}\text{C}$: Dynamic Leidenfrost Point	87
4.40	Spread factor versus Time	88
4.41	Drop-on-drop impact: Net Spread factor versus Time	88
4.42	Input heat transfer versus Time	89
4.43	Dimensionless input heat transfer versus Time	90
4.44	Single droplet impingement: Boiling regimes ($We = 20$ and $Re = 986$)	90
4.45	Surface centre temperature versus Time	91
4.46	FC-72 droplet impingement over a heated surface	91
4.47	Maximum spread factor: Experimental versus theoretical	92
4.48	Effectiveness: Experimental versus theoretical	92
5.1	Sessile droplet evaporation: Case details and numerical domain . .	98
5.2	Droplet volume versus time	98
5.3	Single droplet impact: Case details and numerical domain	99
5.4	Grid independence study: FC-72 droplet impact over the surface with temperature $T = 70\text{ }^{\circ}\text{C}$	100
5.5	Evaporation heat transfer versus time	100
5.6	Static contact angle versus temperature	101
5.7	Contact angle analysis: FC-72 droplet impact over the surface with temperature $T = 70\text{ }^{\circ}\text{C}$	102

5.8	Comparison of the experiment ($T = 57\text{ }^{\circ}\text{C}$, $We = 20$, $Re = 986$), and simulation with concentration (left) and temperature (right) contours	103
5.9	Comparison of the experiment ($T = 105\text{ }^{\circ}\text{C}$, $We = 20$, $Re = 986$), and simulation with concentration (left) and temperature (right) contours	103
5.10	FC-72 droplet impingement over the heated surface ($T = 57\text{ }^{\circ}\text{C}$, $We = 20$, $Re = 986$)	104
5.11	FC-72 droplet impingement over the heated surface ($T = 105\text{ }^{\circ}\text{C}$, $We = 20$, $Re = 986$)	104
5.12	FC-72 droplet impingement over the heated surface ($We = 20$, $Re = 986$)	105
5.13	Parametric study : (a) Different instants of single droplet impact ($T = 70\text{ }^{\circ}\text{C}$, $We = 20$, $Re = 986$) (b) Consecutively impinging droplets (Drop-on-drop impact) at these instants	106
5.14	Parametric study : Case details and the numerical domain	107
5.15	Drop-on-drop impact with time interval of 0 ms, $T = 70\text{ }^{\circ}\text{C}$, $We = 20$, $Re = 986$: Contours of concentration (left) and temperature (right)	108
5.16	Drop-on-drop impact with time interval of 20 ms, $T = 70\text{ }^{\circ}\text{C}$, $We = 20$, $Re = 986$: Contours of concentration (left) and temperature (right)	109
5.17	Parametric study of Drop-on-drop impact over the surface with temperature $T = 70\text{ }^{\circ}\text{C}$, $We = 20$, $Re = 986$: Spread factor and input heat transfer variation with time	110
5.18	Parametric study of Drop-on-drop impact over the surface with temperature $T = 70\text{ }^{\circ}\text{C}$, $We = 20$, $Re = 986$: Evaporation heat transfer and STV variation with time	110
5.19	Parametric study of Drop-on-drop impact over the surface with temperature $T = 70\text{ }^{\circ}\text{C}$, $We = 20$, $Re = 986$: Dimensionless input and evaporation heat transfer variation with time	111
5.20	Parametric study: Effectiveness ratio	111
5.21	Experimental versus theoretical	112

ABBREVIATIONS

CCD	Charge Coupled Device
CFD	Computational Fluid Dynamics
DLP	Dynamic Leidenfrost Point
DPM	Droplets Per Minute
FPS	Frames Per Second
HTTP	Heat Transfer and Thermal Power
IIT	Indian Institute of Technology
NETD	Noise Equivalent Temperature Difference
SCA	Static Contact angle Analysis
STV	Surface area-To-Volume ratio

NOTATION

A_e	Effective area, m^2
A_e^*	Dimensionless effective area
c	Specific heat capacity of the heater, J/kgK
d	Instantaneous spread diameter, mm
D_0	Impacting droplet diameter, mm
D_1	Sessile droplet diameter, mm
D_s	Initial/sessile droplet spread diameter, mm
g	Acceleration due to gravity, m/s^2
h_s	height of the sessile droplet, mm
h_{max}	height of the droplet at maximum spread, mm
h_{lv}	Latent heat of vaporization, J/kg
m	Mass of liquid droplet, kg
Q_{cond}	Net conduction heat transfer, W
Q_{conv}	Convective heat transfer, W
Q_{drop}	Droplet input heat transfer, W
Q_{gen}	Generated heat, W
Q_{rad}	Radiation heat transfer, W
Q_{stored}	Stored heat, W
Q^*	Effectiveness or cooling efficiency
Q_e^*	Dimensionless evaporation heat transfer (mass)
S^*	Spread factor, (d/D_0)
S_{max}^*	Maximum spread factor, (d_{max}/D_0)
T	Temperature of the surface, $^{\circ}C$
T^*	Dimensionless temperature
t	Time, ms
T_{∞}	Ambient temperature, $^{\circ}C$
T_{sat}	Saturation temperature, $^{\circ}C$
U_0	Impact velocity of droplet, m/s

V	Volume of the droplet, m^3
Y	Mass concentration, kg/m^3

Non-dimensional quantities

Bo	Bond number, $\rho_l g D_0^2 / 4\sigma$
Ja	Jakob number, $c\Delta T / h_{lv}$
Pr	Prandtl number, $\mu_l c_{pl} / k_l$
Re	Reynolds number, $\rho_l U D_0 / \mu_l$
We	Weber number, $\rho_l D_0 U^2 / \sigma$

Greek alphabet

ϵ	Effectiveness ratio
θ	Three-phase contact angle, degree
σ_{sd}	Standard deviation
τ	Non-dimensional time, tU_0 / D_0

Subscripts

f	final
i	initial
l	liquid
max	maximum

CHAPTER 1

INTRODUCTION

1.1 Motivation

High-performance computing (HPC) is becoming ever more important as a research tool. It is also extended to industrial-based applications where an enormous amount of data is to be handled and analysed, which are named as Data Centers (DC). Data Centers, as such, consume a tremendous amount of energy to power and manage the server devices (Minas and Ellison, 2009). A significant expenditure towards cooling is required to ensure the reliability of the devices, which accounts for about 40% of the data center's total energy consumption. With the miniaturization of microelectronic components and growing component density, air cooling becomes inefficient. It demands heat sinks with bigger fans at the chassis level, thus hindering a rise in the rack density. By using liquid cooling, the size of the heat sinks can be reduced drastically, thus naturally promoting a surge in server component density. The evolving liquid cooling techniques such as spray, micro-channels, and impingement jet cooling are shown in Figure 1.1.

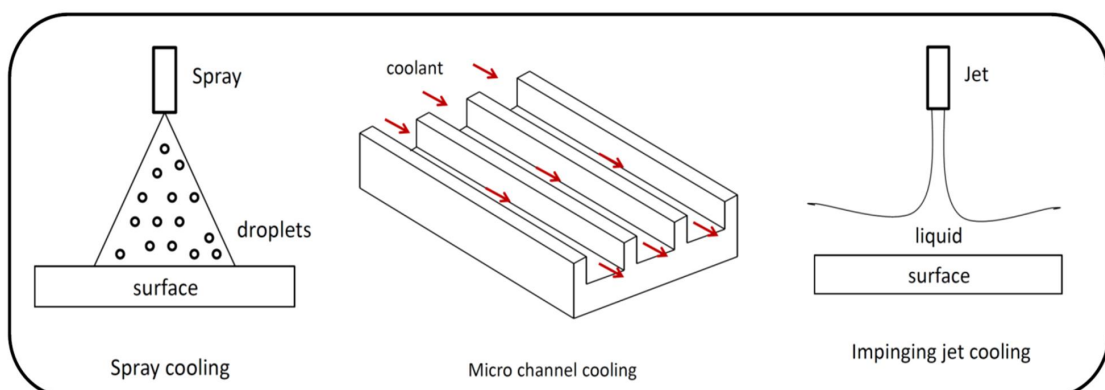


Fig. 1.1: Liquid cooling techniques

Spray cooling is one of the efficient liquid cooling techniques which has numerous industrial applications apart from data centers and electronics cooling. To comprehend

the spray cooling operation, the interpretation of relevant basic processes such as single droplet impact, drop coalescence and drop-on-drop collisions, etc., is required. Some of the impingement scenarios during the spray cooling are summarized in Figure 1.2. Extensive research studies on single droplet impact over non-heated and heated surfaces are available in literature. The present work deals with the numerical and experimental investigation of drop-on-drop impingement over heated surfaces.

On the other hand, various natural and industrial processes require the knowledge of droplet interactions with surfaces. The underlying physics of these droplet systems is complex, and has triggered many experimental and numerical investigations in the past decades. Applications such as inkjet printing, spray coating, and tablet encapsulation require the study of droplet dynamics over adiabatic (non-heated) surfaces. Droplet interaction with heated walls is also a topic of interest in processes such as metal quenching, fuel-air interaction in internal combustion engines, power plant engineering, and refrigeration.

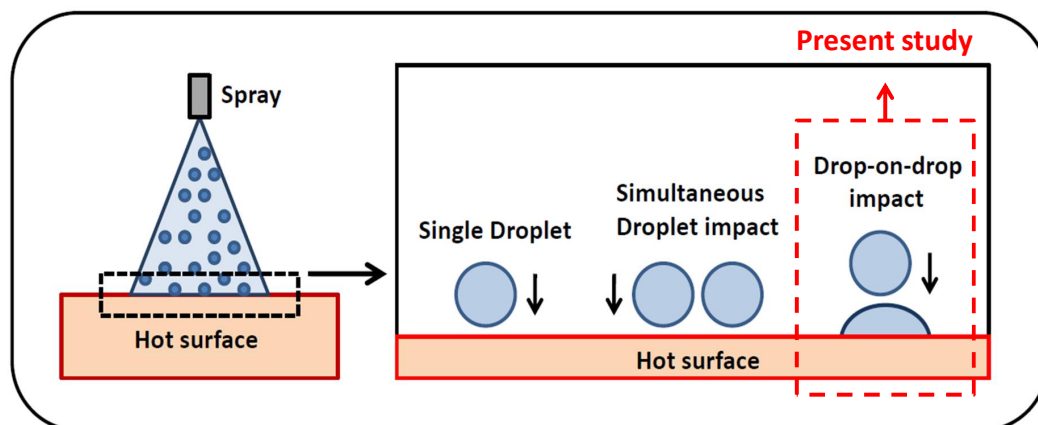


Fig. 1.2: Spray cooling: Impingement configurations

1.1.1 Droplet impingement: Nomenclature

When a droplet is impacted on a surface, it will perform cycles of the advancing (spreading) and receding (retracting) phases for a specific time and comes to a static position, which is named as the sessile droplet. Figures 1.3a to 1.3d shows the hydrodynamics observed during one cycle of post-impingement behaviour, and 1.3e is the sessile droplet.

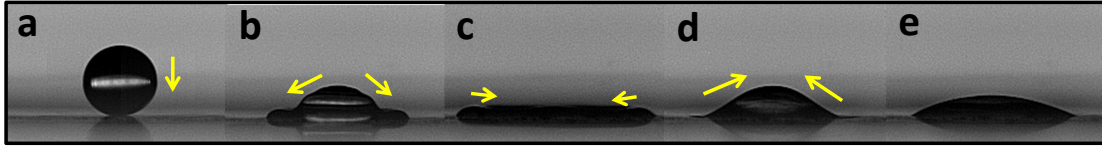


Fig. 1.3: Droplet behaviour post impingement: (a) Pre-impacting droplet (b) Advancing phase (c) Maximum spread (d) Receding phase (e) Sessile droplet

During the advancing phase, (Chandra and Avedisian, 1991; Rioboo *et al.*, 2001) the inertial forces influence the spreading, and droplet spreads to a maximum due to viscous dissipation. At this point, the capillary forces dominate and retract the droplet. A series of cycles will continue until it dissipates the energy and reaches an equilibrium (sessile droplet). For a droplet of diameter D_0 and the impact velocity U_0 as shown in the Figures 1.4 and 1.5, the spread dynamics and time scale is represented in terms of dimensionless parameters.

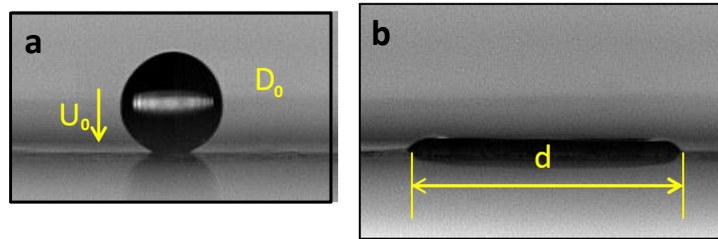


Fig. 1.4: Single droplet impingement: Pre-impact and Post-impact scenario

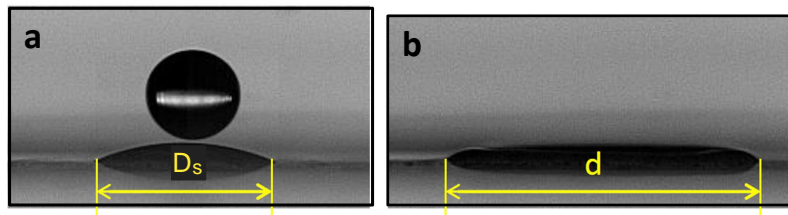


Fig. 1.5: Drop-on-drop impingement: Pre-impact and Post-impact scenario

Spread factor (S^*) is defined as the ratio of instantaneous spread diameter (d) to the impacting droplet diameter (D_0)

$$\text{Spread factor } S^* = \frac{d}{D_0} \quad (1.1)$$

While non-dimensional time (τ) is given as a ratio of actual time to spreading time scale.

$$\text{Dimensionless time } \tau = \frac{tU_0}{D_0} \quad (1.2)$$

In the case of drop-on-drop impact, with a leading droplet sitting on the surface with an initial spread D_s , the net spread factor (δS^*), at a given instant of time, is defined as the ratio of change in spread diameter ($d - D_s$) to the impacting droplet diameter (D_0).

$$\text{Net spread factor } \delta S^* = \frac{d - D_s}{D_0} \quad (1.3)$$

1.1.2 Possible morphologies of droplet impact

The phenomena of droplet impingement are governed by inertial, viscous, surface tension, and contact line forces near the three-phase contact region. Droplet behaviour during the impact depends upon surface properties and impingement parameters. Rioboo *et al.* (2001) presented the possible morphologies during a droplet impact, as shown in Figure 1.6. When viscous and capillary forces dominate the inertial forces during the spreading, it will result in a '*Deposition*' where well-defined spread profiles are observed without any satellite droplets. When the surface is hydrophobic (partially wetting), during the receding phase of the droplet, there will be a '*Partial rebound*' with secondary droplets ejecting out of the droplet. Whereas for a superhydrophobic surface (completely non-wetting), there is a complete rebound from the surface. For super-hydrophilic surfaces (completely wetting), a receding breakup is noticeable. If the inertial forces are dominating, there will be a droplet splash with a generation of satellite droplets during the spreading phase itself as in '*Prompt splash*' or from the rim of the droplet as seen in '*Corona splash*'.

The possibility of the splashing during the droplet impingement can be estimated from the characteristic number ' K'_D ' given as

$$K_D = We^{0.8} Re^{0.4} \quad (1.4)$$

And for a droplet splash to occur, ' K'_D ' number takes the value of 657 (Mundo *et al.*, 1995). Throughout the present study, a spherical droplet with impact conditions resulting in a deposition pattern is considered. The impingement is normal to the surface, and the surface deformation due to the droplet collision is neglected.

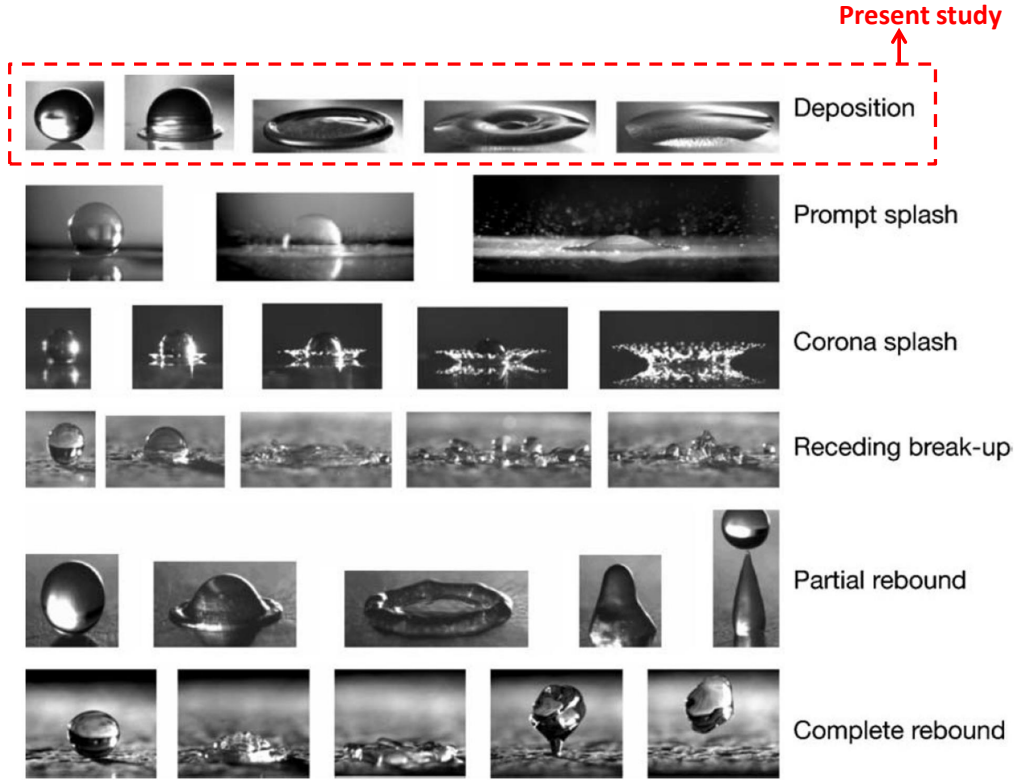


Fig. 1.6: Impingement morphologies over a dry wall. Image courtesy: Yarin (2006) and originally published in Rioboo *et al.* (2001)

The essential non-dimensional parameters that describe the droplet impact process are discussed below.

Weber number (We) is defined as the ratio of inertial forces to the capillary forces and found to be very effective parameter for the impact studies.

$$\text{Weber number } (We) = \frac{\text{Inertial forces}}{\text{Capillary forces}} = \frac{\rho_l U_0 D_0^2}{\sigma} \quad (1.5)$$

Reynolds number (Re) is given as the ratio of inertial forces to the viscous forces within in a fluid.

$$\text{Reynolds number } (Re) = \frac{\text{Inertial forces}}{\text{Viscous forces}} = \frac{\rho_l U_0 D_0}{\mu_l} \quad (1.6)$$

Jakob number (Ja) The wall superheat is non-dimensionalized using latent heat of vaporization of the fluid which is termed as Jakob number.

$$\text{Jakob number } (Ja) = \frac{\text{wall superheat}}{\text{latent heat}} = \frac{c\Delta T}{h_{lv}} \quad (1.7)$$

Bond number (Bo) is defined as a ratio of body forces to the surface tension forces.

$$\text{Bond number } (Bo) = \frac{\text{Body forces}}{\text{Capillary forces}} = \frac{\rho_l g D_0^2}{4\sigma} \quad (1.8)$$

1.2 Organization of the thesis

The thesis is organized into six chapters, including this chapter. A short description of the contents of each chapter is given below.

Chapter 1 provides a brief introduction to the motivation of the present work. It is followed by the description of nomenclature involved and different morphologies during the droplet impingement. In the end, an outline of the thesis chapters is presented.

Chapter 2 presents a detailed review of literature related to numerical and experimental investigation of the droplet impingement over non-heated and heated surfaces. Subsequently, the key findings of the literature are discussed in detail. Finally, the objectives and the scope of the present work are listed.

Chapter 3 provides the details of numerical investigation of droplet impact over a heated surface in saturated vapour (single-component) medium. The model is implemented in the open-source CFD software OpenFOAM considering contact line evaporation and dynamic contact angle motion. The implementation is validated using the experimental observations from the literature and is used to simulate the droplet impact onto a sessile droplet, i.e., drop-on-drop collision, over a heated surface. In the simulation, the droplet impingement and the surface heating are activated simultaneously, and the initial droplet interaction with the hot surface is not considered. Studying the drop-on-drop impact enables us to understand the presence of a liquid film (sessile droplet) affecting the droplet heat transfer. A comparison of the spread and heat transfer dynamics of the single droplet and drop-on-drop impingement is presented. Later on, influential parameters are identified from the past studies, and their effect on drop-on-drop impact dynamics is studied. In the end, the analytical models estimating the maximum spread factor and corresponding droplet input heat transfer are identified and extended to drop-on-drop impingement over the heated surfaces.

Chapter 4 reports the experimental investigation of the two consecutively impinging droplets over a heated surface. High-speed photography and Infrared thermography are used for the study. A brief description of the experimental set-up and image post-processing techniques used in the study are provided. The adopted experimental methodology is validated against the previous droplet impact studies of the literature. Preliminary experimental studies are carried out using Deionised water, and surface temperature is the parameter. The observations made from the experimental studies are compared with the results obtained from the analytical models presented in chapter 3. Following that, FC-72 (Perfluorohexane) liquid droplets are used for further studies where different boiling regimes are identified based on droplet spread dynamics and heat transfer. A comparison of droplet dynamics of the leading and trailing droplet impact during the consecutive impingement is presented.

Chapter 5 discusses the numerical implementation of droplet impact in air-vapour (multi-component) medium. The details of the mathematical formulation are elaborated, and the model is validated using the present experimental observations. Two contact angle models, i.e., static contact angle and contact line evaporation, are used in the simulations, and the effect on spread outcomes and heat transfer is presented. Later on, a parametric study is carried out by varying the time interval between the droplets during the consecutive impingement. The spread and heat transfer characteristics during the drop-on-drop impact with different time intervals are explained.

Chapter 6 summarizes the major conclusions of the present work. With an overview of the entire study, the scope for future work is discussed.

1.3 Closure

This chapter introduces the motivation behind the present work and the need for studying droplet impact configurations such as single droplet and drop-on-drop impact. An outline of possible droplet impingement scenarios and parameters used in the study are discussed. The next chapter provides a critical review of droplet impingement studies and summarizes the observations made from the literature.

CHAPTER 2

REVIEW OF LITERATURE

2.1 Introduction

This chapter deals with a critical review of the literature pertinent to the numerical and experimental investigation of droplet impingement over non-heated and heated surfaces. For ease of reading, the literature review is discussed under the following headings.

- Studies on droplet impact over non-heated surfaces
- Studies on droplet impact over heated surfaces

2.2 Studies on droplet impact over non-heated surfaces

Many initial studies were devoted to single droplet impingement onto non-heated surfaces as the impacting phenomena is also important in IC engines, inkjet printing, spray painting and coating applications. From earlier studies conducted on droplet impingement over adiabatic surfaces, the droplet impact scenario can be classified into three types based on the nature of target, i.e., solid wall, liquid film and deep liquid pool. Extensive reviews on these subtopics have been provided by Prosperetti and Oguz (1993), Rein (1993), Yarin (2006), Moreira *et al.* (2010), Marengo *et al.* (2011), and Josserand and Thoroddsen (2016). They have summarized several aspects associated with the hydrodynamics of the impingement process i.e., nature of impact, surface wettability, influence of thermophysical properties, and the observed regimes of evaporation. Numerical investigations of the droplet impact on to isothermal surfaces were found to be successful where different techniques such as marker-cell method (Harlow and Shannon, 1967), front tracking method (Tryggvason *et al.*, 2001), Volume of Fluid (VOF) (Šikalo *et al.*, 2005; Bussmann *et al.*, 1999) method were employed to capture the dynamics of droplet deformation during the process.

Theoretical models based on the total energy conservation of impacting droplet predicting the maximum spread diameter (Fukai *et al.*, 1995; Pasandideh-Fard *et al.*, 1996) were also proposed and validated with the experimental results.

Significant studies available in literature on single droplet and multiple droplet impact over non-heated surfaces are discussed below in detail.

2.2.1 Single droplet impingement

Harlow and Shannon (1967) investigated the splashing of a liquid droplet during its impingement over a flat plate, a shallow or a deep pool. Navier-Stokes equation is solved using Marker and cell (MAC) method in cylindrical coordinates. In all the calculations, the viscosity and surface tension effects are neglected, and the spreading phase of the droplet is modelled. Correlations predicting the rate of droplet spread and height are provided and validated with the available experimental results. A discussion of the effects of pressures, compressibility, droplet velocities, rupture and oscillations are also included.

Fukai *et al.* (1993) implemented a numerical model based on finite elements with deforming grid to simulate the droplet deformation during the impact. The surface tension effects during the droplet spreading are accounted. Two liquids with different thermophysical properties, water and liquid tin are considered, which are relevant to spray cooling and coating applications. Effects of droplet diameter, surface tension, impact velocity and material properties on spread dynamics are captured. The occurrence of droplet recoiling and mass accumulation around the splat periphery were defining features of the flow field and yielded a non-monotonic dependence of the maximum splat radius on time. The frequencies of the droplet oscillation are computed and found to be characteristic of natural frequencies of unobstructed droplet oscillation. Moreover, it is observed that the dynamics during the droplet deformation is significantly different for a water and liquid tin.

Rein (1993) presented a review on liquid droplet dynamics during the impact over dry and liquid surfaces. The impact outcomes such as spreading, splashing and bouncing on solid surfaces, and coalescence, bouncing, and splashing on liquid surfaces are described. The discussions on cavitation and the gas entrainment during

the impacts are also included. Details of the impact conditions resulting in the outlined morphologies have been incorporated in this review.

Prosperetti and Oguz (1993) discussed the earlier works on the topics of bubble growth, entrainment, liquid drop impact, and rain water splashing. The experimental work through high-speed photography and the numerical formulation implemented to simulate the droplet dynamics have been presented.

Fukai *et al.* (1995) improved the previous model by accounting the effect of inertial, body, surface tension forces and surface wettability effects along with the contact angle hysteresis. Later, they performed experiments on different wettable surfaces and compared with the numerical results. The maximum splat radius decreased with the value of the dynamic contact angle for the spreading stage. Also, the effect of impact velocity on droplet spreading was more pronounced when the wetting was limited.

Pasandideh-Fard *et al.* (1996) conducted the experiments and numerical simulations of droplet impact onto flat surface. The high speed photographs are used to extract the droplet diameters during the impingement and Solution Algorithm (SOLA) -volume of fluid method (VOF) based on the Marker and cell (MAC) method is used for numerical analysis through finite element grid. Different liquid-surface contact angles are varied adding surfactants to the water. It is found that the maximum spread diameter is not affected by the addition of surfactants but there is a change in droplet shapes during the recoiling stage. A static (equilibrium) and dynamic contact angle effects are also included during the simulations and observed that the numerical predictions are more accurate using dynamic contact angle values. An analytical model predicting the maximum spread diameter based on the conservation of energy is formulated and is able to show that the capillary effects are negligible when $We \gg Re^{0.5}$.

Bussmann *et al.* (1999) presented a 3-D numerical model to simulate droplet impact over the asymmetric surfaces. A volume tracking technique is used to capture the droplet break up and deformation in an Eulerian fixed-grid. Surface tension effects are included as a volume force near the free surface and the contact angle is prescribed along the contact line. Simulations of droplet impact over an inclined and sharp edge surfaces were presented and validated using the photographs taken during the

experiments. Contact angle measurements from the photographs are used in numerical analysis to capture the dynamics and yielded a better agreement. A simpler model is proposed for contact angle as a function of contact line velocity, and applied to both geometries. The model required values of only two contact angles, at a rapidly advancing and a rapidly receding contact line. The implemented model is found to be efficient in capturing the droplet deformation especially when characterised by notable inertial and viscous effects.

Tryggvason *et al.* (2001) modelled the multiphase flows using a front-tracking method. Direct numerical simulations are presented in a fixed, structured grid using finite volume method. The interface which is the 'front', separating the phases, is realised using the connected marker points. The interfacial source terms are calculated at the interface and transferred to the grid. Density and other fluid properties, and their advection are computed by following the interface (front) motion. The detailed description of interface representation, its motion, and transfer of data to the grid are presented. Later on, the simulation cases of bubble flow, solidification, boiling and atomization of sprays are successfully carried out.

Rioboo *et al.* (2001) conducted the experimental investigation of droplet impacts over the surfaces. High speed photography is used and a qualitative analysis of the outcomes of droplet impingement is presented. A wide range of liquid properties are considered by using water, silicon oil, water-glycerine mixture, ethanol and liquid alloys. The different morphologies of post-impact are presented and identified them as the splash, prompt splash, rebound, corona splash and others.

Šikalo *et al.* (2005) carried out the experiments of droplet impact over a dry wall with a partial wettability nature. Glycerine and water droplets impact over a wax and glass surface are conducted. The instantaneous spread diameters and contact angles are measured. Later on, different dynamic contact angle models are discussed and Kistler's model is used for the simulation. Numerical simulations are carried out using finite volume method in an unstructured grid. It is found that the wall treatment using an appropriate contact angle model improved the accuracy of the numerical results.

Yarin (2006) presented a review on the droplet impacts over dry surfaces and liquid films. The motivation behind the studies of drop impingement is provided. The discussions of experimental, theoretical and computational aspects of the topic are

given in detail. The description of morphologies such as splashing, crown formation and their propagation are the main focus of the paper.

Moreira *et al.* (2010) summarized the investigations on the droplet-wall interactions pertaining to the IC engine applications. The fundamental findings of the individual droplet impact and their relevance in understanding the spray interaction with the wall have been discussed in detail.

Marengo *et al.* (2011) reviewed the experimental, numerical and theoretical analysis carried out in the field of droplet impacts over a simple (smooth) surfaces. Following that, the studies on complex surfaces such as with variable surface roughness, micro and nano structures, and the wettable and non-wetting surfaces are presented. The basic outcomes of the impingement upon simple and complex surfaces, and their dependence on the impact conditions have been epitomized.

Josserand and Thoroddsen (2016) reviewed the latest findings on the topic of droplet impact over a solid substrate. Along with the discussions on the post-impact outcomes such as splash, bouncing, and spreading, the particular focus is given to the gas entrainment into the droplets. The effect of surrounding gas, surface roughness, and their role in the repellency of the droplets during the impingement is extensively presented.

2.2.2 Multiple droplet impingement

Liu *et al.* (1993) carried out the numerical simulations of liquid droplet interaction with cold substrates which results in deformation and freezing during the impact. The Navier-Stokes equations are solved in a two-domain method using the VOF interface tracking technique. The two-domain method is for the thermal domain, and a two-phase continuum model of the growing solid layer in the fluid. The effect of impacting conditions such as droplet impacting velocity, temperature and solid surface temperature on the spread dynamics are presented.

Yarin and Weiss (1995) studied the droplet train impingement over a solid surface through experimental and theoretical analysis. High and low impact velocities resulting in spreading, and splashing phenomena respectively are recorded using a CCD camera. The secondary droplets resulting from the splashing, and their

distribution and volume are measured from the experimental observations. The threshold for splashing is characterised in terms of impact conditions. Later on, capillary vibrations during the low velocity impacts are analysed and the patterns are observed to be self-similar.

Fujimoto *et al.* (2001) conducted the experimental and numerical investigation of a impacting droplet on to a sessile droplet. Flash photographic technique is used to capture the physics of the phenomena. The impacting velocity is the parameter and observed the crown formation at the rim when the droplet is colliding on to the static droplet. Following that a numerical model is implemented in finite difference method by solving the Navier-Stokes equation. A 2-D axisymmetric domain is considered by accounting the viscous, surface tension, and gravity effects. A reasonable agreement of hydrodynamics is achieved with the experimental observations.

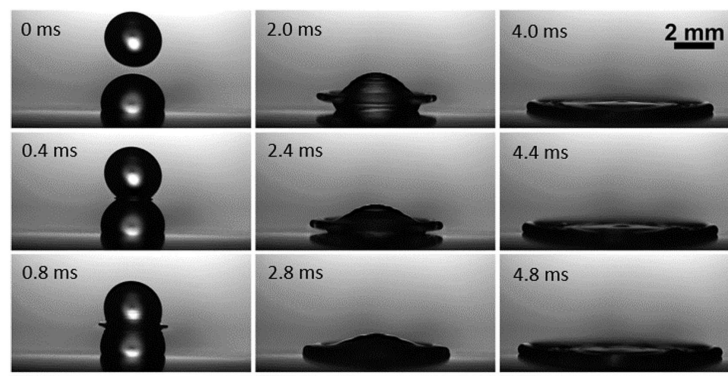


Fig. 2.1: Drop-on-drop impingement over non-heated Teflon surface for equal volume droplets and $We = 141$. Image courtesy: Wakefield *et al.* (2016)

Wakefield *et al.* (2016) presented the experimental analysis of the falling droplet onto a static droplet over a hydrophobic surface as shown in Figure 2.1. The impacting energy, i.e., Weber number is the parameter of interest. It is found that at high weber numbers, the droplets makes a one event of advancing and receding and reaches equilibrium thereby confirms that the energy dissipation is high during the spreading, receding and crown formation. Whereas, the droplet system performs a series of advancing and recoiling phases for a low weber number impact studies. Later on, an analytical model for maximum spread diameter is formulated and showed that the one half of the impacting kinetic energy is dissipating to reach the maximum spread diameter.

2.3 Studies on droplet impact over heated surfaces

In the case of droplet impingement over hot surfaces, the process involves mass, momentum and heat transfer interactions, and thereby requires additional efforts for better understanding of the phenomenon. A comprehensive review of studies concerning the fluid mechanics and heat transfer mechanisms of liquid drop impact on a heated wall is presented by Liang and Mudawar (2017). Significant contributions were made in the literature in understanding the interfacial behaviour of droplet from the moment of impact over heated surfaces. It has been observed that heat transfer in droplet impingement over a hot surface is strongly dependent on the magnitude of wall temperature relative to the liquid's saturation temperature. Factors such as droplet diameter, impact velocity, physical properties of the liquid, nature of the surrounding gas, and wall characteristics can also influence the overall process.

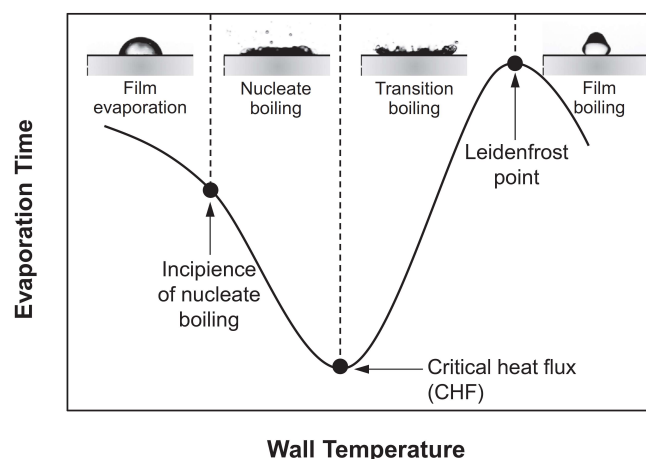


Fig. 2.2: Heat transfer regimes associated with a drop impinging a hot wall. Image courtesy: Liang and Mudawar (2017)

Four distinct regimes, as shown in Figure 2.2, are identified based on the evaporation lifetime of a single drop at different wall temperatures as film evaporation, nucleate boiling, transition boiling and film boiling (Ko and Chung, 1996; Naber and Farrell, 1993). Efforts were made to quantify the impact dynamics and heat transfer behaviour in those regimes in order to characterize the droplet-hot wall interactions. Bernardin *et al.* (1997, 1996) revealed that wall temperature and impact Weber number are the two most influencing parameters governing the impingement process over heated surfaces. Impingement studies were carried out for low and high Weber numbers and extensive maps concerning the impact and heat transfer were provided. They have also studied the

effect of surface roughness and found that surface features can influence the observed boiling regimes.

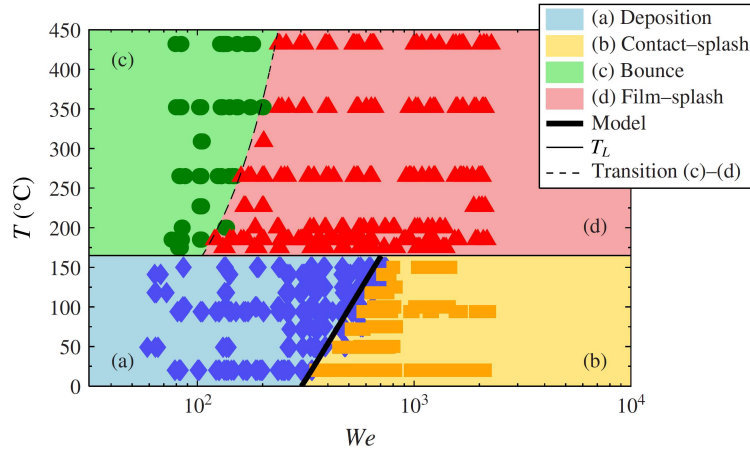


Fig. 2.3: Regime diagram for ethanol drop impinging a heated sapphire wall, based on outcome of impact. Image courtesy: Staat *et al.* (2015)

Using advanced diagnostic tools such as high speed imaging (Wang *et al.*, 2005, 2000; Staat *et al.*, 2015), interferometry and total internal reflection techniques (Tran *et al.*, 2012; Limbeek *et al.*, 2016), attempts were made to quantify the droplet boiling regimes based on the observations of hydrodynamic behaviour during impact as shown in Figure 2.3.

Film evaporation takes place when the wall temperature is below the liquid's saturation temperature, and even when the wall is superheated but insufficient to initiate bubble nucleation inside the drop upon contact with the surface (Liang and Mudawar, 2017). It is observed that, in film evaporation regime, droplet heat transfer is affected by temperature variations inside the droplet, wall heat flux and droplet evaporation rate (Di Marzo and Evans, 1989; Marzo *et al.*, 1993; Ruiz and Black, 2002; Berberović *et al.*, 2011; Strotos *et al.*, 2008b). Chandra *et al.* (1996) investigated the effect of contact angle on droplet evaporation rate by experimental investigation. They have used a surfactant to reduce the contact angle resulting in higher evaporation rates. Pasandideh-Fard *et al.* (2001) presented a numerical model and carried out simulations revealing that impact velocity has a minor influence on the overall droplet heat transfer. From these works, it is identified that wall temperature is lowest at the impact point and increase in the radial direction toward the edge of the droplet. Investigators (Cui *et al.*, 2001; Nakoryakov *et al.*, 2012) also found that the evaporation rate is highest at the three-phase contact line and several numerical

predictions (Di Marzo and Evans, 1989; Berberović *et al.*, 2011; Herbert *et al.*, 2013b; Francois and Shyy, 2003; Strotos *et al.*, 2008a; Ge and Fan, 2006; Healy *et al.*, 2001) have confirmed these observations.

Nucleate boiling regime is the region extended from the point of bubble nucleation, which will take place when wall temperature is above the saturation temperature, to the critical heat flux point which corresponds to shortest droplet evaporation time. Tarozzi *et al.* (2007) demonstrated a non-intrusive optical method to measure liquid-solid contact temperature where an infrared camera was used to capture the foot print from the underside of the impact surface. It was reported that the onset of the nucleate boiling depends on contact temperature, and observed the regime when contact temperature exceeds the liquid's saturation temperature. Studies on the effect of the dissolved gases and salts (Cui *et al.*, 2001), surface thickness (Nakoryakov *et al.*, 2012), surfactants (Qiao and Chandra, 1997), nano fluids (Okawa *et al.*, 2012), droplet size and physical properties (Xiong and Yuen, 1991) on the incipience of bubble nucleation are available. Predictions of critical heat flux temperatures (Bernardin *et al.*, 1997, 1996; Kandlikar and Steinke, 2001) were also reported in the literature for different liquids including water, and correlations provided (McGinnis and Holman, 1969; Holman *et al.*, 1972) for corresponding maximum heat transfer rate.

For liquid-solid interface temperatures at or above certain temperature, named as the Leidenfrost temperature, the liquid in the immediate vicinity of the wall is instantaneously converted to vapour upon contact, and forms a continuous insulating vapour layer between the liquid and the wall (Bernardin and Mudawar, 1999, 2002). In literature, this temperature is identified as the lowest wall temperature of the film boiling regime and has been studied in relation to sessile drop over hot surface termed as static Leidenfrost temperature (Wang *et al.*, 2005; Okawa *et al.*, 2012; Avedisian and Koplik, 1987). While, for impinging droplets, this temperature is termed as dynamic Leidenfrost temperature where rebound of the droplet from the surface can be observed (Okawa *et al.*, 2012; Bernardin and Mudawar, 2002; Pedersen, 1970). Influence of pressure, wall roughness, gravity and surface tension on static Leidenfrost temperature (Avedisian and Koplik, 1987; Celestini *et al.*, 2013; Kwon *et al.*, 2013; Arnaldo del Cerro *et al.*, 2012), and correlations (Celata *et al.*, 2006; Bertola and Sefiane, 2005) concerning the precise prediction of dynamic Leidenfrost temperatures in terms of saturation temperature, static Leidenfrost temperature and impact Weber

number are also available. In a recent work (D.V.Zaitsev *et al.*, 2017; Kabov *et al.*, 2017), it is shown that microscale droplets with low impacting velocities can find themselves in a Leidenfrost-type regime (levitating over the substrate) at substrate temperatures not only far below the Leidenfrost temperature but even below the saturation temperature. In addition, using levitating microdroplets as tracers it is shown that evaporation rate has a maximum at the three-phase contact line, confirming the results of other studies (Cui *et al.*, 2001; Nakoryakov *et al.*, 2012).

Significant studies available in literature on single droplet and multiple droplet impact over heated surfaces are discussed below in detail.

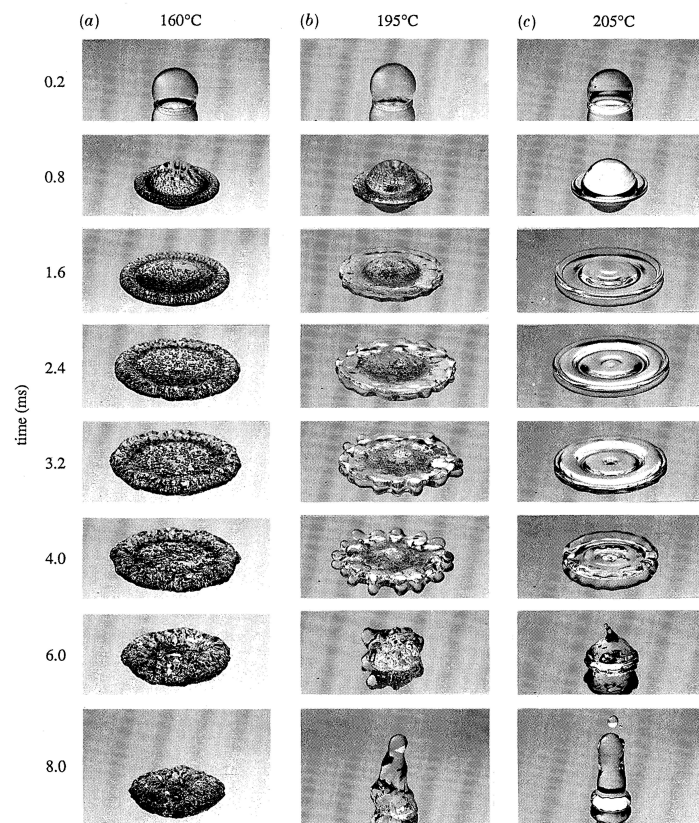


Fig. 2.4: The transition from nucleate boiling to film boiling of n-heptane droplet impact. Image courtesy: Chandra and Avedisian (1991)

2.3.1 Single droplet impingement

Chandra and Avedisian (1991) investigated the event of droplet impingement over a dry heated stainless steel surface using flash photographic method. N-heptane liquid droplets are used and the surface temperature is the parameter. Different regimes of boiling, from film evaporation up to the Leidenfrost point where the droplet jumps off

the surface due to the formed gas cushion, as shown in Figure 2.4, are observed during the study. The spread rate is measured from the images and found that the spreading phase is independent of the surface temperature due to negligible effects of viscous and surface tension. At high temperatures, below the Leidenfrost point, numerous bubbles were found inside the droplet. However, the overall droplet shapes are unaffected by the bubbles especially during the advancing phase. Later on, the studies are also extended to the consecutive droplet impingement. An analytical model based on energy balance is formulated to calculate the maximum spread rate and is in agreement with the experimental observations.

Lee *et al.* (2001) conducted the experimental studies of droplet impact over a hot surface to measure the heat flux and deformation from the time of impact till it evaporates completely. Adopted the high speed photography technique for imaging, and for heating the surface, a novel 96-element array heater is used. Three wall superheats are maintained which are 9K, 19K and 29 K. It is observed that the droplet evaporation process can be divided into two parts. Initial part is the one where transient heat transfer coefficients are observed and dependent on splat (spread) radius whereas the second part is with the constant heat transfer coefficient. The available models in the literature are then used to calculate the droplet evaporation time.

Nikolopoulos *et al.* (2007) presented the numerical simulation of the droplet impingement on a heated surface. The governing equations are solved using the finite volume method coupled with VOF interface tracking technique. N-heptane and water are the liquids and the three surface temperatures are selected such that one above and one below the Leidenfrost temperature. Both 2D-axisymmetric and 3-D domains are used and the model is able to capture the vapour blanket under the droplet during the impact. Droplet levitation from the surface was calculated without any ‘a priori’ assumption for the vapour layer height forming between the liquid and the wall. For high impact Weber number but on a surface with temperature below Leidenfrost, the splashing of the liquid associated with the formation of a ring detached from the spreading lamella is predicted. Moreover, formation of vapour bubbles within the bulk of the liquid was predicted while its volume was calculated transiently during the numerical solution. The numerical results are validated using the available experimental data, and the evaporation time and other details are computed from the simulation.

Hardt and Wondra (2008) formulated an evaporation model based on the continuum –field representation of the source terms for a wide range of CFD models. The evaporation source term is calculated from a physical relationship of evaporated mass and accordingly the mass source term is derived from the non-homogenous Helmholtz function with the spatial adjustment of the source terms using a free parameter. It is shown that the model is compatible with all interface-capturing techniques and using the VOF technique the simulations of bench mark cases of Stefan problem, droplet evaporation and two-dimensional film boiling cases are carried out.

Strotos *et al.* (2008a) conducted numerical simulations of droplet impingement over a heated surface in atmospheric conditions. A VOF-based numerical model is implemented and the surface cooling is captured by solving the fluid flow and the evaporation by considering the Fick's law based model. The numerical results are shown to be in agreement with the experimental observations. Model predictions for the droplet shape, temperature, flow distribution and vaporised liquid distribution reveal the detailed flow mechanisms that cannot be easily obtained from the experimental observations.

Chatzikyriakou *et al.* (2009) implemented a numerical model to simulate the sessile droplet and impacting droplets bouncing off over a superheated substrate. The liquid and gas interface is captured using the Level-set technique in finite volume method. A constant evaporation rate is assumed and two cases of Leidenfrost sessile and impacting droplet, from the literature, are considered. The temporal variation of vapour layer formed underneath the droplet is captured, and a good agreement is obtained.

Chatzikyriakou *et al.* (2011) conducted an experimental investigation of impacting droplets over a heated surface from wetting to non-wetting phase (high temperatures). A thin metal layer imparted upon an infrared transparent substrate is used as the surface. The infrared thermography is adopted and the heat transfer into the droplets is calculated from the images. The experimental uncertainty with this method is found to be 15%.

Herbert *et al.* (2013a) investigated the heat transport phenomena associated with the droplet impingement over a heated surface in a saturated vapour medium. Both experiments using high speed and infrared imaging, and numerical simulations using VOF method are conducted. A special attention is given to the evaporation near three-phase contact region and various heat transfer phenomena during the impact are

analysed. It is found that convective is domination during spreading whereas the contact line evaporation is dominant in receding phase.

Herbert *et al.* (2013b) performed numerical simulations using contactline evaporation model to study the effect of thermophysical properties on the droplet impingement process. A dimensionless analysis is carried out and Weber number (We), Prandtl number (Pr), Reynolds number (Re) and Bond number (Bo) are chosen are parameters. The VOF-interface capturing technique is used which is implemented in OpenFOAM based on finite volume method. It is observed that the dynamics during the spreading phase is influenced more by Reynolds number whereas the recoiling phase is affected by Weber number.

Gumulya *et al.* (2014) developed a numerical model using the coupled Level set-VOF method to capture the evaporating droplet during the impact on to a heated surface. Later on, an experimental data from the literature is considered for the model validation. It is found that the model is able to capture the spread dynamics and also predicted the bouncing of the droplet at high temperatures.

Villegas *et al.* (2016) proposed a numerical model in the framework of Ghost Fluid method and conducted direct numerical simulations of droplet impact by considering the boiling and evaporation. The key-point of this new method lies in the computation of the mass fraction field equation with an imposed Robin Boundary Condition at the interface. This formulation allows to capture continuously the transition between evaporation and boiling in thin regions of saturated vapor, as it can occur in Leidenfrost droplets or in superheated droplets. The model is later validated with the benchmark cases, theoretical solutions and experimental results.

Villegas *et al.* (2017) conducted experimental and numerical investigation of droplet impact over heated surface well above Leidenfrost temperatures. Impacting weber number is varied during the study. Later on, the experimental observations are compared with the numerical simulations using Ghost Fluid method and measured the vapour cushion thickness formed during the droplet bouncing.

2.3.2 Multiple droplet impingement

Bernardin and Mudawar (1997) attempted to predict the heat transfer efficiency of the

spray cooling in the film boiling regimes (temperatures upto 400 °C). First of all an experimental investigation of single stream of droplets is conducted, and the hydrodynamics and heat transfer characteristics are presented. Later on, these results are extrapolated to the sprays and multiple droplet streams by considering the appropriate volumetric flux and heat transfer. Empirical correlations were developed for the film boiling heat transfer rate and heat transfer efficiency for a single stream of water droplets. Key influential parameters in these correlations are surface temperature, droplet diameter, and droplet velocity.

Fujimoto *et al.* (2008) presented the study of two consecutively impinging droplets over a hot surface. The high speed imaging is used for the experiments and impacting velocity, surface temperature, and time interval between the droplets are varied. The effect of these parameters on the droplet hydrodynamics is discussed. The formation of a liquid crown is clearly observed at room temperature. The height of the crown is larger with wider spacing between two droplets and higher droplet impact inertia (Weber number).

Minamikawa *et al.* (2008) carried out numerical simulations of two consecutive impinging droplets over a heated surface at high temperatures. The governing equations considering the gravity, viscous and capillary forces are solved using the finite difference method. The hydrodynamics of droplet such as crown formation is highlighted in the study and numerical results are compared with the experimental observations.

Batzdorf *et al.* (2017) conducted a numerical investigation of simultaneous impingement of two droplets over a heated surface. The model is based on the VOF interface tracking technique and considers the contact line evaporation near the three-phase contact region. A theoretical model is also developed to predict the heat transfer rate during the spreading phase and observations are made with respect to the Prandtl number (Pr). The numerical and theoretical results are reasonably in agreement at the Prandtl number values of order unity. It is shown that at high Prandtl numbers the heat flow is mainly determined by the instantaneous wetted area while for Prandtl numbers of order unity, the contribution of evaporation is significant.

Breitenbach *et al.* (2018) presented a review of work on the droplet impacts which are aimed at understanding the spray cooling process. Significant theoretical models

proposed, and studies conducted in the past are discussed in order to establish a framework for the future work predicting the underlying physics of spray process. This review underlines the observation that the hydrodynamic behaviour of the drop impact can depend strongly on the respective regime and in general, the Weber number is not adequate to capture or describe regime boundaries, since the Weber number does not involve any aspect of heat transfer. It is realised that for sprays in which the drop number density is low enough such that little drop interaction on the substrate arises, single drop data can be used, incorporated into a statistical model for drop impact.

From the previous studies, it is observed that the impact dynamics and heat transfer mechanisms involved in multiple droplet collisions are not fully known. There is a need to assess various configurations of these droplet collisions and their interference over the heated surfaces for different boiling regimes. Comparison with a single droplet impact and theoretical models estimating the dynamics of the process will provide more insights into understanding the physical process of spray cooling. The present work is aimed at studying the spread and heat transfer dynamics of two consecutively impinging droplets, i.e., drop-on-drop impact.

2.4 Objectives of the present research work

- To develop and implement a numerical model to study the drop-on-drop impact over a heated surface in different ambient conditions (single and multicomponent medium), and examine the effect of influential parameters on the impingement dynamics and heat transfer.
- To design and carry out an experimental investigation of drop-on-drop impingement over a heated surface to visualize the spread and evaporation dynamics using high-speed photography and Infrared thermography.
- To incorporate available analytical models for obtaining droplet spread diameter and heat transfer during the impingement and to derive new analytical models for drop-on-drop impact configuration.

2.5 Closure

In this chapter the overview of the literature related to the droplet impingement is presented. The key findings are discussed in detail and the objectives of the present work are listed out. In next chapter the details of the numerical implementation to study droplet impact over heated surfaces in a vapour medium are provided.

CHAPTER 3

NUMERICAL STUDY: DROPLET IMPACT OVER A HEATED SURFACE IN VAPOUR MEDIUM

3.1 Introduction

This chapter provides the details of the numerical modelling of droplet impingement over a heated surface in a vapour medium. Additionally, the available analytical models predicting the droplet's maximum spread and heat transfer are discussed and developed new correlations for the drop-on-drop impact configuration.

3.2 Numerical modelling

The present numerical study focussed on a drop-on-drop impingement onto heated wetting surface. Even though the studies on drop-on-drop impact and droplet coalescence were conducted, the underlying physics is not yet fully understood. In addition, the head-on collisions of droplets over a heated surface are investigated to a lesser extent and also expected to be different from a single drop impingement scenario. In the current study, saturated FC-72 liquid is impinged onto chromium surface in its vapour region. The proposed numerical model is first validated with the experimental observations available in the literature. Following that a drop-on-drop impact phenomena is compared to single droplet impingement onto heated surface under same impact conditions. In the drop-on-drop simulation, the droplet impingement and the surface heating are activated simultaneously, and the initial droplet interaction with the hot surface is not considered. Studying this impingement configuration enables us to understand the presence of a liquid film (sessile droplet) affecting the droplet heat transfer. The spread and evaporation dynamics are examined for the both cases and later the study is extended to investigate the influence of important governing parameters such as Weber number (We), Bond number (Bo), Jakob number (Ja) and Radius ratio (R^*).

3.3 Mathematical formulation

A phase change solver is implemented in the open-source CFD toolbox OpenFOAM with VOF interface capturing technique. The event of drop-on-drop impingement is modelled through the conservation of mass, momentum, and energy equations. Here a one-field approach is adopted i.e., a single velocity, pressure and temperature fields are implemented for both liquid and gas phases.

$$\rho(\nabla \cdot \vec{u}) = \dot{\rho} \quad (3.1)$$

$$\frac{\partial(\rho\vec{u})}{\partial t} + \nabla \cdot (\vec{u} \cdot \rho\vec{u}) = -\nabla p + \nabla \cdot [\mu(\nabla\vec{u} + (\nabla\vec{u})^T)] + \vec{f}_g + \vec{f}_\sigma \quad (3.2)$$

$$\frac{\partial(\rho c T)}{\partial t} + \nabla \cdot (\rho c \vec{u} T) = \nabla \cdot (k \nabla T) + \dot{h} \quad (3.3)$$

where $\dot{\rho}$ and \dot{h} represents the evaporation mass and energy source terms respectively due to phase change of fluid. Here \vec{f}_g and \vec{f}_σ are the source terms which accounts for gravity and surface tension respectively. In this model, liquid and gases are assumed to be completely incompressible and dissipation term in the energy equation is neglected. In order to capture the interface, an additional equation in terms of volume fraction α is solved.

$$\frac{\partial\alpha}{\partial t} + \nabla \cdot (\vec{u}\alpha) = \frac{\dot{\rho}}{\rho}\alpha \quad (3.4)$$

Where α is defined as the ratio of volume of liquid to the volume of the cell. Thus it assumes a value of 1 and 0 for the phases of liquid and gas respectively and forms the interface between 0 and 1. All the properties (γ) at the interface cells can be calculated as volume weighted properties of the pure phases.

$$\gamma = \gamma_l\alpha + \gamma_v(1 - \alpha) \quad (3.5)$$

The surface tension source term \vec{f}_σ is given in terms of the interface curvature using continuum surface force model proposed by Brackbill *et al.* (1992)

$$\vec{f}_\sigma = \sigma K_c \nabla \alpha \quad (3.6)$$

where curvature K_c , in terms of volume fraction α is given as

$$K_c = \nabla \cdot \frac{\nabla \alpha}{|\nabla \alpha|} \quad (3.7)$$

3.3.1 Evaporation model

The mass and energy source terms are introduced in the conservation equations in order to consider the evaporation process. These source terms are evaluated based on an approach developed by Kunkelmann and Stephan (2010) for pool boiling studies. The local temperature gradient at the interface is used to calculate the evaporation fluxes for which the interface is assumed to be at saturation temperature. The default method available in the OpenFOAM, smears out the interface between phases. For an accurate estimation of distances between interface and the cells near to it, a special interface reconstruction method (Herbert *et al.*, 2013a; Pattamatta *et al.*, 2014) is incorporated in the model. An iso-surface of $\alpha = 0.5$, is constructed as interface from which the distances required for the temperature gradient calculation are evaluated. The mass source term $\dot{\rho}_0$ is given as

$$\dot{\rho}_{0,i} = \frac{S_{int,i}(k_l \nabla_{int} T_l + k_v \nabla_{int} T_v)}{h_{lv} V_i} \quad (3.8)$$

where $S_{int,i}$ and V_i are surface area and volume of the i^{th} cell near the interface and the local temperature gradients on liquid and gas phase sides are taken as

$$\nabla_{int} T_l = \frac{T_l - T_{int}}{d_{l,int}} \quad (3.9)$$

$$\nabla_{int} T_v = \frac{T_v - T_{int}}{d_{v,int}} \quad (3.10)$$

$d_{l,int}$ and $d_{v,int}$ represents the distances to the interface of the closest cell neighbor on either sides of the interface.

To ensure the numerical stability of the model, the calculated mass source term $\dot{\rho}_0$ is smeared out to smooth the source term distribution $\dot{\rho}$ as proposed by Hardt and Wondra

(2008). From the mass source term $\dot{\rho}_0$, the energy source term \dot{h} is calculated, as

$$\dot{h} = -\dot{\rho}_0 h_{lv} \quad (3.11)$$

Apart from these equations, special attention is given to the evaporation near the three phase contact line region.

Contact line evaporation model

As proposed originally by Potash and Wayner (1972), the zone near the three phase contact angle can be divided into three regions namely macro, micro and adsorbed regions as shown in Figure 3.1. It is observed that the macro region is influenced by capillary forces whereas micro region flow is dominated by both capillary and adhesive forces between the fluid and solid. The adsorbed region, which is of order of nanometres, is completely controlled by intermolecular dispersion forces.

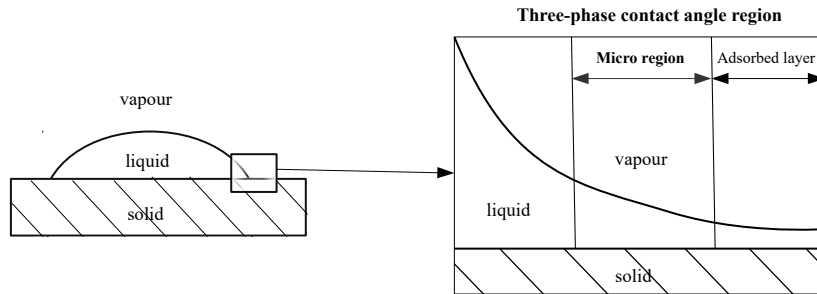


Fig. 3.1: Three-phase contact line region

Stephan and Busse (1992) modelled the micro region by solving the conservation equations where the adhesion effects are included in terms of ‘disjoining pressure’. Here the film thickness is assumed to be perfectly flat and lubrication approximation is used to solve the equations. Herbert *et al.* (2013a) extended this method to the single droplet impact and also considered the contact line motion. The effect of contact line velocity and wall temperature on contact line motion is inspected for a range of values. These results are fitted into a regression curve which will be used in the macroscopic simulation.

In order to model the micro region, a moving reference frame with a local coordinate

system and contact line velocity is assumed. As described in the reference (Herbert *et al.*, 2013a), the heat flux from the wall to interface can be given as

$$\dot{q} = \frac{T_{wall} - T_{sat}(1 + \frac{\Delta p}{h_{lv}\rho_l})}{\frac{\delta}{k_l} + R_{int}} \quad (3.12)$$

Where δ denotes the thickness of the film and the interfacial heat resistance R_{int} is calculated as

$$R_{int} = \frac{2 - \chi}{2\chi} \frac{T_{sat} \sqrt{2\pi R_{gas} T_{sat}}}{h_{lv}^2 \rho_v} \quad (3.13)$$

χ is the accommodation coefficient and the ideal gas constant R_{gas} . The pressure difference Δp in the micro region is calculated by considering capillary force, disjoining pressure and recoil pressure, as

$$\Delta p = \sigma \frac{\delta''}{(1 + \delta')^{1.5}} + \frac{A}{\delta^3} - \frac{\dot{q}^2}{h_{lv}} \left(\frac{1}{\rho_v} + \frac{1}{\rho_l} \right) \quad (3.14)$$

Here A is the dispersion coefficient which is kept constant ($A = 2 \times 10^{-21} J$). Using lubrication approximation, along with equation 3.12, the conservation equations are simplified and solved as a system of four non-linear ordinary differential equations over the micro region considered. The formulation and solution procedure are explained by the references (Kunkelmann and Stephan, 2009; Herbert *et al.*, 2013a; Raj *et al.*, 2012) in detail. Using this approach, the dependency of contact angle on the contact line velocity U_{cl} and wall superheat ΔT was studied (Herbert *et al.*, 2013a) and are fitted into a regression curve which are used in the macroscopic simulation. The described model with contact line evaporation was successfully implemented in previous simulations of pool boiling (Kunkelmann and Stephan, 2010), single droplet impingement onto heated surfaces (Herbert *et al.*, 2013b) and Taylor-bubble coalescence studies (Pattamatta *et al.*, 2014).

3.4 Validation of the model

The past studies on droplet-hot wall interactions and drop-on-drop impingement onto isothermal surfaces, are chosen for the assessment of present numerical formulation. The details of validation cases are explained briefly in the following sections.

3.4.1 Single droplet impact onto heated surface

Herbert *et al.* (2013a) conducted experiments to study the evaporation dynamics of a single droplet collision onto a heated surface. Saturated FC-72 (Perfluorohexane) liquid in its vapor environment and Chromium surface were used for these studies. The droplet of 1.02 mm diameter was impacted with a velocity of 0.262 m/s on a wall superheat ΔT of 13K which corresponds to a Weber number of $We \sim 14$ and Reynolds number of $Re \sim 956$. Experiments were followed by a numerical simulation using a contact line evaporation model with a solid surface coupling.

The above depicted case is used for the validation of the numerical model. A grid independence study was conducted in domain size of 4 mm x 2 mm with uniform grid of cell sizes 4 micron (1000 x 500), 6 micron (664 x 334) and 8 micron (500 x 250). The grid sizes of 6 and 8 micron were showing a deviation of 2 % and 5 % in estimating spread and heat flow rate respectively when compared to a 4 micron grid size. The results are shown in the Figures 3.2 and 3.3.

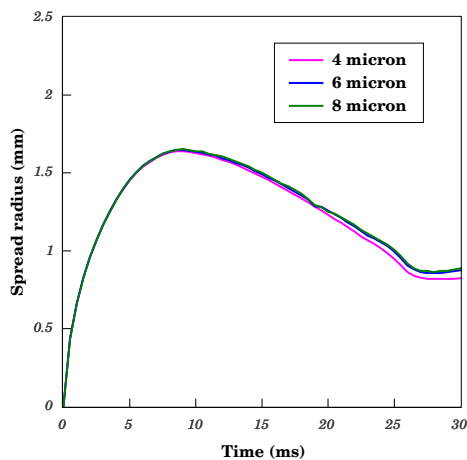


Fig. 3.2: Spread radius versus time

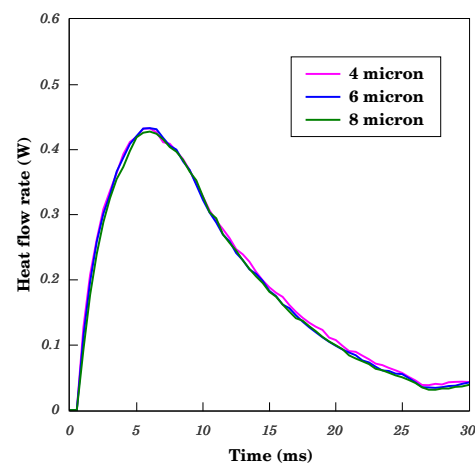


Fig. 3.3: Heat flow versus time

The present simulation with a uniform grid of 8 micron with maximum Courant number (Co) ~ 0.1 are compared to the experiments. The dynamic contact angle is calculated from the contact line evaporation as explained in the evaporation model. The results obtained from the present numerical simulations are well within the range of the experimental results as shown in Figures 3.4 and 3.5.

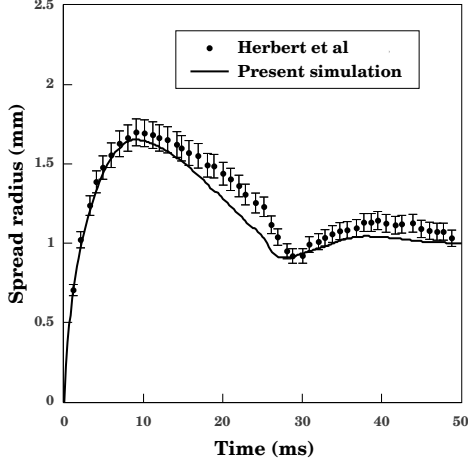


Fig. 3.4: Spread radius versus time

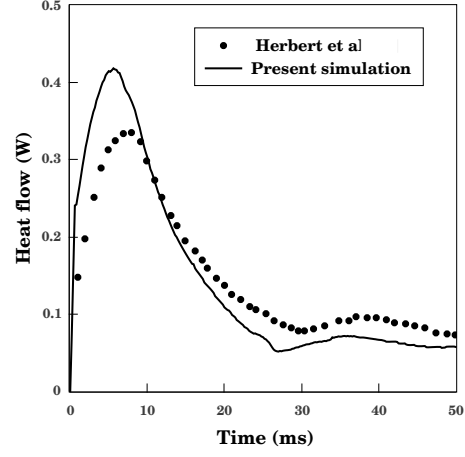


Fig. 3.5: Input heat flow versus time

3.4.2 Drop-on-drop impingement upon isothermal surface

The experimental investigation of falling droplet onto a sessile drop on a non-heated hydrophobic surface were conducted by Wakefield *et al.* (2016). Weber number (impacting velocity) of falling droplet is chosen as parameter and for different values of We ranging from 1 to 275, concentric impacts of water droplet onto a Teflon substrate were performed. The dynamic behaviour of drop-on-drop during the phases of coalescence, spreading and receding were presented and compared with a theoretical model based on the energy conservation principle.

For present validation, one case ($We \sim 219$) of drop-on-drop impact was considered and compared with the experimental observation in terms of spread factor. The conservation of mass and momentum equations are solved and dynamic contact angle is determined using Kistler's dynamic contact angle model (Šikalo *et al.*, 2005). Kistler's model considers the dependence of dynamic contact angle θ_D on the contact line velocity U_{cl} and observed apparent contact angle θ_a during the phase.

$$\theta_D = f_{Hoff}(Ca + f_{Hoff}^{-1}(\theta_a)) \quad (3.15)$$

Where Hoffman's function $f_{Hoff}(x)$ is defined as

$$f_{Hoff}(x) = \cos^{-1} \left\{ 1 - 2 \tanh \left[5.16 \left(\frac{x}{1 + 1.31Ca^{0.99}} \right)^{0.706} \right] \right\} \quad (3.16)$$

Capillary number Ca is given, in terms of contact line velocity U_{cl} , as

$$Ca = \frac{\mu U_{cl}}{\sigma} \quad (3.17)$$

The contact line velocity U_{cl} is assumed as the velocity component at the interface near the solid wall which is normal to the contact line and tangential to the surface. More details are provided in reference (Schremb *et al.*, 2017). The apparent contact angle θ_a takes the advancing contact angle θ_{ad} and receding contact angle θ_{re} during the spreading and retracting phases respectively. The phases are realized from the direction of the contact line velocity U_{cl} .

A drop size of 2.92 mm with a velocity of 2.353 m/s is impacted onto equal volume sessile drop on a Teflon surface (static contact angle $\theta \sim 117^\circ$) which corresponds to a Weber number of $We \sim 219$ and Reynolds number of $Re \sim 7138$. With the understanding from the previous studies (Šikalo *et al.*, 2005), an advancing contact angle $\theta_{ad} \sim 140^\circ$ and receding angle $\theta_{re} \sim 90^\circ$ are considered such that the dynamics can be captured during the impact. The domain size of 12 mm x 15 mm with three uniform grids with minimum cell sizes of 10 micron (1200 x 1500), 20 micron (600 x 750) and 30 micron (400 x 500) were used for the grid sensitivity study as given in the Figure 3.6. It was found that the percentage deviation in spread factor was less than 5% for both 20 and 30 micron when compared to 10 micron grid size. A good prediction of spread factor was obtained in the simulations (with 20 micron and maximum $Co \sim 0.1$) when compared to the experimental results as shown in the Figure 3.7.

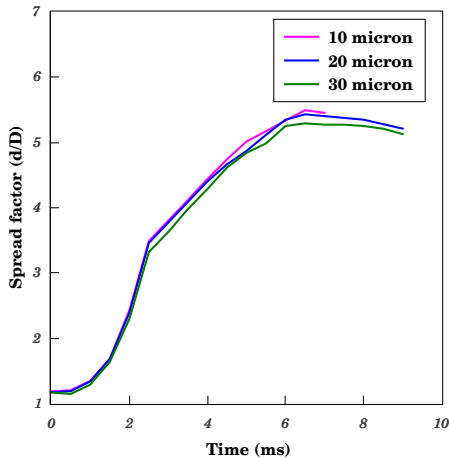


Fig. 3.6: Grid independence study

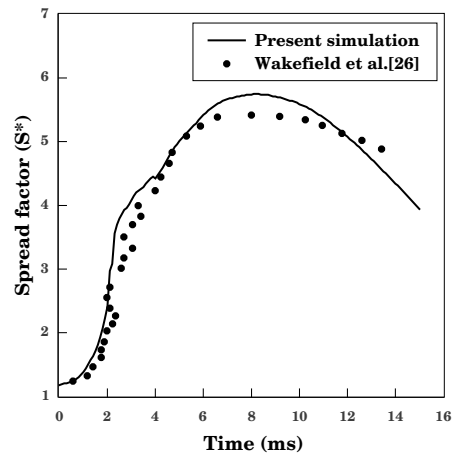


Fig. 3.7: Spread factor versus time

Table 3.1: Properties of FC-72 (Perfluorohexane) at saturation pressure of 1 bar

Property	Symbol	Liquid	Vapour
Density, kg/m^{-3}	ρ	1619.82	13.36
Dynamic viscosity, $kg/(m\ s)$	μ	$4.5306 \cdot 10^{-4}$	$9.4602 \cdot 10^{-6}$
Specific heat capacity, $J/(kg\ K)$	c_p	1098.41	885.04
Thermal conductivity, $W/(mK)$	k	0.05216	0.00864
Saturation temperature, K	T_{sat}	329.75	
Latent heat of vaporization, J/kg	h_{lv}	84515	
Surface tension, N/m	σ	0.008273	

3.5 Present simulation - Drop-on-drop impact onto heated surfaces

The validated numerical model with contact line evaporation and dynamic contact line motion is used to perform the drop-on-drop simulations onto heated surface. Saturated FC-72 liquid surrounded by its saturated vapor is impinged onto the heated chromium surface (wetting surface with equilibrium contact angle of $\theta \sim 35^\circ$). All the simulations are done within the splashing limit of the droplet i.e., less than $We \sim 50$ and superheat less than $\Delta T \sim 15K$ (Herbert *et al.*, 2013a). The thermophysical properties are assumed to be constant within the used superheat range and the values are given in Table 3.1. When compared to single drop impact, drop-on-drop collision needs high-end computation facility and time. In order to reduce the computation effort, a 2-D axisymmetric domain is considered for the simulations with an assumption of concentric head-on collision of droplets. The details of the domain size and boundary conditions are given in Figures 3.8 and 3.9.

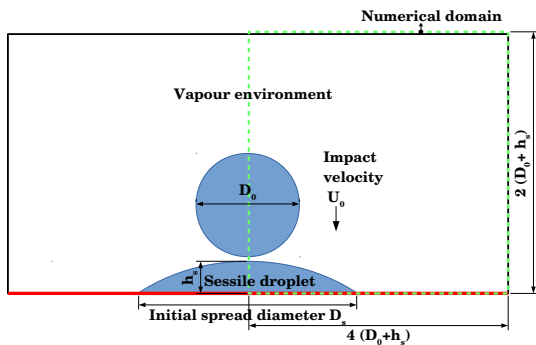


Fig. 3.8: Drop-on-drop configuration

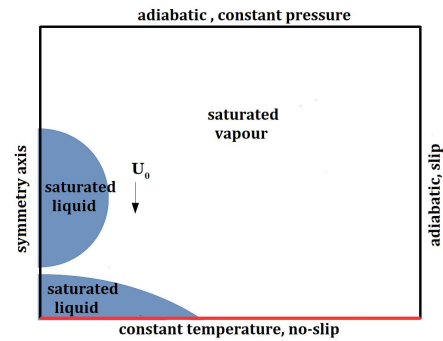


Fig. 3.9: Numerical domain with boundary conditions

For the determination of input heat transfer, the temperature gradient is calculated

from the cells near wall boundary. Thus, these values are strongly dependent on thickness during deformation of drop and cell size of the grid. Among the cases used in the present work, $We \sim 40$ is associated with the smaller value of diameter and thickness during deformation. Therefore, the study of grid independence is done with the case of $We \sim 40$ where a drop diameter of 0.3829 mm is impinged with a velocity of 0.7304 m/s on a wall superheat of $\Delta T \sim 10K$. A grid independence study is conducted in a domain of 2 mm x 1 mm with a uniform grid of cell sizes 2 (1000 x 500), 4 (500 x 250) and 6 micron (334 x 166).

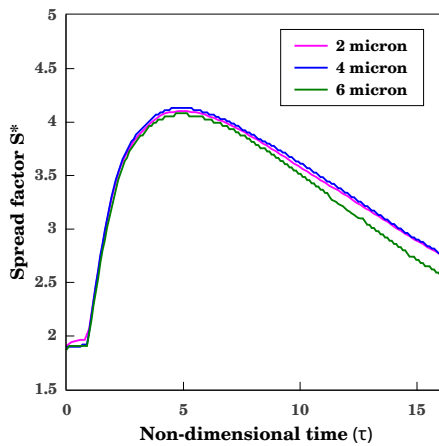


Fig. 3.10: Spread factor versus time

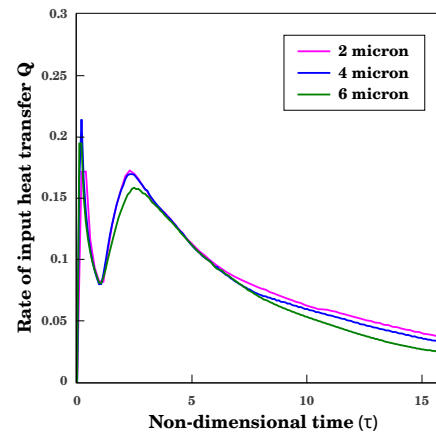


Fig. 3.11: Input heat flow versus time

Table 3.2 presents the average percentage error for the grid resolutions of 4 and 6 micron compared to 2 micron. The comparison of spread factor and heat transfer between these grid sizes, are given in Figures 3.10 and 3.11. The results showed that the percentage variation between 2 and 4 micron cell sizes are found to be less than 1% and 6 % for spread factor and input heat transfer calculations respectively. As a compromise for appropriate estimation of the values and reduced computational effort, a grid resolution of 4-micron is adopted for all the studies presented in this work.

Table 3.2: Percentage error in spread factor and heat transfer compared to grid size of 2-micron

Grid resolution	Error (percentage) in Spread factor	Error (percentage) in Input heat rate
4 micron	0.6	5.8
6 micron	8	16

The configuration of drop-on-drop impingement is achieved by impinging a single drop and making it sessile on the surface after which another droplet of equal volume (diameter) is impinged onto sessile drop (i.e., Radius ratio $R^* \sim 1$). The moment, impacting drop collides into static droplet, surface is heated with the given wall superheat. To understand the spread and evaporation dynamics of drop-on-drop impact, it is compared to a single drop impingement under same conditions. A drop diameter of 1.021 mm with impacting velocity of 0.2739 m/s and wall superheat of 10 K are used for the comparison. This configuration corresponds to a Weber number of $We \sim 15$, Bond number of $Bo \sim 0.5$, Reynolds number of $Re \sim 1000$ and Jakob number of $Ja \sim 0.13$. This is followed by the study on the effects of different influencing parameters on the evaporation dynamics of drop-on-drop impact. Weber number, Bond number, Jakob number and Radius ratio are chosen as parameters. In each parameter study, three cases were considered to evaluate its effect on the dynamics of the process.

3.6 Results and Discussion

3.6.1 Drop-on-drop impingement onto heated surface

During the process of drop-on-drop impact, different phenomena can be observed such as mixing of the two droplets, spreading of the drop for a while and retracting back as a whole after sometime. For a better perception and understanding of the event, impingement process is divided into three phases i.e., coalescing, advancing and receding phases. In the present work, a coalescing phase is defined as the mixing process of impacting drop with the sessile one. An advancing phase is one in which the drop will advance in the direction of increasing spread on the surface. A receding phase is realized as a phase of the drop shrinking back from its maximum spread position.

It is observed that the merging of droplets is taking place in two ways. Initially, the impacting drop will fuse into sessile drop without causing any motion in it. After a while, there is a simultaneous mixing and advancing action taking place in the process due to the momentum transfer between the droplets. Here, the former stage is

considered as a coalescing phase and the later one is included in advancing phase. From the previous studies of single droplet impact, it is ascertained that the advancing phase is influenced by inertial forces while the receding behaviour depends on capillary action. Thus an advancing regime is associated with comparatively high velocities than a receding phase. These lead to high convective heat transfer rates during the spreading stage. A similar trend is observed for the case of drop-on-drop impingement during study. The droplet behaviour of case with $We \sim 40$, $Bo \sim 0.5$, $Ja \sim 0.13$ and $R^* \sim 1$ during drop-on-drop impingement along with the temperature contours are shown in Figure 3.12.

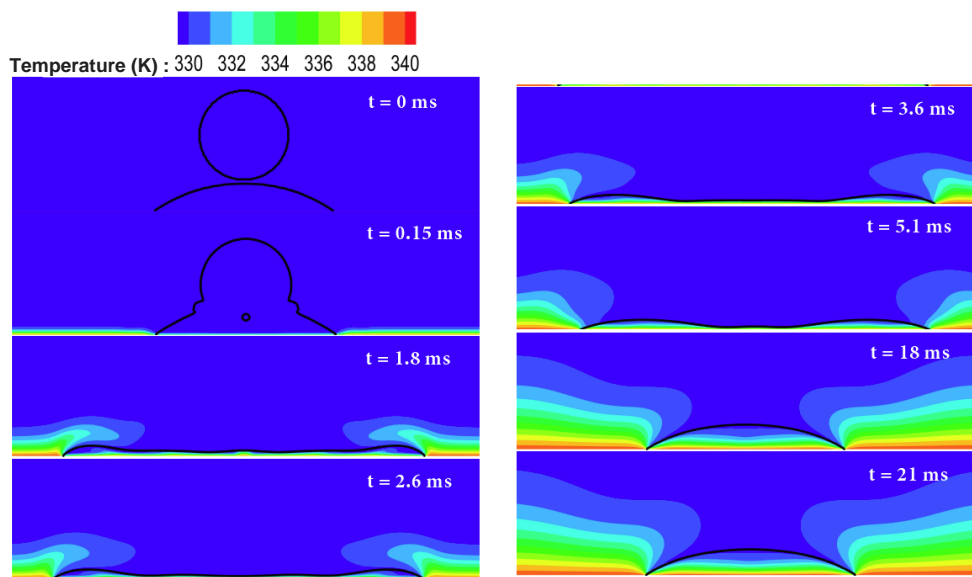


Fig. 3.12: Drop-on-drop impingement process with iso-surface ($\alpha = 0.5$) and temperature contours

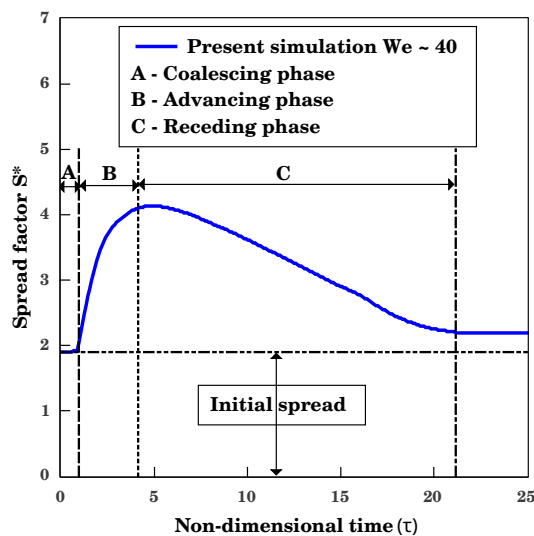


Fig. 3.13: Spread factor versus time

An initial spread is realized for the cases of head-on collisions due to the presence of the sessile drop. In the context of drop-on-drop impingement, the completion of coalescing, advancing and receding phases can be termed as an initial cycle followed by cycles consisting of only advancing and receding regimes. The variation of spread with respect to time along with identified phases, is presented in Figure 3.13.

3.6.2 Comparison of drop-on-drop impingement to single drop impingement

To discern the process of drop-on-drop impact from single droplet impingement, simulations are performed under same conditions and analysed. We ~ 15 , Bo ~ 0.5 , Re ~ 1000 , Ja ~ 0.13 and $R^* \sim 1$ (drop-on-drop) are used for the both cases where droplet has a diameter of 1.021 mm, impacting velocity of 0.2739 m/s, wall superheat of 10 K with a gravity conditions equivalent to $9.81m/s^2$. The domain size of 5.6 mm x 2.8 mm (drop-on-drop case) and 4 mm x 2 mm (single droplet case) with a uniform grid of 4 micron was used. Under these circumstances, a comparison is made in terms of spread factor, input and evaporation heat flux with the classified regimes as shown in Figures 3.14 to 3.17.

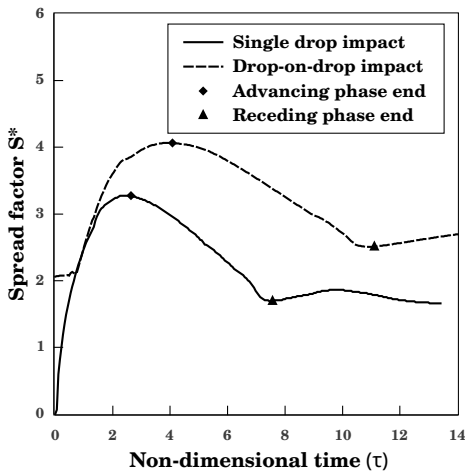


Fig. 3.14: Spread factor versus time

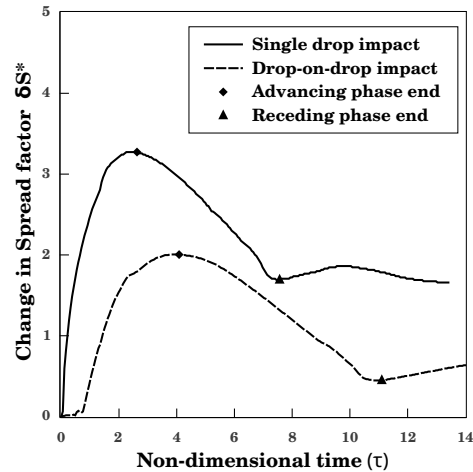


Fig. 3.15: Net spread factor versus time

Regarding spread dynamics, an initial cycle of drop-on-drop impingement consists of coalescing, advancing and receding phases while a single drop impact associated with only regimes of advancing and receding. As expected and given in the Figure 3.14, the drop-on-drop case exhibits a maximum spread factor compared to single drop

impingement owing to the fact that it contains more volume. Furthermore, the duration of phases is increased for the drop-on-drop collision. However, the change in spread i.e., the difference between instantaneous and initial spread is more in the case of single drop impact which is shown in the Figure 3.15. Note that the spread factor is defined as an instantaneous spread diameter normalized with impact droplet diameter. For single drop impact, the only resisting medium during deformation is vapour while in case of drop-on-drop collision, the liquid resistance of sessile drop is added to the former one and leading to low magnitudes of change in spread. As a result of this increased resistance, the rate of spread is low for drop-on-drop collision further gives rise to long periods of advancing and receding phases.

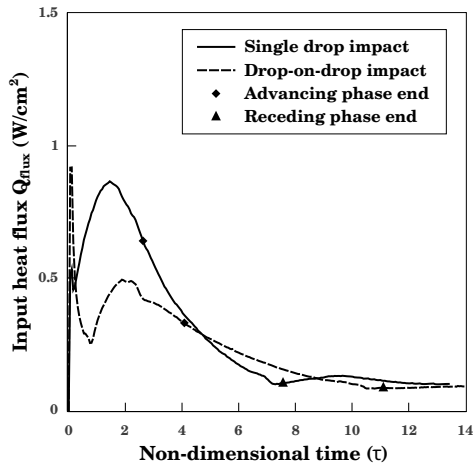


Fig. 3.16: Input heat flux versus time

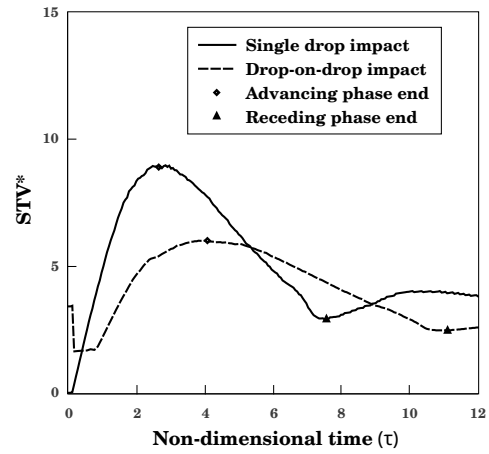


Fig. 3.17: STV ratio versus time

Coming to the evaporation dynamics, the heat transfer into drop during the impact i.e., input heat flux as shown in Figure 3.16 is found to decrease for the event of drop-on-drop collision in contrast to single drop impingement. As shown in Figure 3.17, reduction in spread surface area-to-volume ratio (STV) during the head-on collision of the drops, explains this behaviour of heat transfer. As it is a dimensional quantity, a dimensionless surface area-to-volume ratio (STV*) is introduced which can be obtained by the product of STV and the impacting drop diameter. The parameter STV* can be conceived as inverse of the thickness factor (h/D) which was used in the past studies of droplet impingement studies (Lunkad *et al.*, 2007). Thus, it reflects the variation of thermal resistance experienced by the deforming droplet during the process. A close observation at pre-coalescing phase of drop-on-drop reveals a high heat transfer into sessile drop due to high STV* ratio. The moment when a impacting drop collides into sessile one, STV* ratio reduces giving rise to low input heat transfers. As it was

previously quoted, the maxima in heat transfer rates are realized during advancing phase of single drop which is the same for the case of multiple droplet impact. Also the area under the curve in Figure 3.16, will provide an estimation of total heat transfer into drop for a given time period. Upto advancing phase, cumulative heat transfer of single drop impact is higher than the value of the drop-on-drop impingement case. However, the multiple drop has higher heat transfer during receding phase contrary to single drop. Actually, this is a phase-wise comparison and note that the cycle period for drop-on-drop is more compared to single drop impingement. So, these high values are due to the increased duration of receding i.e., slow pace of retracting phase. If the comparison is made with respect to time, heat transfers are always greater for single drop impact than multiple drop. Nevertheless, both cases are associated with almost same magnitudes of heat transfer rates at the end of their cycles which can be observed from the Figure 3.16.

3.6.3 Effect of influencing parameters on drop-on-drop impingement over heated surfaces

With the observations from past studies (Rein, 1993; Chandra and Avedisian, 1991; Herbert *et al.*, 2013b), some of the influencing parameters are identified to study their effect on the spread and evaporation dynamics of drop-on-drop impact over hot surfaces. Weber number (We), Bond number (Bo), Jakob number (Ja) and Radius ratio (R^*) are chosen as parameters. In the present work, the density and dynamic viscosity of the gas phase can be completely neglected against the corresponding properties of the liquid phase. So, all the dimensionless numbers used are defined using the liquid properties. During each study, three values are considered and compared for variables. Droplet diameter, impact velocity and gravitational acceleration are changed to obtain different values of the parameters so that there is no change in fluid properties. Hence, there is a possibility that different values of droplet diameters may involve for a given configuration of impact. For the sake of comparison between the cases, measurements are made in terms of spread factor, non-dimensional time, input heat and evaporation heat transfers. Spread factor (S^*) is defined as the ratio of instantaneous spread diameter (d) to the impacting droplet diameter (D_0)

$$Spread\ factor\ S^* = \frac{d}{D_0} \quad (3.18)$$

while non-dimensional time (τ) is given as a ratio of actual time to spreading time scale.

$$\text{Dimensionless time } \tau = \frac{tU_0}{D_0} \quad (3.19)$$

Similarly for the input and corresponding evaporation heat transfers, their cumulative values are non-dimensionalised by heat required for total drop evaporation. These non-dimensional input and evaporation heat (which is also the dimensionless evaporated mass) transfers are designated by Q^* and Q_e^* . Dimensionless input heat Q^* is defined as the ratio of cumulative heat input into the drop to the total heat required to evaporate the droplet.

$$\text{Dimensionless Input heat } Q^* = \frac{6Q_{cu}}{\rho_l \pi (D_0^3 + D_1^3) h_{lv}} \quad (3.20)$$

Dimensionless evaporation heat Q_e^* is defined as the ratio of cumulative evaporation heat of the droplet to the total heat required to evaporate the droplet.

$$\text{Dimensionless evaporation heat } Q_e^* = \frac{6Q_{ecu}}{\rho_l \pi (D_0^3 + D_1^3) h_{lv}} \quad (3.21)$$

Where Q_{cu} is cumulative heat input calculated from the temperature gradient near the wall over a time period (t) where as the Q_{ecu} , cumulative evaporation heat, is obtained from the mass source term defined in the Evaporation model section. D_0 and D_1 are impacting and sessile droplet diameters respectively.

Note that all the impingement studies are carried out in superheated deposition regime (maximum values of $We \sim 40$ and $\Delta T \sim 15K$). All the parameter calculations are based on liquid properties of the FC-72 and in every study attempts were made to extract the effect of the parameter on hydrodynamic and heat transfer behaviour of the drop impact.

Effect of Weber number

Weber number is defined as the ratio of inertial forces to the capillary forces and found to be very effective parameter for the droplet impact studies.

$$\text{Weber number } (We) = \frac{\text{Inertial forces}}{\text{Capillary forces}} = \frac{\rho_l U_0 D_0^2}{\sigma} \quad (3.22)$$

The spread and morphological behaviour of the droplets during the impingement process, will strongly depends upon Weber number. In order to conceive its effect on drop-on-drop impingement over hot surface, three values of Weber number are used i.e., We 20, We 30 and We 40 are used. In every case, remaining dimensionless parameters, $Re \sim 1000$, $Ja \sim 0.130$ ($\Delta T \sim 10$ K), $Bo \sim 0.5$ and $R^* \sim 1$ are maintained constant. The droplet diameters and impact velocities corresponding to the Weber numbers are provided in Table 3.3.

Table 3.3: Droplet configuration for different Weber number cases

Weber number (We)	Droplet diameter (D_0) in mm	Droplet impact velocity (U_0) in m/s
20	0.7659	0.3652
30	0.5106	0.5478
40	0.3829	0.7304

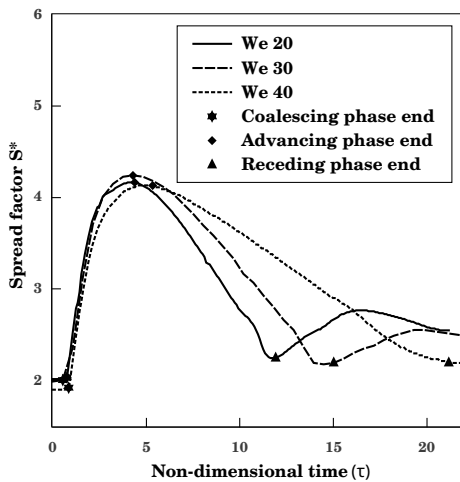


Fig. 3.18: Spread factor versus time

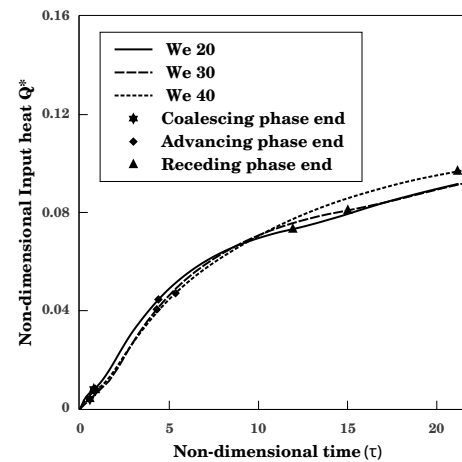


Fig. 3.19: Input heat versus time

As the cases are associated with different droplet size and impacting conditions, a suitable domain sizes i.e., 4.4 mm x 2.2 mm (We 20), 2.8 mm x 1.4 mm (We 30) and 2 mm x 1 mm (We 40) with a uniform grid of cell size 4 micron are considered for this parameter study. A higher value of Weber number indicates large impacting energy due to increased impinging velocity for a given fluid. Under isothermal conditions, drop impact of high Weber number (within splashing limit) yields large value of maximum spread. Also, the duration of advancing and receding phases will be higher interms of

non-dimensional time scale. However due to the simultaneous wall heating, it is found that there is no much difference in maximum spread factor for the given Weber number cases as shown in Figure 3.18.

As explained above, the duration of advancing and receding phases are high for $We \sim 40$ compared to other configurations which will enhance the input and evaporation heat transfer as given in Figures 3.19 and 3.20. Moreover, the spread surface area-to-volume (STV^*) ratio will also plays a role in transferring heat into droplet. From the figures 3.19, 3.20 and 3.21, it can be observed that for a higher Weber number case (We 40), a low input heat transfer is recorded during the advancing phase compared to other cases. While in the receding phase, the heat transfer is improved as the surface area-to-volume ratio (STV^*) is increased. Considering all these effects, increase in Weber number enhances the input heat transfer and promotes high evaporation rate which is followed by decrease in the spread as expected. The slopes of dimensionless input and

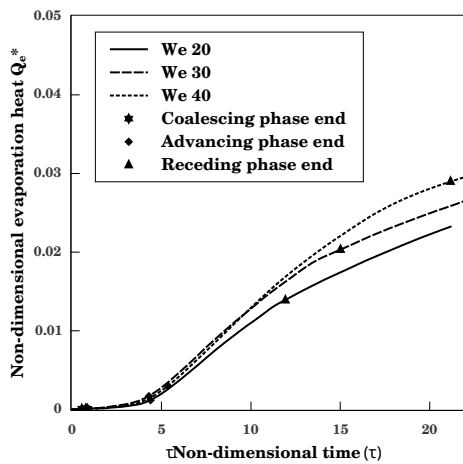


Fig. 3.20: Evaporation heat versus time

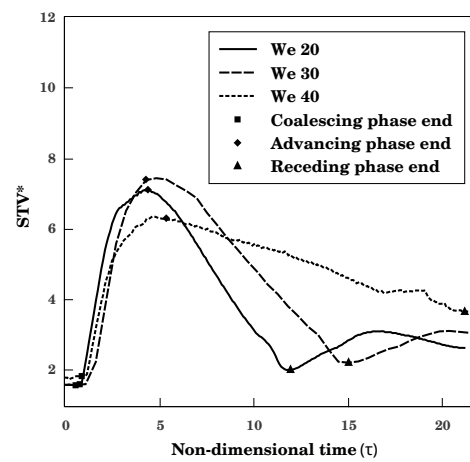


Fig. 3.21: STV^* ratio versus time

evaporation heat curves in the Figures 3.19 and 3.20 provides the information of heat transfer rates. A phase-wise comparison reveals that there is no considerable effect of Weber number on duration, spread and evaporation dynamics in the coalescing phase. Observations made in the advancing and receding phases reveals that there is high rate of input heat transfers during advancing phase compared to receding phase due to the high velocities associated with the droplet. However, rate of evaporation heat transfer showed an increasing trend during the receding phase.

Effect of Jakob number

Along with the Weber number, the wall superheat will be one of the most influencing parameters for impact studies upon heated surfaces. Depending upon degree of superheat, it is realized that impact phenomena on a hot surface can be categorized into different regimes namely convective, nucleate and film boiling (Chandra and Avedisian, 1991). The present study comes under convective boiling which can be called as superheated deposition where maximum superheat is below 15 K. The wall superheat is non-dimensionalised using latent heat of vaporization of the fluid which is termed as Jakob number.

$$Jakob\ number\ (Ja) = \frac{wall\ superheat}{latent\ heat} = \frac{c\Delta T}{h_w} \quad (3.23)$$

Three Jakob number values of 0.075, 0.130 and 0.175 corresponding to different superheats, are used in the present study and details of the cases are given in Table 3.4. Droplet configuration is maintained at $We \sim 40$, $Re \sim 1000$, $Bo \sim 0.5$ and $R^* \sim 1$, during this parameter study. A domain of 2 mm x 1 mm with uniform grid resolution of 4 micron is used for all the cases.

Table 3.4: Case details of different Jakob numbers

Jakob number (Ja)	Wall superheat (ΔT) in K
0.075	5.8
0.130	10
0.175	13.5

The phase contours with corresponding time period, at the maximum spread position for the three cases are presented in Figure 3.22 which concludes the strong dependence of spread factor on wall superheat. From the Figure 3.23, it is observed that a high Jakob number results in large heat transfer rates which ultimately improves evaporation of mass from the droplet. Owing to this behaviour, spread factor decreases consequently reducing the duration of cycle. An increasing trend of input and evaporation heat transfers through out the cycle is shown in Figures 3.24 and 3.25. Also, the slope of the heat transfer curves are more steep in the region of advancing

phase because of its high velocities. The dominant inertial forces are accounted for the high velocities during the advancing phase.

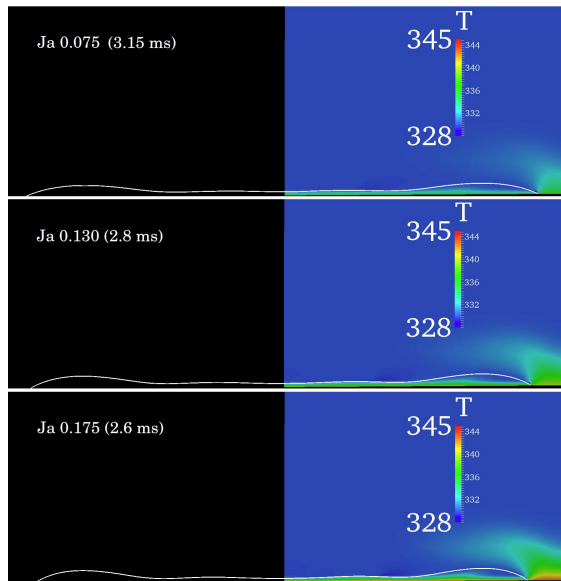


Fig. 3.22: Maximum spread diameter at different Jakob numbers

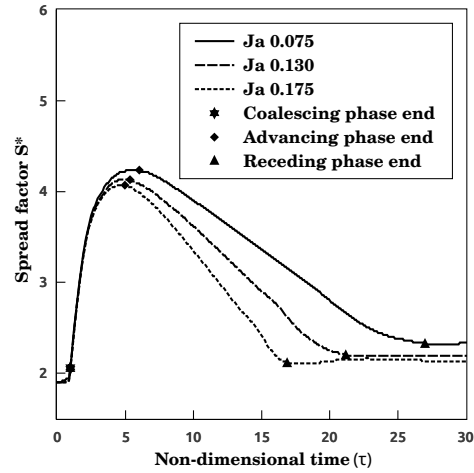


Fig. 3.23: Spread factor versus time

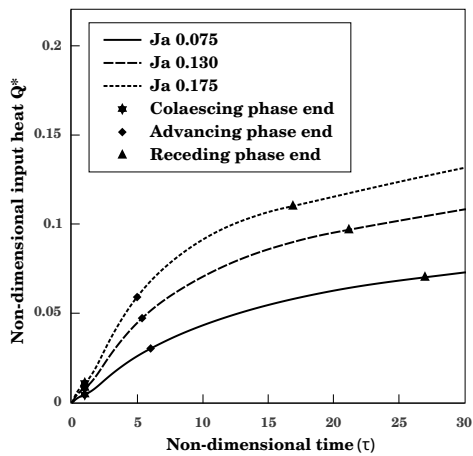


Fig. 3.24: Input heat versus time

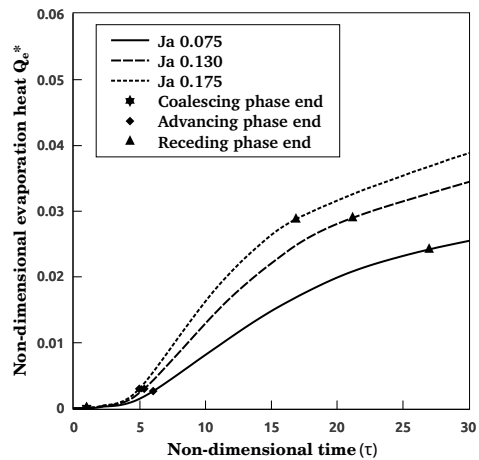


Fig. 3.25: Evaporation heat versus time

While in receding phase, velocities are small in magnitude which result in less rate of heat transfer thereby decrease in slopes of curves. Variation of Jakob number does not cause any change in the coalescing phase as it's duration is limited to small time periods. However, advancing and receding phase durations are found to be strongly dependent on wall superheat.

Effect of Bond number

The gravity effects on the impingement process can be captured by varying Bond number. It is defined as a ratio of body forces to the surface tension forces.

$$\text{Bond number } (Bo) = \frac{\text{Body forces}}{\text{Capillary forces}} = \frac{\rho_l g D_0^2}{4\sigma} \quad (3.24)$$

Different values of Bond number are achieved by impinging a droplet under different gravity conditions. A diameter of 0.3829 mm, impact velocity of 0.7304 m/s with 10 K wall superheat are used for the parameter study. A domain of 2 mm x 1 mm with uniform grid of cell size 4 micron is used for all the cases. This results into a $We \sim 40$, $Ja \sim 0.130$, $Re \sim 1000$ and $R^* \sim 1$ and the details of gravity conditions for the cases are presented in Table 3.5.

Table 3.5: Case details of different Bond numbers

Bond number (Bo)	Acceleration due to gravity (g) in m/s²
0.2	3.91
0.5	9.79
1	19.59

A rise in gravity increases the impact energy of the drop due to which the spread factor will improve. As there is a simultaneous wall heating, a case with increased spread will result in better heat transfer rates during the process. This behaviour is presented for the given cases of Bond number in Figures 3.26 to 3.28 where increase in Bond number gives rise to high spread factor thereby promoting heat transfers.

As the wall superheat is constant for all the cases, evaporation dynamics strongly depends on the hydrodynamics of the drop. More the spread, higher the input and evaporation heat transfers during the impact process. Coming to the onset of phases, coalescing phase is undisturbed due to the variation of this parameter while advancing and receding phases are slightly increased with rise in Bond number value.

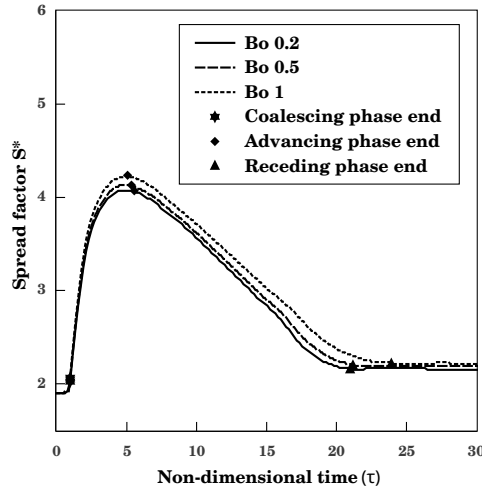


Fig. 3.26: Spread factor versus time

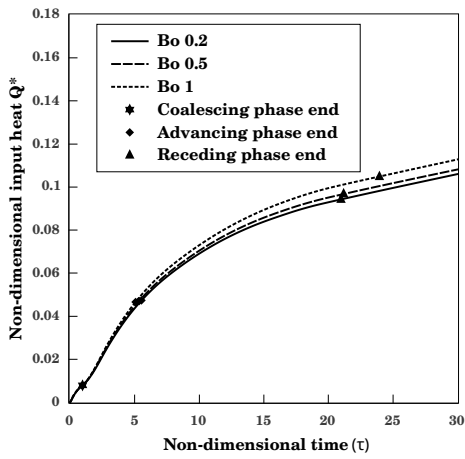


Fig. 3.27: Input heat versus time

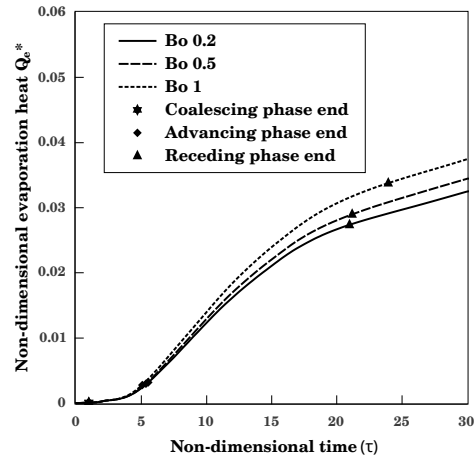


Fig. 3.28: Evaporation heat versus time

Effect of sessile droplet radius

The presence of sessile droplet in the drop-on-drop configuration, differentiates it from single droplet phenomena. From the comparison, it is understood that the heat transfer rate declines due to the existence of sessile drop. To get more insights of its effect on the process, the radius of sessile droplet is changed. A dimensionless parameter namely Radius ratio (R^*) is taken and defined as the ratio of sessile drop radius to the impacting droplet radius.

$$\text{Radius ratio } (R^*) = \frac{\text{Sessile droplet radius}}{\text{Impacting droplet radius}} = \frac{R_1}{R_0} \quad (3.25)$$

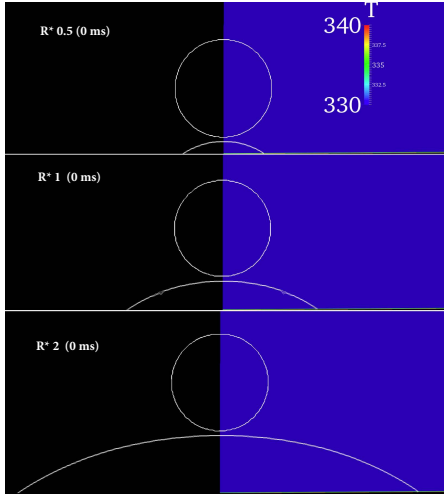


Fig. 3.29: Sessile drop radius: Initial stage

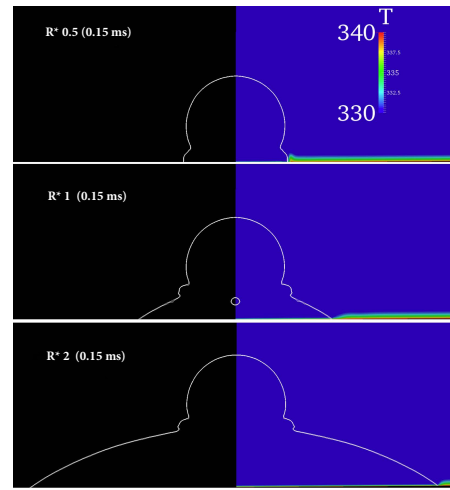


Fig. 3.30: Coalescing stage

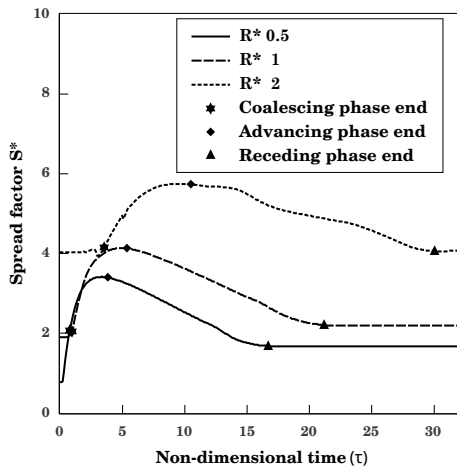


Fig. 3.31: Spread factor versus time

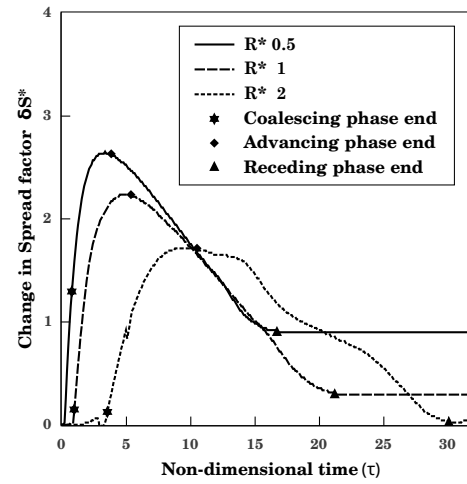


Fig. 3.32: Net spread factor versus time

A droplet with a diameter (D_0) of 0.3829 mm, impact velocity of 0.7304 m/s is impinged onto sessile drop with varying diameters (radii) of $0.5D_0$, D_0 and $2D_0$ where the wall superheat is maintained at 10 K. Thus, these cases corresponds to R^* values of 0.5, 1 and 2 respectively, where other dimensionless parameters such as $We \sim 40$, $Ja \sim 0.130$, $Bo \sim 0.5$ and $Re \sim 1000$ are remained constant. The domain sizes of 2 mm x 1 mm ($R^* \sim 0.5$ and 1) and 4 mm x 2 mm ($R^* \sim 2$) with a uniform grid resolution of 4 micron is used for the cases. The phase contours along with temperatures are indicated in the Figures 3.29 and 3.30. The spread factor (S^*) and change in spread factor (δS^*) variation with dimensionless time is presented in Figures 3.31 and 3.32. It has been observed that an increasing diameter of sessile droplet is reducing the overall change in spread factor. Thus, the enhancement in spread factor (δS^*) is more for the case of smaller diameter as it offers little resistance to flow and easy to coalesce. Because of

which, the duration of coalescing phase is increased with rise in the value of sessile droplet diameter. Moreover, the heat transfers values are also showed a declining trend with the diameter increase as given in Figures 3.33 and 3.34.

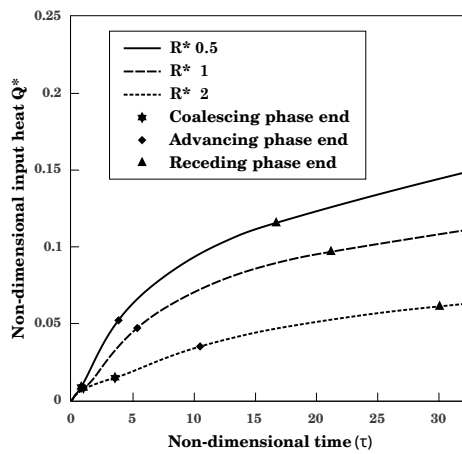


Fig. 3.33: Input heat versus time

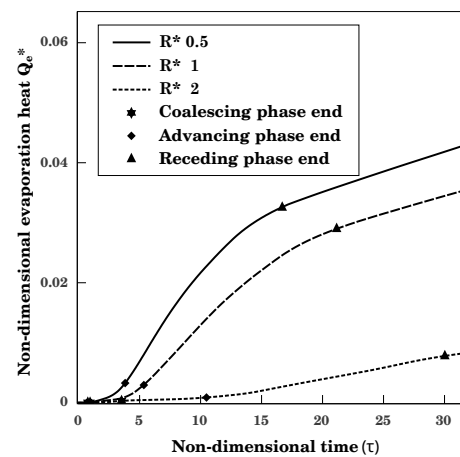


Fig. 3.34: Evaporation heat versus time

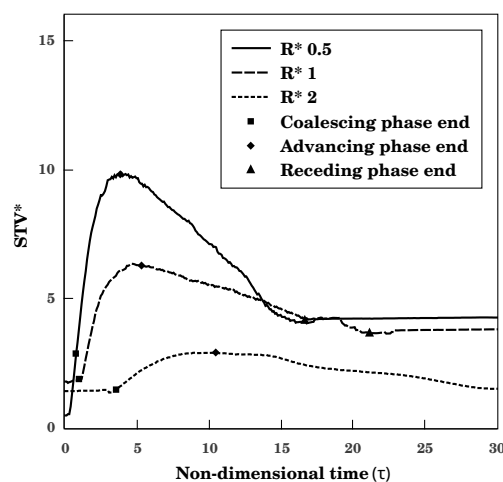


Fig. 3.35: STV ratio versus time

This behaviour of the process is best explained from the thermal resistance's point of view. The decrease in surface area-to-volume ratio represents an increase in thermal resistance which eventually reduce the input heat transfer into the droplet as shown in Figure 3.35. In addition, a decrease in spread factor and velocities also reduces the heat transfer creating an overall effect on evaporation during the process. The onset of phases i.e., advancing and receding are also changed, giving rise to different patterns of spread and evaporation associated with the phenomena.

3.6.4 Analytical modelling

Maximum spread

The maximum spread during the impingement process can be conveniently modeled using the conservation of energy principle. This approach has been used for single droplet impact onto solid surfaces by Chandra and Avedisian (1991) and later modified by Pasandideh-Fard *et al.* (1996) and Batzdorf (2015). Similarly, this method is extended to head-on collisions over a non-heated surface by Wakefield *et al.* (2016).

For setting up an energy balance, two instances during the droplet impingement are considered i.e., initial state before impact and the instant of maximum spread. The corresponding energies at these stages are shown in Figure 3.36. For impacting droplet, the initial kinetic and potential energies are given as

$$KE_{I,1} = \frac{1}{2}mU_0^2 = \frac{\pi}{12}\rho D_0^3 U_0^2 \quad (3.26)$$

$$PE_{I,1} = mg \left(\frac{D_0}{2} + h_s \right) \quad (3.27)$$

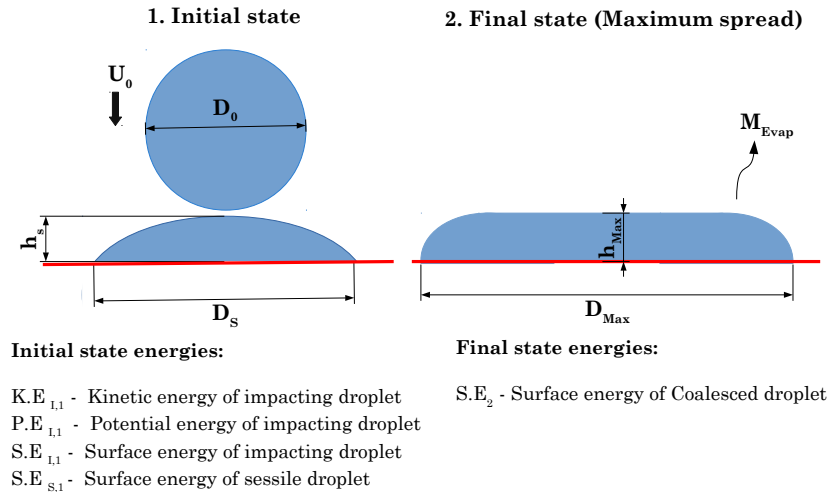


Fig. 3.36: Energies associated with droplets at initial and maximum spread

Here, sessile droplet is assumed as a cylindrical film with base diameter D_s and equivalent thickness h_s which is obtained by conservation of volume.

$$h_s = \frac{2}{3} \frac{c^3 D_0^3}{D_s^2} \quad (3.28)$$

Note that the sessile drop diameter is taken as c (constant) times the impacting droplet (D_0).

The initial surface energy of impacting drop is given as

$$SE_{I,1} = \sigma_{lv}\pi D_0^2 \quad (3.29)$$

For sessile drop, the initial surface energy is

$$SE_{S,1} = \frac{\pi}{4}D_s^2\sigma_{sl} - \frac{\pi}{4}D_s^2\sigma_{sv} + \pi D_s h_s \sigma_{lv} + \frac{\pi}{4}D_s^2\sigma_{lv} \quad (3.30)$$

using Young's relation

$$\sigma_{sv} = \sigma_{sl} + \sigma_{lv}\cos\theta \quad (3.31)$$

results in

$$SE_{S,1} = \frac{\pi}{4}\sigma_{lv}D_s^2(1 - \cos\theta_1) + \pi\sigma_{lv}D_s h_s \quad (3.32)$$

Similarly, the surface energy of the droplet at the instant of maximum spreading is

$$SE_2 = \frac{\pi}{4}\sigma_{lv}D_{max}^2(1 - \cos\theta_2) + \pi\sigma_{lv}D_{max}h_{max} \quad (3.33)$$

Using mass conservation, the thickness at the maximum spread h_{max} is

$$h_{max} = (1 + c^3)(1 - Q_e^*)\frac{2}{3}\frac{D_0^3}{D_{max}^2} \quad (3.34)$$

Q_e^* represents the non-dimensional evaporation heat (mass) till the maximum spread.

From conservation of energy principle

$$KE_{I,1} + PE_{I,1} + SE_{I,1} + SE_{S,1} = SE_2 + W_{dis} \quad (3.35)$$

Where W_{dis} is the dissipation work derived by Chandra and Avedisian (1991) as following

$$W_{dis} = \mu \left(\frac{U_0}{\delta} \right)^2 V_{drop} t_c \quad (3.36)$$

Where V_{drop} is $\pi d_{max} h_{max}$ and time period t_c of the process is scaled in terms of impact

drop diameter D_0 and velocity U_0 (Chandra and Avedisian, 1991) as

$$t_c = a \frac{D_0}{U_0} \quad (3.37)$$

Where a is constant and the characteristic length scale δ has been set equal to thickness h_{max} (Chandra and Avedisian, 1991; Batzdorf, 2015).

Substituting all the terms in equation 3.35 and final non-dimensionalised equation will result in

$$AS_{max}^*{}^5 + BS_{max}^*{}^3 + CS_{max}^* + D = 0 \quad (3.38)$$

where

$$A = \frac{18}{4} a \frac{We}{Re} \frac{1}{(1+c^3)(1-Q_e^*)} \quad (3.39)$$

$$B = 3(1 - \cos \theta_2) \quad (3.40)$$

$$C = -(We + 4Bo + \frac{16c^3Bo}{3S_{in}^*{}^2} + 3S_{in}^*{}^2(1 - \cos \theta_1) + \frac{8c^3}{S_{in}^*} + 12) \quad (3.41)$$

$$D = 8(1+c^3)(1-Q_e^*) \quad (3.42)$$

Where

$$\text{Bond number, Bo} = \frac{\rho_l g D_0^2}{4\sigma_{lv}} \quad (3.43)$$

$$\text{Reynolds number, Re} = \frac{\rho_l D_0 U_0}{\mu} \quad (3.44)$$

$$\text{Weber number, We} = \frac{\rho_l D_0 U_0^2}{\sigma_{lv}} \quad (3.45)$$

$$\text{Maximum spread factor, } S_{max}^* = \frac{D_{max}}{D_0} \quad (3.46)$$

$$\text{Initial spread factor, } S_{in}^* = \frac{D_s}{D_0} \quad (3.47)$$

Maximum spread factor of the parametric cases are calculated theoretically using equation 3.38. Here constants 'a' is taken as 2.67 (Batzdorf, 2015) and c is chosen as 1, 0.5 and 2 for the cases of sessile droplet of radius R_0 , $0.5R_0$ and $2R_0$ respectively. The values of initial spread and evaporation mass are taken from simulation data. It can be noted that the equation 3.38 shows the dependency of maximum spread factor on non-dimensional numbers Re , Bo and We . Also the effect of Jakob number is considered inherently in the form of evaporated mass and changed contact angle from

θ_1 to θ_2 due to superheating. The comparison of theoretical maximum spread to the simulation values is given in Figure 3.37. and both results are in agreement within maximum deviation of 10 %. In addition, the theoretical model is also able to reflect the effects of chosen parameters on the maximum spreading of droplet.

Input heat transfer

From the simulation studies, it is observed that heat transfer during spreading phase is dominated by convection which can be described using a Nusselt number correlation. In reference (Batzdorf, 2015), the spreading process is assumed as a single impinging jet and overall heat transferred during spreading phase is proportional to the convective heat transfer is described as

$$Q^* = 3b \frac{S_{max}^* (S_{max}^* - 1.1) (1 + 0.005 Re^{0.55})^{0.5} Ja}{(S_{max}^* - 0.6) Re^{0.5} Pr^{0.58}} \tau_{max} \quad (3.48)$$

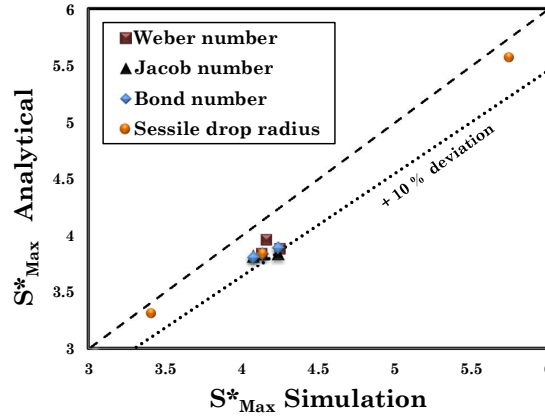


Fig. 3.37: Maximum spread factor: Analytical versus Simulation

The same correlation is also used for the present impingement scenario as in the most cases of drop-on-drop impact the advancing phase is associated with high velocities. The simulation's maximum spread factor (S_{max}^*) and time period τ_{max} are used and the constant $b = 3.4$ is chosen in order to fit the simulation data.

A good approximation of the simulation values are obtained using this correlation which is shown in the Figure 3.38. Most of the results obtained are under a maximum deviation of 20 %. Nevertheless, the case with sessile drop of radius $2R_0$ is over estimated because of its high spread factor contributed by sessile drop radius.

Moreover, there are more coalescing effects involved in this case giving rise to comparatively low convective heat transfer rates. Nevertheless, the correlation is found to be in good agreement with the simulation values for the remaining cases.

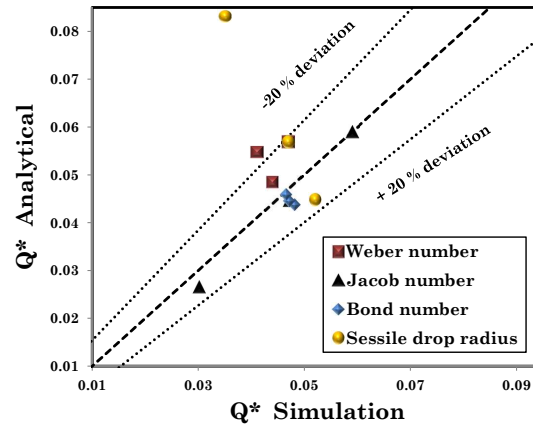


Fig. 3.38: Non-dimensional input heat: Analytical versus Simulation

3.7 Closure

This chapter deals with the numerical modelling of drop-on-drop impingement over a heated wetting surface. The preliminary cycle of drop-on-drop impingement is examined and classified into three phases i.e., coalescing, advancing and receding regimes. To understand the basic phenomena associated with the process, it is compared with the single droplet impact and extended to study the effect of influencing parameters on spread and evaporation dynamics of the process. The next chapter reports the experimental investigation of two consecutively impinging droplets over a heated surface.

CHAPTER 4

EXPERIMENTAL STUDY: DROPLET IMPACT OVER A HEATED SURFACE IN AIR-VAPOUR MEDIUM

4.1 Introduction

The present work is aimed at studying the spread and heat transfer dynamics of a consecutive impingement train of two droplets over a heated surface in a air-vapour medium (open atmospheric conditions). High-speed photography and infrared thermographic techniques are employed to capture the post impingement events associated with the process. A thin Inconel 600 foil has been used as the target surface and temperature is chosen as the parameter. Preliminary experiments are carried out using Deionised water and the surface temperature is varied from ambient temperature of 22 °C to 175 °C, and found to be within the film evaporation regime. It is followed by FC-72 droplet impingement over the surface and chosen the temperatures upto Dynamic Leidenfrost Point which is about 105 °C in the present study. From the instant of impact, the droplets are found to undertake a series of spreading and receding phases until it achieves an equilibrium and evaporates as a spherical liquid cap (Liang and Mudawar, 2017). In the present work, the impact dynamics of droplet initial stage i.e., spreading and receding phases are captured and studied in detail. The event of consecutive impact is considered as two separate configurations i.e., single droplet and drop-on-drop impact. The temporal variation of droplet deformation in terms of spread diameter, dynamic contact angle and heat transfer rate are used and compared for these configurations.

4.2 Experimental methodology

Experimental apparatus consists of image acquisition system, droplet generating unit and heater surface arrangement powered by a high capacity DC supply. The schematic of experimental set up is shown in Figure 4.1. A microfluidic pressure pump (Dolomite, MitoS P-pump) connected to an external air compressor, is used to generate the desired rate of droplets at the needle tip and are made to fall under gravity to achieve the required impact conditions. A trial set of 30 droplets is considered for diameter calculation and the generated droplet size for Deionised water and FC-72 are found to be 2.80 ± 0.04 mm and 1.2 ± 0.06 mm respectively.

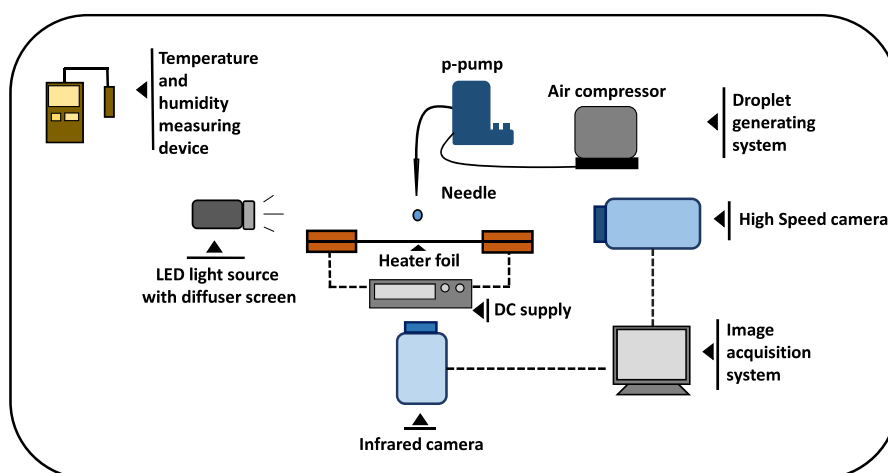


Fig. 4.1: Schematic showing the experimental apparatus used in the present study

Image acquisition system consists of a high-speed camera (*Photron fastcam SA3 120K*) running at 10000 FPS (frames per second) with a spatial resolution of $20 \mu\text{m}/\text{pixel}$. Shadow photography technique is adopted for imaging the droplets using a LED light source with a diffusion screen. Factory calibrated high-performance infrared camera (*FLIR X6540sc*) is used to capture the thermal foot print (temperature distribution) of the droplet on the surface. With a frame rate of 1000 FPS and a spatial resolution of $136 \mu\text{m}/\text{pixel}$, the infrared camera is triggered simultaneously along with high-speed camera. The post-processing of images is carried out using *Matlab* Image processing tool box and an open source java based image processing program, *ImageJ* (Schneider *et al.*, 2012).

An annealed Inconel 600 alloy foil of thickness $25 \mu\text{m}$ is used as the target surface,

sandwiched between copper bus bars on either side, and fixed to a wooden base. The surface is polished, and the surface roughness measurement, R_a , using stylus probe profilometer is within the range of 0.15 - 0.30 μm . DC power supply (*BK Precision 1900, 1-16 VDC, 60 A*) is provided through the copper bus bars to maintain the surface at different temperatures using power supply controls. To improve the response of the infrared camera imaging of the surface, a thin layer of high heat-resistant black paint is applied underneath the surface. The emissivity of the paint was measured using an emissometer (*D & S Emissometer, Model AE*) and found to be 0.82. The dimensions of the foil surface is about 45 mm x 40 mm x 0.025 mm.

4.2.1 Impingement configuration

A train of two droplets are consecutively impacted on to the foil surface. The event is captured through the high-speed camera from the side view while the temperature variation of the surface, upon interaction with the droplet, is acquired from the bottom of the surface using the thermal camera. The impingement scenarios are presented in Figure 4.2 where both the schematic diagram and high speed images are provided.

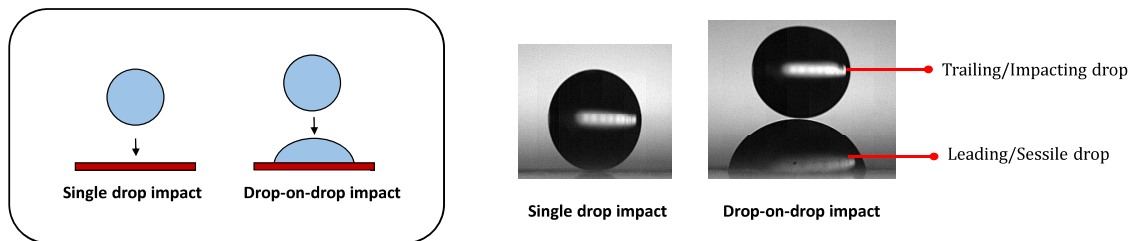


Fig. 4.2: Impingement configurations considered in the present work

The time interval between the two drops (t) is approximately 3 seconds and 1 second for water and FC-72 i.e., the flow rate is about 20 and 60 droplets per minute (DPM) respectively. With this flow rate, the leading droplet that impinges the foil surface will become sessile, before the trailing droplet impacts on the sessile droplet. Thus the configuration can be treated as a drop-on-drop impact. Figure 4.3 is a schematic that demonstrates the temporal change of droplet spread diameter upon impact with the surface. The first droplet, when impacted, oscillates on the surface for a while, and will remain sessile upon which the second droplet is impinged resulting in the spreading and receding phases.

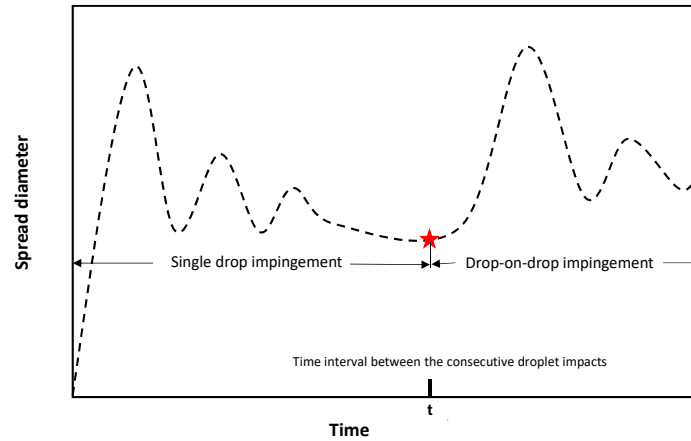


Fig. 4.3: Schematic showing the temporal change of spread diameter during the impact

4.2.2 Image post-processing

Information regarding hydrodynamics such as droplet initial diameter (volume), spread diameter, and dynamic contact angle are measured using the side-view images of the impingement process. Standard procedures of image conversion i.e., conversion of grey to binary image followed by edge and region recognition, are implemented, and data is retrieved using resources available in *Matlab* and *ImageJ* post-processing toolbox. The resulting image after post-processing is shown in Figure 4.4.

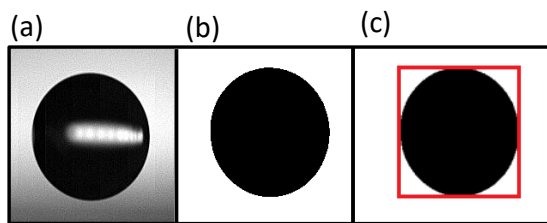


Fig. 4.4: Steps involved in image post-processing: (a) Grayscale (b) Binary (c) Region recognition

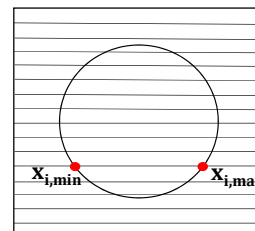


Fig. 4.5: Droplet volume calculation

Droplet volume (diameter) calculation

High-speed images obtained from experiments are used for the calculation of droplet volume and diameter. Assuming an axisymmetric droplet, the volume of the droplet is calculated (Schweizer, 2010) by summing up the cylindrical slices of unit pixel height

as

$$Volume, V = \frac{\pi}{4} Z_p^3 \sum d_i^2 \quad (4.1)$$

where, d_i , the diameter of each cylindrical strip in the droplet image given as $(x_{i,max} - x_{i,min})$ as shown in Figure 4.5, and Z_p is the resolution of the image measured in *meter/pixels*

Then diameter of the droplet can be obtained as

$$Diameter, D_0 = \left[\frac{6V}{\pi} \right]^{1/3} \quad (4.2)$$

Dynamic contact angle

The wetting characteristics of a surface for an impinging liquid can be represented using the contact angle in the three-phase contact region. Former studies on droplet-wall interactions (Herbert *et al.*, 2013b; Šikalo *et al.*, 2005; Chandra and Avedisian, 1991) discussed various contact angles and the effect of contact line velocity and temperature on contact angle. Measurement of this dynamically changing angle will enhance the understanding of the key aspects associated with the spread and evaporation dynamics of the present work.

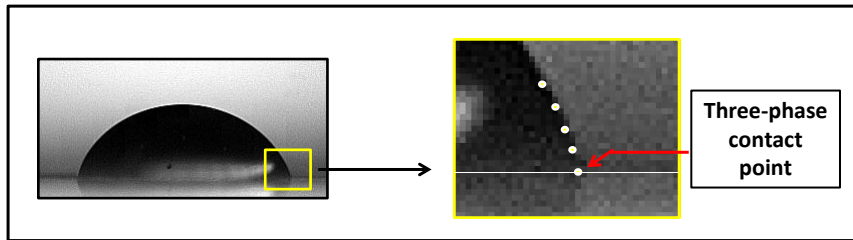


Fig. 4.6: Contact angle measurement

In the present work, the three-phase contact angle is calculated using the side-view images of droplet impingement. During the impact process, the observed profiles of the droplet are complex, and standard methods of curve fitting for obtaining the droplet profile is mathematically tedious and complicated. Instead, as shown in Figure 4.6, at least five points on the droplet profile near the contact line region are considered. Upon analysis, a second-order polynomial fits well with the selected data points, and the tangent of the polynomial at the three-phase contact point is calculated as the dynamic

contact angle.

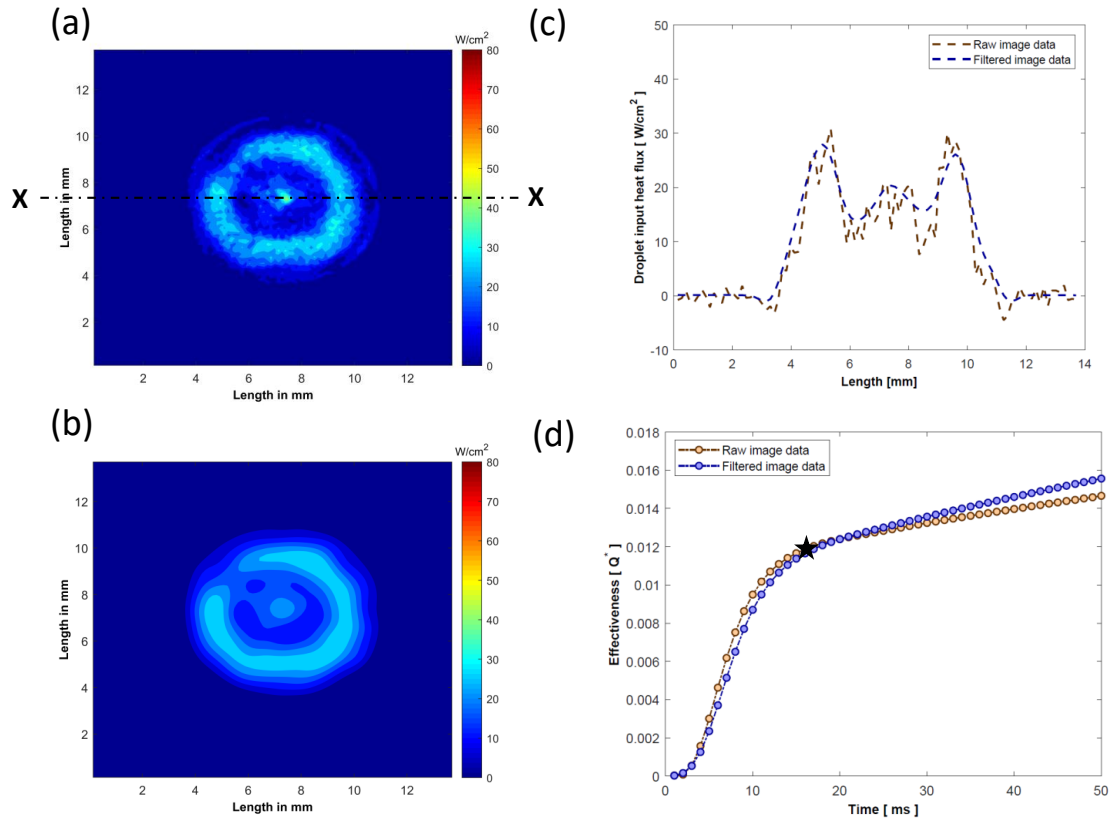


Fig. 4.7: (a) Raw image ($T = 154\text{ }^{\circ}\text{C}$ and $t = 15\text{ ms}$) (b) Filtered image (c) Droplet input heat flux distribution along the centreline X-X (d) Effectiveness

4.2.3 Infrared image post-processing

The infrared camera used in the present study is factory calibrated, and the uncertainty associated with temperature measurement is $\pm 1\text{ K}$. It is noticed that the recorded raw images are prone to noise, and is estimated in terms of the noise equivalent temperature difference (NETD) value of thermography system. For the given temperature range used in the study, the NETD values are within the acceptable range of 60 - 200 mK. However, it is shown that the heat conduction term used in the heat transfer analysis is sensitive to the spatial signal noise of the input temperature field (Schweizer, 2010) and extensive filtering is required to reduce the noise. Time and spatial averaging are applied to the temperature field, and it is followed by the application of *Matlab* provided Gaussian filter ($\sigma_{sd} = 2$). The detailed description of the method can be found in reference Schweizer (2010). Figure 4.7(a) and (b) shows the raw and filtered heat flux image calculated during single droplet impact over a

surface temperature of 154 °C, and at a time instant, $t = 15$ ms. From Figure 4.7(c), it is visible that the non-physical noise in heat flux distribution is reduced, and the overall droplet heat transfer during the impact, expressed as effectiveness (Q^*), is not significantly affected by the filtering procedure, as given in Figure 4.7(d).

Droplet input heat transfer calculation

The droplet input heat transfer is one of the important parameters required for understanding the droplet-hot wall interactions and the ongoing cooling process. The temperature variation of the surface is obtained from the bottom of the surface via infrared images. An energy balance is applied at every pixel element of the surface, as shown in Figure 4.8 to calculate the heat transfer into the droplet.

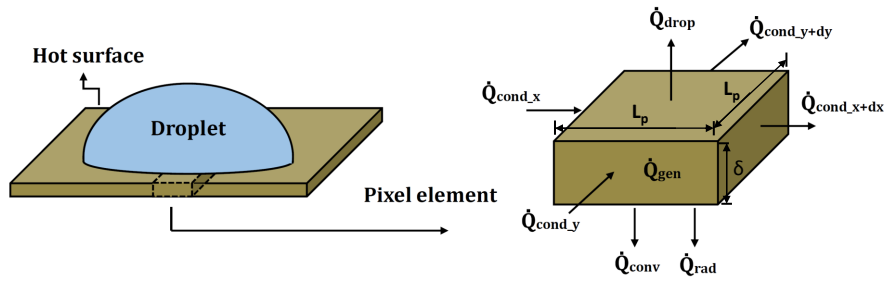


Fig. 4.8: Heat transfer calculation: energy balance at a pixel element

The energy balance applied to the pixel element results in

$$Q_{stored} = Q_{gen} + Q_{cond} - Q_{rad} - Q_{conv} - Q_{drop} \quad (4.3)$$

where droplet input heat transfer is represented as Q_{drop}

Thus,

$$Q_{drop} = Q_{gen} + Q_{cond} - Q_{rad} - Q_{conv} - Q_{stored} \quad (4.4)$$

and droplet input heat flux q_{drop} is obtained, using the length of the pixel element L_p , as

$$q_{drop} = \frac{Q_{drop}}{L_p^2} \quad (4.5)$$

It is noted that Q_{stored} represents the change in energy of the surface due to cooling,

and Q_{gen} being heat generated due to DC supply. While Q_{cond} , Q_{rad} and Q_{conv} are net conduction heat transfer along the surface, radiation and convection heat transfers underneath the surface respectively.

A continuous DC supply is provided to the surface and is maintained at a constant temperature. Upon droplet impingement, considerable heat transfer takes place resulting in the cooling of the surface. The generated heat due to the DC supply is calculated as Q_{gen}

$$Q_{gen} = \frac{I^2 R V_p}{V_s} \quad (4.6)$$

where I being the supplied current, V_p and V_s are the volumes of considered pixel element and total surface respectively.

Following the reference Schweizer (2010), the heater foil resistance 'R' is obtained from

$$R = \frac{\rho_s L_p (1 + \alpha_s (T - T_\infty))}{A_p} \quad (4.7)$$

where ρ_s , L_p , $A_p (= L_p \delta)$, α_s and δ represents surface electrical resistivity, pixel length, cross-sectional area, temperature coefficient of resistance, and thickness of the pixel element respectively. The properties of the surface is outlined in Table 4.1.

The net energy change in the pixel, is termed as stored heat Q_{stored}

$$Q_{stored} = \frac{m_s c (T_t - T_{t-1})}{dt} \quad (4.8)$$

where m_s is the mass of the pixel element, c specific heat capacity, T_t and T_{t-1} are the temperatures of the pixel element at a time intervals of t and $t - 1$ respectively.

Due to negligible thickness (Schweizer, 2010; E.Teodori *et al.*, 2018), the conduction effects perpendicular to the heater surface is minimal compared to other directions.

Thus, the conduction heat transfer along the surface is taken into account and is given as

$$Q_{cond} = (Q_{cond})_{in} - (Q_{cond})_{out} \quad (4.9)$$

can be simplified into

$$Q_{cond} = \frac{k_s A_p (T_{i+1,j} + T_{i-1,j} + T_{i,j+1} + T_{i,j-1} - 4T_{i,j})}{L_p} \quad (4.10)$$

where k_s is surface thermal conductivity and $T_{i,j}$ represents the temperature of considered element, and $T_{i+1,j}$, $T_{i-1,j}$, $T_{i,j+1}$, $T_{i,j-1}$ are the temperatures of neighbouring pixel elements in respective directions.

The bottom side of heater surface is coated black and is maintained at high temperatures. The radiation heat transfer underneath the surface is considered as

$$Q_{rad} = \sigma \epsilon_r L_p^2 (T_{i,j}^4 - T_\infty^4) \quad (4.11)$$

Also, natural convection currents will form eventually underneath the hot surface which can be calculated as

$$Q_{conv} = h_i L_p^2 (T_{i,j} - T_\infty) \quad (4.12)$$

where natural convective heat transfer coefficient at a pixel element, h_i can be taken from the correlation

$$h_i = 0.27 Ra_i^{0.25} \quad (4.13)$$

and Ra_i is the Rayleigh number and all the properties are considered at the film temperature T_f

$$T_f = \frac{T_{i,j} + T_\infty}{2} \quad (4.14)$$

Using the above energy balance, the contributions of heat transfer quantities towards the droplet input heat transfer is compared. Two instants, one each in the spreading and receding phase, are selected and the percentage of heat transfer quantities is calculated against the magnitude of droplet input heat transfer at the impact point (pixel). Figure 4.9 shows the selected points which are marked over the temporal change of spread factor for the droplet impingement over the surface at a temperature of 154 °C. Figures 4.10 and 4.11 present the comparison of these quantities during the advancing and receding phases as a percentage of the droplet heat transfer. It is evident that Q_{gen} and Q_{cond} are significant quantities compared to Q_{rad}

and Q_{conv} in contributing to the droplet input heat transfer.

Even though the heat loss by convection and radiation seems negligible in receding phase, it is important for the accurate estimation of droplet heat transfer in the spreading phase. Thus, in the present work, all the above described heat transfer quantities will be included for droplet heat transfer calculations.

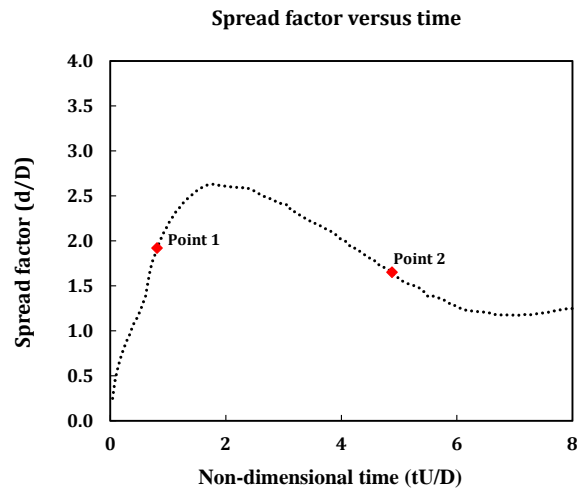


Fig. 4.9: Single droplet impact over the target surface ($T = 154^{\circ}\text{C}$)

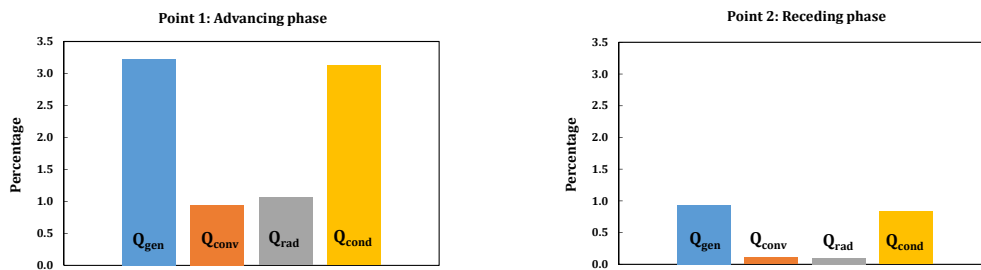


Fig. 4.10: Comparison in advancing phase Fig. 4.11: Comparison in receding phase

4.2.4 Experimental methodology: Validation cases

The present experimental methodology is validated using previously published studies available in the literature. Two cases: drop-on-drop impingement over a non-heated surface, and a single droplet impact over a heated surface are carried out. The spreading parameter i.e., spread factor is calculated and compared with experimental results.

Drop-on-drop impact over non-heated surface

For the present study, the generation of multiple droplets to achieve the drop-on-drop configuration is crucial. Wakefield *et al.* (2016) carried out drop-on-drop impingement studies over a non-heated Teflon surface with the Weber number as a parameter. A case with Weber number of 2 is considered for the validation, and the results are compared in terms of the spread factor. Figure 4.12 shows the results from the present experiments compared with Wakefield *et al.* (2016). The variation of spread factor with time was found to be in agreement within $\pm 10\%$, thus validating the experimental methodology followed in the present work.

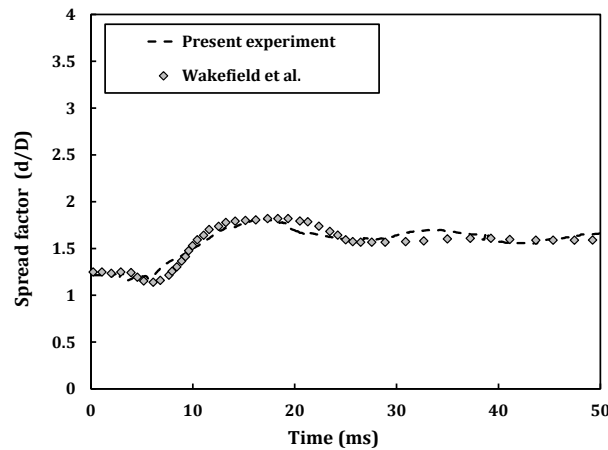


Fig. 4.12: Drop-on-drop impact over a non-heated surface

Single droplet impact over a heated surface

Pasandideh-Fard *et al.* (2001) studied the cooling effectiveness of a single droplet over a heated surface. A single water droplet is impacted over a stainless steel surface maintained at a constant temperature of 120 °C with an impact Weber number of 47. In the present set up, a thin Inconel surface is used instead of stainless steel, and maintained at 120 °C. Figure 4.13 shows the temporal variation of spread factor during the impingement. To validate the accurate variation of spread dynamics over a heated wall, the surface temperature and impact conditions should be exactly maintained. However, in spite of the differences in the target surface (Inconel versus Stainless steel), the results shown in Figure 4.13 show similar trends confirming the validity of the present experimental set-up for droplet impingement studies over heated target surfaces.

Table 4.1: Thermo-physical properties of Inconel 600 alloy used in the present study.

Properties	Value
Density, ρ , kg/m^3	8470
Thermal conductivity, k_s , W/mK	14.8
Electrical resistivity, ρ_s , Ohm-m	$103 \cdot 10^{-8}$
Specific heat capacity, c , kJ/kgK	444
Temperature coefficient of resistance, α_s , K^{-1}	$12 \cdot 10^{-5}$

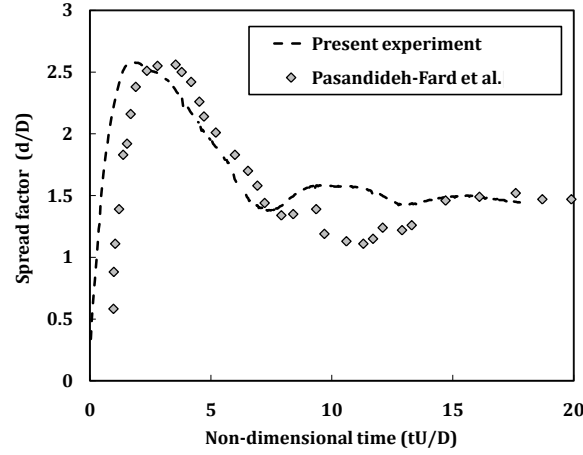


Fig. 4.13: Single droplet impact over a heated surface ($T = 120 \text{ }^\circ\text{C}$)

4.3 Water droplet impingement

During the present investigation, a train of two water droplets of diameter 2.8 mm is impacted, with a velocity of 1.138 m/s , onto a thin Inconel surface maintained at a constant temperature. The surface is hydrophilic, and contact angle measurements are made using *Holmarc's contact angle meter*. The static contact angle, quasi-static advancing and receding angles over the non-heated surface are $72 \pm 1 \text{ }^\circ$, $83 \pm 4 \text{ }^\circ$ and $13 \pm 1 \text{ }^\circ$ respectively. The thermo-physical properties of the deionized water and Inconel surface are listed in Table 4.2 and Table 4.1 respectively. The impact conditions corresponds to a Weber number of 50 and Reynolds number of 3180 with a constant flow rate of 20 droplets per minute (DPM). The surface temperature is the parameter and varies from 22 $^\circ\text{C}$ (non-heated) to 175 $^\circ\text{C}$. At every temperature, the images of single drop and drop-on-drop impacts are recorded separately and analysis is carried out. Droplet impingement experiments were carried out at an ambient temperature of 22 $^\circ\text{C}$ and a relative humidity of about 50 %.

Here the focus is to analyse the spread and heat transfer characteristics at the instant

Table 4.2: Thermo-physical properties of Deionized water used in the present study, at 1 atm and ambient temperature of 22 ° C.

Properties	Value
Saturation temperature, T_{sat} , ° C	100
Density, ρ_l , kg/m^3	998
Dynamic viscosity, μ , Ns/m^2	0.001
Surface tension, σ , N/m	0.0725
Specific heat capacity, c_p , kJ/kgK	4.18
Latent heat of vaporization, h_{lv} , kJ/kg	2260

Table 4.3: The experimental uncertainties associated with different parameters used in the study.

Parameter	Uncertainty
Temperature	$\Delta X = \pm 1 \text{ K}$
Generated volumetric heat flux $q''_{gen} = Q_{gen}/V_s$	$\Delta x_{max} = 11 \%$ ($q''_{gen} = 20 \cdot 10^6 \text{ W}/m^3$ at $T = 50 \text{ ° C}$)
Weber number, We	$\Delta X = \pm 2$ ($We = 50$)
Reynolds number, Re	$\Delta X = \pm 90$ ($Re = 3180$)
Droplet diameter, D_0	$\Delta X = \pm 0.04 \text{ mm}$ ($D_0 = 2.8 \text{ mm}$)
Droplet impact velocity, U_0	$\Delta X = \pm 0.0171 \text{ m/s}$ ($U_0 = 1.138 \text{ m/s}$)
Dynamic contact angle, θ	$\Delta x_{max} = 36 \%$ ($\theta = 62^\circ$ at $T = 175 \text{ ° C}$, Single droplet impact) $\Delta x_{min} = 1.2 \%$ ($\theta = 81^\circ$ at $T = 175 \text{ ° C}$, Drop-on-drop impact)
Spread factor, S^*	$\Delta x_{max} = 12 \%$ ($S^* = 0.43^\circ$ at $T = 175 \text{ ° C}$, Single droplet impact) $\Delta x_{min} = 2 \%$ ($S^* = 2.63$ at $T = 175 \text{ ° C}$, Single droplet impact)

of impact where effective cooling of the surface will take place. The time scale of impingement is of order; time $t = 45$ milliseconds corresponds to a non-dimensional time, $\tau = 18$ for each configuration. The spread dynamics is photographed using a high-speed camera, and the temperature response during the impact is recorded from the underside of the surface using infrared thermography.

At each chosen temperature, three sets of data is recorded ($n = 3$), and average values are used to represent the data. The experimental uncertainties associated with different parameters are presented in the Table 4.3. Here ΔX and Δx are used to represent the absolute and relative uncertainties respectively.

4.3.1 Results and Discussion

When the droplet comes in contact with a hot surface, heat transfer takes place which results in the cooling of the surface. The temperature of the droplet increases with time; evaporation ensuing across the liquid-gas interface affects the droplet spread diameter.

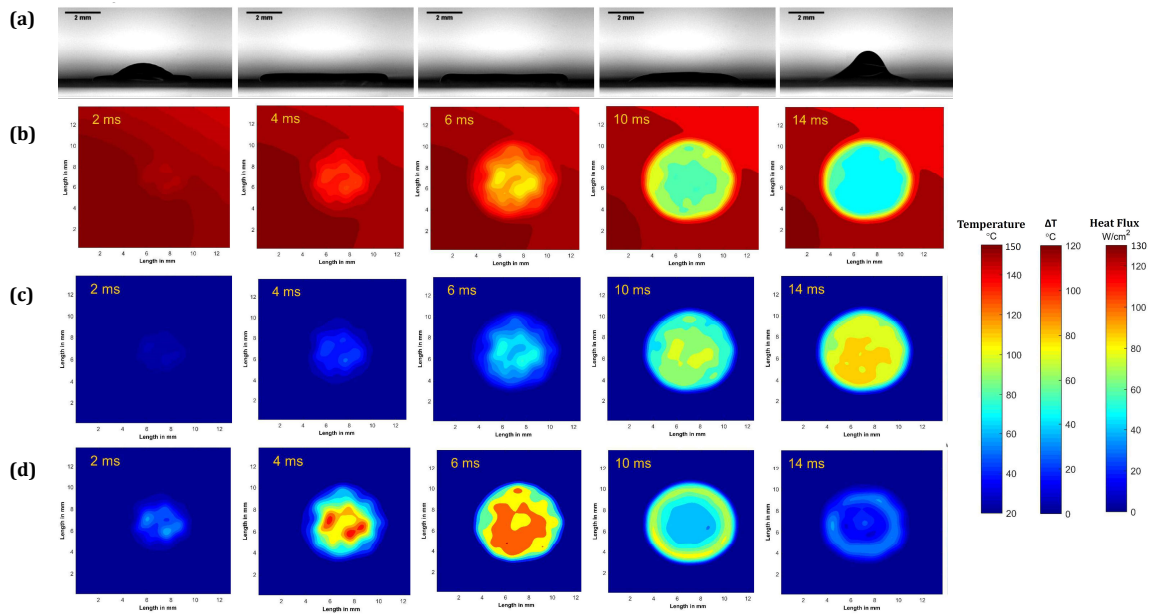


Fig. 4.14: Single droplet impingement over the foil surface ($T = 154\text{ }^{\circ}\text{C}$) : (a) Side-view image (b) Foil surface temperature after impingement (c) Change in temperature (d) Heat flux distribution

Thus, it is important to study the effect of surface temperature on both the spread and the heat transfer characteristics. Figures 4.14 and 4.15 show the spread behaviour of single and drop-on-drop configurations, respectively over the surface with a pre-impact surface temperature of $154\text{ }^{\circ}\text{C}$. The present arrangement of hot surface, using Joule heating, resulted in slightly non-uniform pre-impact surface temperature. Here, the spatial mean temperature (maximum deviation of $\pm 3\text{ }^{\circ}\text{C}$ is observed at $T = 154\text{ }^{\circ}\text{C}$) is represented as the surface temperature. Also, to realise the temperature contours during drop-on-drop impact, the change in temperature (ΔT) for each pixel, is calculated as the difference of the initial temperature to the instantaneous temperature. The temperature contours, the corresponding change in temperature (ΔT), and droplet input heat flux (q_{drop}) are also presented. A considerable amount of heat transfer, termed as effective heat transfer, is observed to occur during the initial stage of droplet interaction with the surface in both the configurations. From Figures 4.14 (d) and 4.15 (d), it can be noted that the significant heat transfer is during the initial spreading phase whereas the peak value is detected at the maximum spread of the droplet. However the heat transfer associated with single droplet impact is prominent compared to that of drop-on-drop configuration. This is because of the low pre-impacting surface temperatures for drop-on-drop scenario as given in 4.15 (b), due to the presence of the initial droplet on the target surface, thereby resulting in lower heat transfer rates. The subsequent sections of

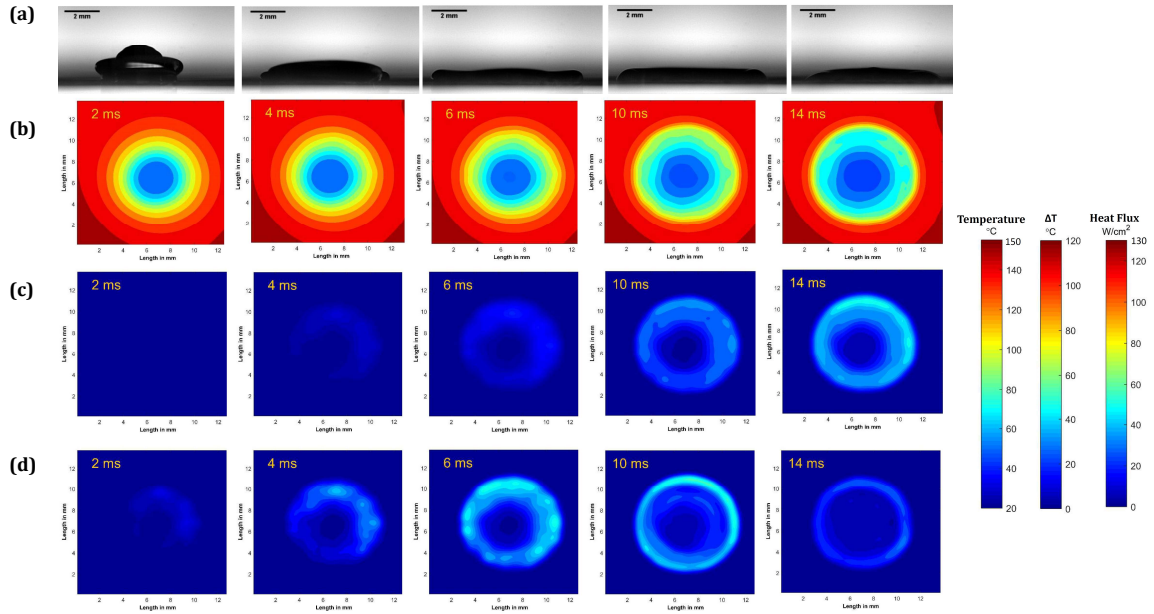


Fig. 4.15: Drop-on-drop impingement over the foil surface ($T = 154 \text{ }^{\circ}\text{C}$) : (a) Side-view image (b) Foil surface temperature after impingement (c) Change in temperature (d) Heat flux distribution

this paper describe the spread hydrodynamics in terms of the spread factor and surface wetting i.e., contact angle. Detailed description of heat transfer characteristics are also provided.

Spread hydrodynamics

Upon impact, the leading droplet performs a series of advancing and receding phases by dissipating the impact energy and attains a sessile droplet state. Consecutively, the second droplet, which impinges on to the sessile droplet, will coalesce for specific instant followed by the spreading and receding phases. Thus, for a single droplet impact, the initial cycle consists of two phases; advancing and receding. Whereas, in a drop-on-drop impingement, three stages, namely; coalescing, advancing and receding, are identified during the initial cycle. A non-dimensional quantity called spread factor, S^* , is defined as the ratio of spread diameter at an instant (d) to the pre-impact droplet diameter (D_0). The temporal variation of spread factor during single droplet and drop-on-drop impact, with identified phases at various surface temperatures, is plotted, as shown in Figure 4.16. For both the configurations, the temperature effect on the spread is evident from the first cycle of spreading. Also, there is a notable reduction in spread factor with temperature in subsequent cycles for both the single droplet as well

as drop-on-drop impingement configuration. The comparison of spread factor during

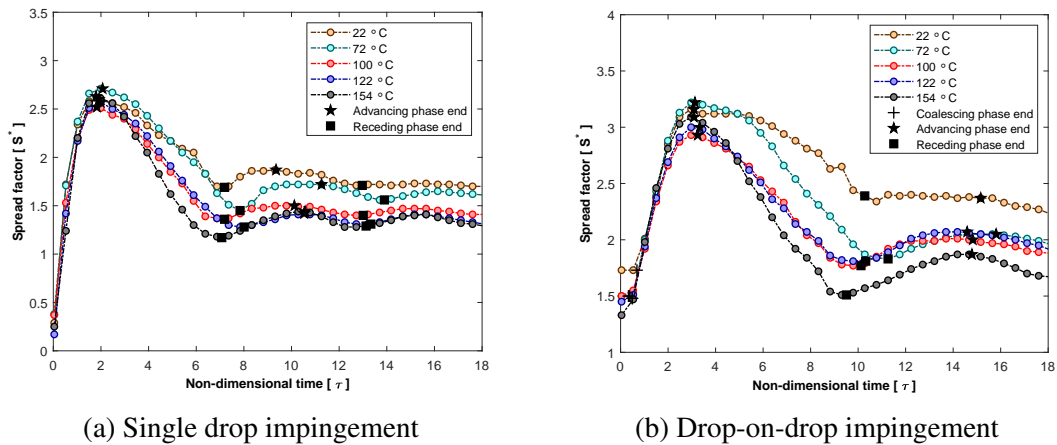


Fig. 4.16: Spread factor versus time

single droplet and drop-on-drop impact at a surface temperature of 154 °C is obtained to understand the effect of configuration on hydrodynamics, as shown in Figure 4.17. Due to the interference of droplets during the impact, the cycle of spreading and receding is delayed, for drop-on-drop impingement, which resulted in longer initial cycle time. The cycle time of single droplet impact is about $t = 18$ ms ($\tau \sim 7.5$) and drop-on-drop impingement is about $t = 24$ ms ($\tau \sim 9.5$) where coalescing phase is about $t = 1$ ms ($\tau \sim 0.5$). The presence of two droplets resulted in a higher spread factor for the drop-on-drop configuration. However, the *net spread factor* (δS^*) at a given instant of time, which is defined as the ratio of change in spread diameter ($d - D_s$) to the impacting droplet diameter (D_0), is more for the single droplet case. The *net spread factor* has reduced during the drop-on-drop impingement due to the high energy dissipation resulted from the droplet coalescence.

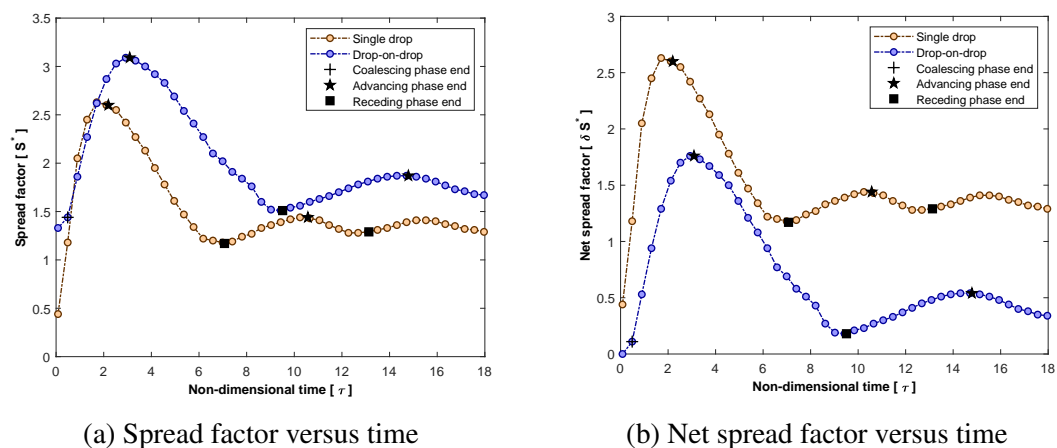


Fig. 4.17: Comparison of single droplet and drop-on-drop impact over the surface ($T = 154$ °C)

Observations revealed that the dynamics of spread is coupled with droplet heat transfer. Especially, the maximum spread factor will dictate the extent of heat transfer over the surface. So, in order to analyse heat transfer rate, the maximum spread factor for the initial and second cycle of the post-impingement is considered. It is noted that, in the present context, a cycle refers to a sequence of spreading and receding phases. Figures 4.18 (a) and 4.18 (b) shows the comparison of maximum spread factor during the first and second cycles which convey that the initial cycle's maximum spread factor has a weak dependence on the surface temperature, whereas it decreases with temperature during the second cycle and the effect is significant for both configurations during the second cycle.

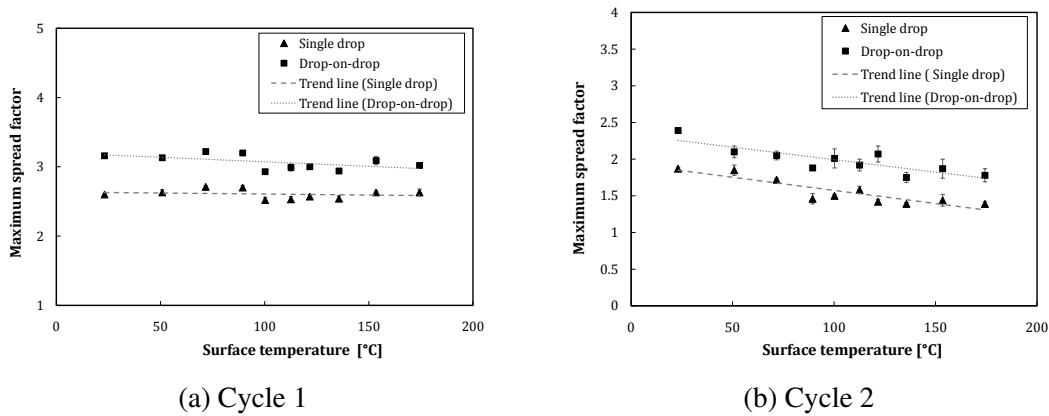


Fig. 4.18: Maximum spread factor with surface temperature: Single drop and drop-on-drop impact

Likewise, another important parameter related to hydrodynamics is the contact angle and its variation during both impingement configurations. The three-phase contact angle is known to vary with velocity (Šikalo *et al.*, 2005) and increase with the surface temperature (Herbert *et al.*, 2013b; Chandra and Avedisian, 1991). It will affect the spread of the droplet, and therefore, the heat transfer rate. The variation of the dynamic contact angle with time is obtained for the present configurations to ascertain the effect of temperature, as shown in Figure 4.19. As soon as the droplet impacts the surface, a high contact angle is observed as it is under the influence of impacting velocity, and the value declines during the receding phase (Šikalo *et al.*, 2005). In the present study, the captured contact angle variation exhibits a similar behaviour during both impingement configurations, as shown in Figures 4.19(a) and (b).

For a single droplet impact, the contact angle is increased till it reaches the maximum spread (advancing phase end) and decreases to a minimum angle at the end of receding phase which is given in Figure 4.19(a). Meanwhile, for drop-on-drop impingement, as presented in 4.19(b), the trend is similar to single droplet impact, additionally exhibits a constant angle during the coalescing stage. In the present study, the effect of temperature on dynamic contact angle is found to be weak. During the single droplet impingement, a slight increase in dynamic contact angle is observed for the heated case ($T = 175\text{ }^{\circ}\text{C}$) compared to non-heated case ($T = 22\text{ }^{\circ}\text{C}$) in subsequent stages of spreading as shown in Figure 4.19(a). However, the increase is marginal and within the uncertainty of the presented data. Additionally, sessile droplet contact angle (Static contact angle) variation with surface temperature is inspected and given in Figure 4.20, and for the temperatures used in the present work, there is only a minor increase in contact angle with surface temperature. Previous studies (Herbert *et al.*, 2013*b*; Chandra and Avedisian, 1991) reported a strong effect of temperature on contact angle which is not so evident in the present work. The difference in volatility of the liquid, and surface conditions are attributed to this behaviour.

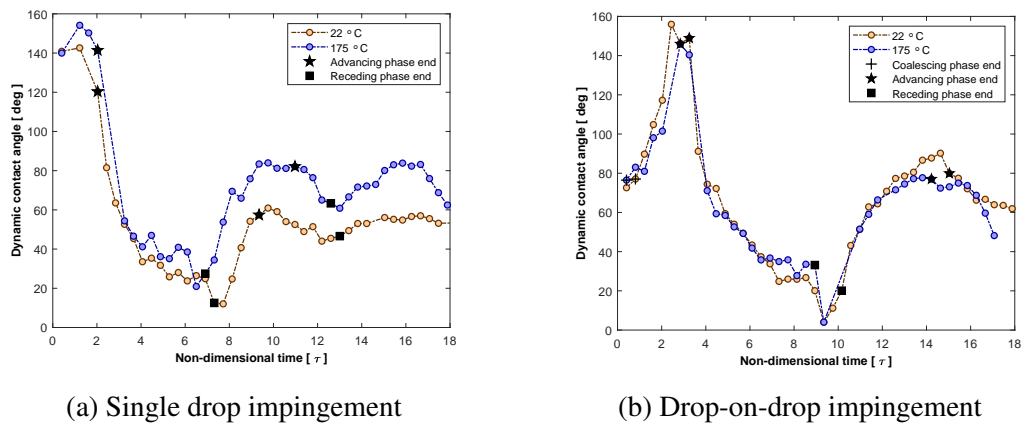


Fig. 4.19: Dynamic contact angle versus time

Heat transfer characteristics

Furthermore, to understand the heat transfer into the droplet, an average quantity of heat transfer is calculated over an effective area in which a significant amount of heat transfer takes place. The effective area is identified using Canny edge detection technique, implemented in *Matlab* image post-processing toolbox, applied to a heat flux image (Jung *et al.*, 2016) as shown in Figure 4.21. A dimensionless effective area

A_e^* is used to compare the present impingement configurations. This is calculated as the ratio of the surface area with effective heat transfer to the cross-sectional area of the impacting droplet.

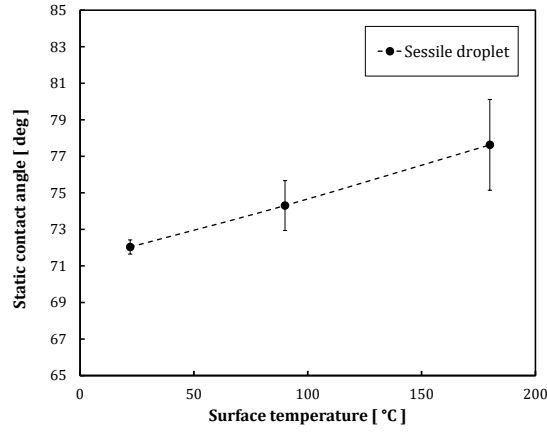


Fig. 4.20: Static contact angle versus temperature

$$A_e^* = \frac{4A_e}{\pi D_0^2} \quad (4.15)$$

where A_e is the area where effective heat transfer is observed. In the present work, dimensionless effective area A_e^* provides a quantitative measurement of area being cooled during the impingement and it can also be observed that the maximum spread factor S_{max}^* during the impact can be approximated from the effective area as

$$S_{max}^* \sim ((A_e^*)_{max})^{0.5} \quad (4.16)$$

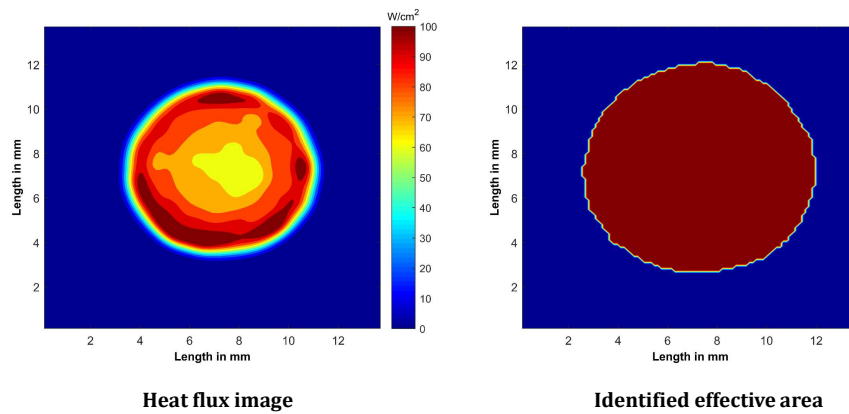


Fig. 4.21: Effective area recognition to calculate the average surface heat transfer rate

Figure 4.22 shows that the droplet heat transfer is enhanced with an increase in the

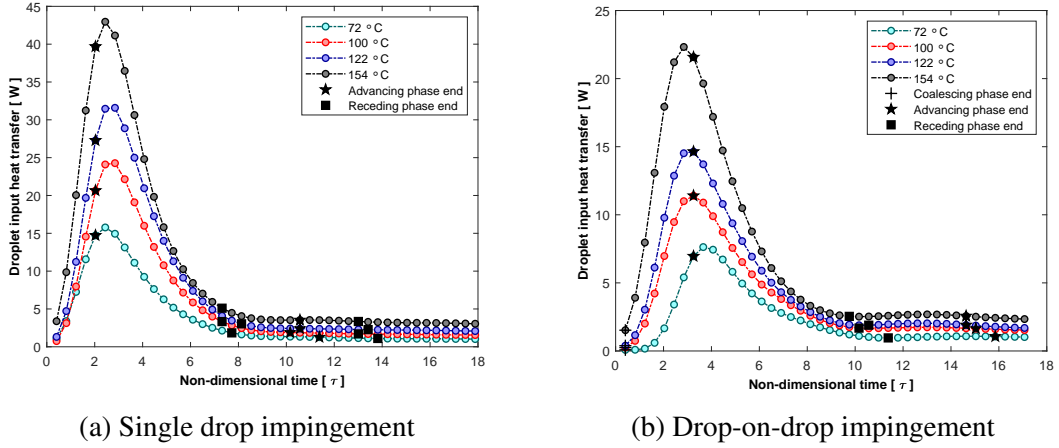


Fig. 4.22: Droplet input heat transfer versus time

surface temperature and this trend is similar for both single and drop-on-drop configurations. A maximum in droplet heat transfer rate is realised at the end of the first advancing phase for all surface temperatures and confirms that most of the surface cooling is takes place during the initial cycle of the droplet impact. A dimensionless input heat transfer, termed as effectiveness or cooling efficiency (Q^*), is introduced to estimate the overall heat transfer per droplet. It is defined as the ratio of the time integral of droplet input heat transfer to the total heat required for the droplet evaporation.

$$Q^* = \frac{\int_0^t (Q_{drop}) dt}{m(c_p(T_{sat} - T_\infty) + h_{lv})} \quad (4.17)$$

Figure 4.23 shows the variation of effectiveness (Q^*) with time for both single and drop-on-drop impingement at different temperatures.

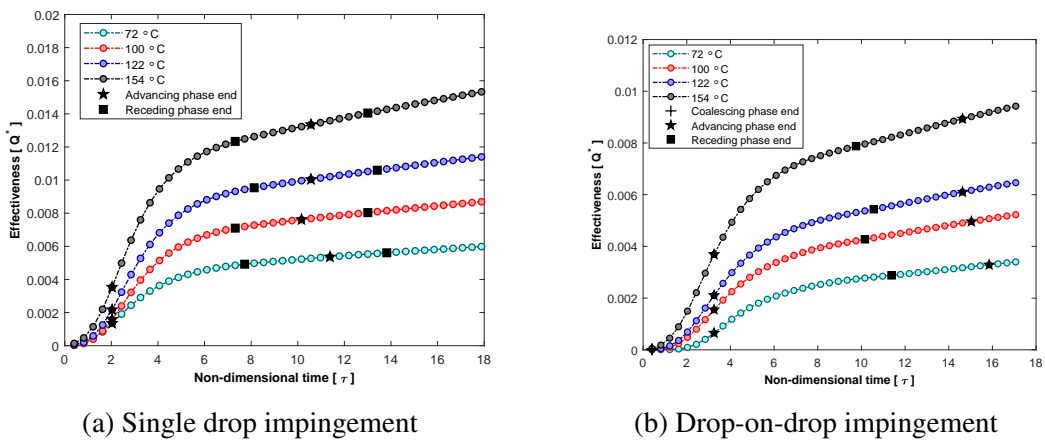
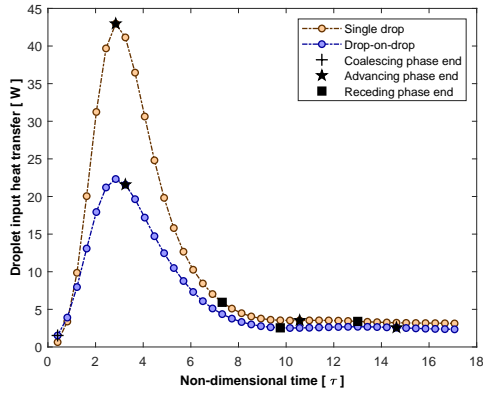
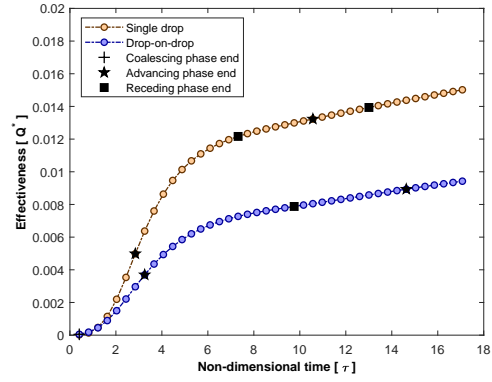


Fig. 4.23: Effectiveness versus time

A comparison of both the configurations at a given surface temperature, as shown in Figure 4.24, reveals that the droplet input heat transfer is lower for the drop-on-drop



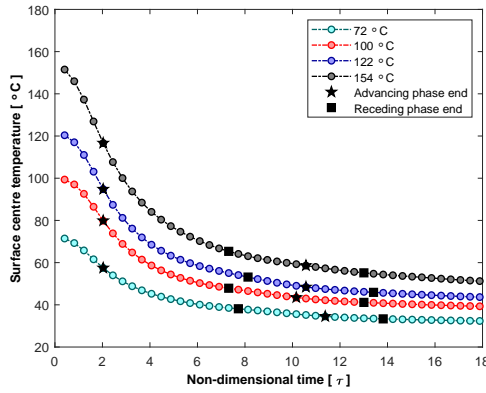
(a) Droplet input heat transfer versus time



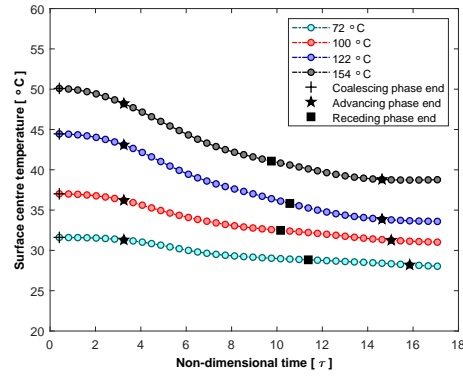
(b) Effectiveness versus time

Fig. 4.24: Comparison of single and drop-on-drop impact over the target surface ($T = 154\text{ }^{\circ}\text{C}$)

impact compared to single droplet case. This is because of the reduction in surface mean temperature as a result of initial droplet (sessile) interaction with the surface. Also, the previous work using numerical modelling (see Chapter 3) revealed that there is rapid decline in heat transfer rate due to the increased film thickness during the drop-on-drop impingement.



(a) Single drop impingement



(b) Drop-on-drop impingement

Fig. 4.25: Target surface center temperature versus time

In order to interpret the surface cooling during the impingement, the surface temperature change with time is determined. The surface temperature change upon impact is plotted by tracking the temperature of the impact point, and termed as centre temperature as shown in Figure 4.25. The impact point is always the lowest temperature over the surface during the impingement Pasandideh-Fard *et al.* (2001). The change in surface temperature is rapid for the case of single droplet impingement compared to drop-on-drop impact, and follows a similar trend for all surface temperature cases considered in the study. However, it is observed that the effective

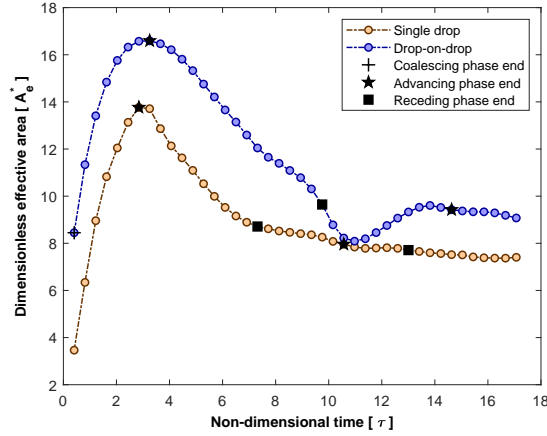


Fig. 4.26: Comparison of effective area for the target surface ($T = 154 \text{ }^\circ\text{C}$)

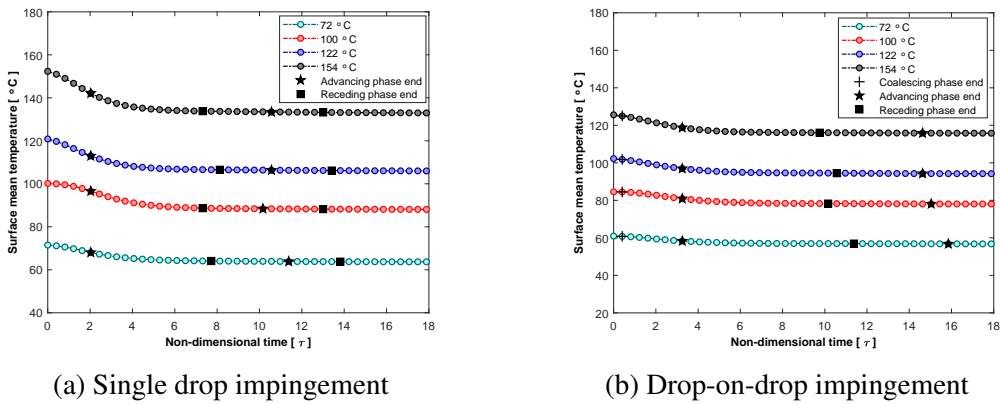
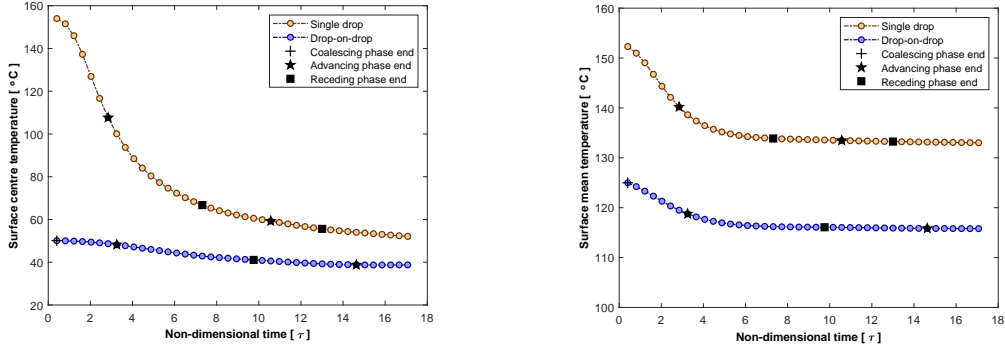


Fig. 4.27: Surface mean temperature versus time

area where considerable heat transfer occur, is improved during the drop-on-drop impingement as shown in Figure 4.26.

In addition, a mean surface temperature is required to represent the overall surface cooling, and is calculated considering the effective area. Figure 4.27 represents the mean surface temperature variation with time at different temperatures. As given in Figure 4.28, the comparison reveals that the overall cooling is significant for the first (single) droplet impact compared to the drop-on-drop impact configuration. Nevertheless, as shown in Figure 4.26, it should be noted that the area being cooled, is improved during the drop-on-drop impact.

The present study investigates two configurations of droplet impingement: single droplet as well as the drop-on-drop. The pre-impacting surface temperatures are different for drop-on-drop impact, compared to that of single droplet impact. Therefore, a dimensionless temperature, T^* is defined and given as,



(a) Surface centre temperature versus time (b) Surface mean temperature versus time

Fig. 4.28: Comparison of single and drop-on-drop impact over the surface with temperature 154 °C

$$T^* = \frac{T_i - T_f}{T_i - T_\infty} \quad (4.18)$$

where T_i, T_f are initial and final surface temperatures respectively and T_∞ being the ambient temperature, in order to compare the two configurations considered in the present study.

Figure 4.29 (a) and (b) shows the distribution of dimensionless temperature at the instant of maximum spread during the single droplet and drop-on-drop impact over the surface with a temperature of 154 °C respectively. The comparison of the dimensionless temperature along the identified centreline is given in Figure 4.29 (c). For the single droplet, dimensionless temperature (T^*) of about 0.3 is observed in the interacted area. Whereas, in the case of drop-on-drop impact configuration due to the presence of sessile droplet, the cooling effect has reduced, with a T^* Value of 0.1 in most of the spreading region. However the surface cooling has improved ($T^* \sim 0.3$) in the peripheral of the droplet spread. Thus, the investigation confirms that there is always a decline in cooling effect by the trailing droplet during drop-on-drop impingement.

To quantify the heat transfer characteristics of the impingement configurations considered in the study, an effectiveness ratio (ϵ) is used which is defined as the ratio of dimensionless heat input during the drop-on-drop impact to that of a single droplet impact.

$$\epsilon = \frac{(Q^*)_{drop-on-drop}}{(Q^*)_{single}} \quad (4.19)$$

It provides a better understanding of each droplet performance (during consecutive droplet impact) in cooling the surface at different wall superheats, and the effect of

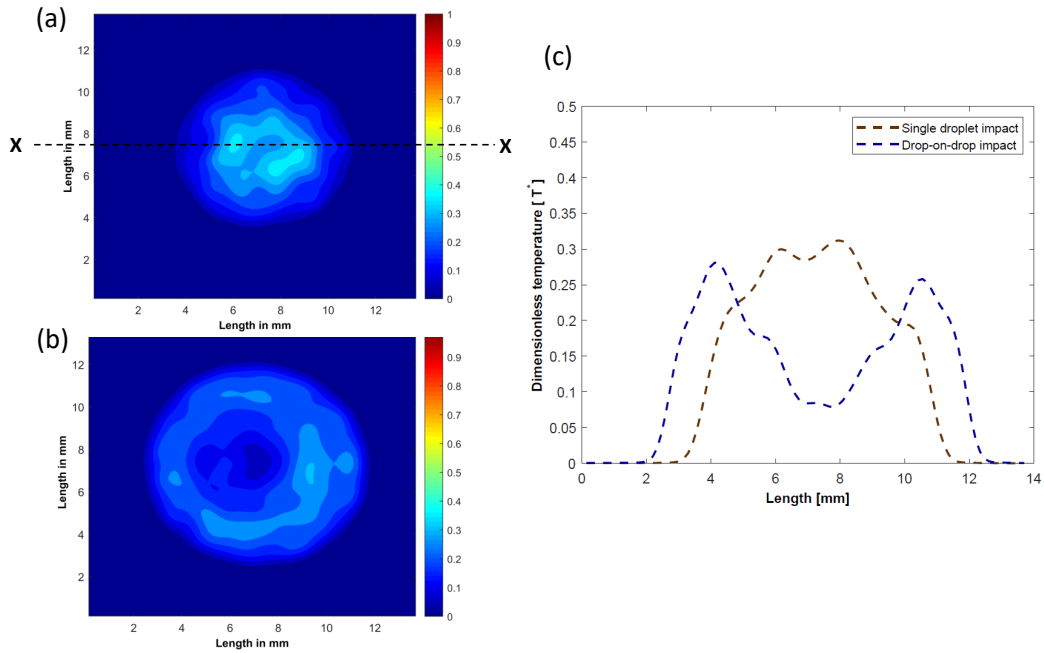


Fig. 4.29: Comparison of dimensionless temperature ($T = 154 \text{ }^\circ\text{C}$) (a) Single droplet impact (b) Drop-on-drop impact (c) Distribution along the centreline X-X

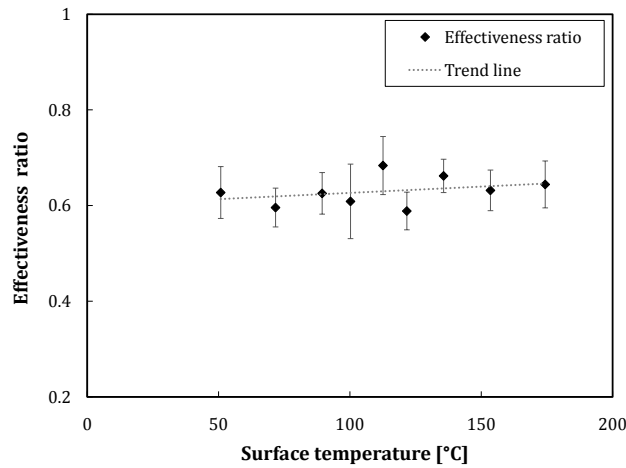


Fig. 4.30: Effectiveness versus temperature

droplet coalescence on spread and heat transfer characteristics during the impingement. Figure 4.30 shows the effectiveness ratio for different surface temperatures. The ratio is found to be nearly constant around a value of 0.62 for all observed temperatures. It can be inferred that the heat transfer for a trailing droplet is always lower compared to a leading droplet during the drop-on-drop configuration. The pre-cooling of the surface caused by the initial droplet, reduces the surface mean temperature, and thereby decreases the heat removal rate of the trailing droplet. It is worth noted that the magnitude of reduction in heat transfer could be influenced by the droplet flow rate, which controls the surface mean temperature. Also, the boiling

regimes such as nucleate boiling with rigorous bubbles, and film boiling, can determine the outcomes of drop-on-drop impingement phenomenon. In the present work, the flow rate was constant at 20 droplets per minute (DPM), and the adopted surface temperatures are not adequate to initiate the bubbles (of nucleate boiling) in the droplet. Further investigations are needed to analyze these parameter effects on the spread and evaporation dynamics.

Three-phase contact line region: Temperature and heat flux distribution

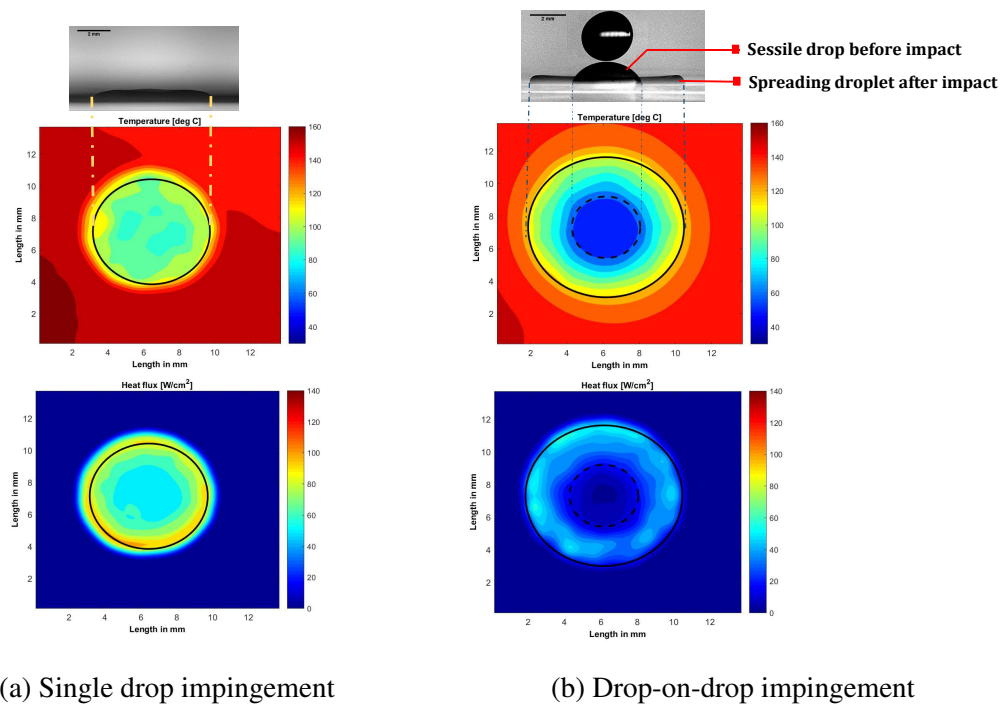


Fig. 4.31: Post-impact behaviour over the target surface ($T = 154 \text{ }^\circ\text{C}$; $t = 8 \text{ ms}$)

Figure 4.31 shows the temperature and heat flux distribution of the target surface during single droplet and drop-on-drop impact at an instant. The spread diameter estimated from the high speed image is superimposed onto the infrared temperature and heat flux images. It is observed that the surface temperature increases in the radial direction from the center of the droplet (impact point). For both configurations, the maximum heat flux value is recorded in the vicinity of three-phase contact line as shown in Figure 4.31 and is found to be significant in receding phase. Low film thickness near the contact line region is attributed to the observed high heat transfer rates. For the case of drop-on-drop impingement, Figure 4.31(b) also unveils that there is an effective heat transfer in the annulus portion i.e., the region of change in spread

and thereby extends the area being cooled. These observations will be used in further sections to develop a model for estimating droplet heat transfer during impingement.

4.3.2 Analytical modelling

Maximum spread

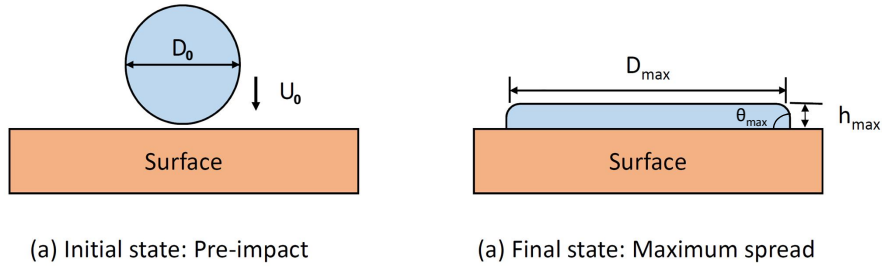


Fig. 4.32: Single drop impact: Maximum spread

Earlier studies (Chandra and Avedisian, 1991; Pasandideh-Fard *et al.*, 2001; Wakefield *et al.*, 2016) modelled the maximum spread theoretically using the energy conservation principle. Two instances during the droplet impingement are considered i.e., pre-impact state and the instant of maximum spread. The associated kinetic, potential and surface energies are taken into consideration to estimate the maximum spread factor. The theoretical models proposed in the literature are adopted in the present work in order to validate the present experimental observations. Batzdorf (2015) implemented an analytical model for evaluating the maximum spread during the single droplet impact over a hot surface. A schematic of the droplet system with the initial and final states considered are presented in Figure 4.32. Using energy balance it is shown (Batzdorf, 2015) that the maximum spread can be calculated from following equation.

$$We + 4Bo + 12 - 3(1 - \cos(\theta_{max}))S_{max}^{*2} = \frac{9a}{2} \frac{We}{Re(1 - Q_e^*)} S_{max}^{*4} \quad (4.20)$$

where θ_{max} and Q_e^* are contact angle at the instant of maximum spread and dimensionless evaporated mass, respectively. The dimensionless evaporated mass (Q_e^*) is given as

$$Q_e^* = \frac{m_e}{m_{single}} \quad (4.21)$$

' m'_e and ' m'_{single} are the cumulative evaporated mass and pre-impacting droplet mass.

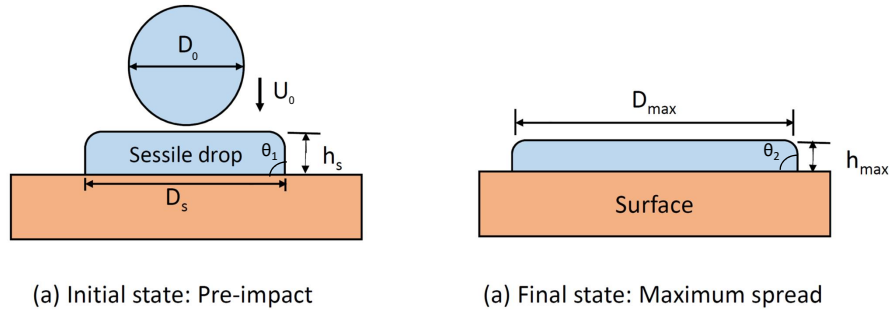


Fig. 4.33: Drop-on-drop impact: Maximum Spread

A similar approach was applied to the drop-on-drop impingement over a hot surface (see Chapter 3) as shown in Figure 4.33. In this case, the maximum spread factor is derived as

$$AS_{max}^*{}^5 + BS_{max}^*{}^3 + CS_{max}^* + D = 0 \quad (4.22)$$

where

$$A = \frac{18}{4} a \frac{We}{Re} \frac{1}{(1+c^3)(1-Q_e^*)} \quad (4.23)$$

$$B = 3(1 - \cos \theta_2) \quad (4.24)$$

$$C = -(We + 4Bo + \frac{16c^3Bo}{3S_{in}^*{}^2} + 3S_{in}^*{}^2(1 - \cos \theta_1) + \frac{8c^3}{S_{in}^*} + 12) \quad (4.25)$$

$$D = 8(1 + c^3)(1 - Q_e^*) \quad (4.26)$$

and

$$\text{Bond number, } Bo = \frac{\rho_l g D_0^2}{4\sigma_{lv}} \quad (4.27)$$

$$\text{Reynolds number, } Re = \frac{\rho_l D_0 U_0}{\mu} \quad (4.28)$$

$$\text{Weber number, } We = \frac{\rho_l D_0 U_0^2}{\sigma_{lv}} \quad (4.29)$$

$$\text{Maximum spread factor, } S_{max}^* = \frac{D_{max}}{D_0} \quad (4.30)$$

$$\text{Initial spread factor, } S_{in}^* = \frac{D_s}{D_0} \quad (4.31)$$

Where, θ_1 and θ_2 are the corresponding contact angles at the initial and final states.

Here constant ' a ' is taken as 15, in order to approximate the present experimental observations, and ' c ' is the radius ratio of impacting to sessile droplet ($c = 1$). In the present work, the liquid used is deionized water which is non-volatile and for the surface temperatures used, the total evaporation time of droplet is ranging from 720 seconds (at 50 ° C) to 100 seconds (at 175 ° C). The time interval between the two consecutive droplets at the considered flow rate of 20 droplets per minute (DPM) is around 3 seconds, and the total evaporated mass during this time is assumed to be negligible for the sessile droplet (equal volume as the impacting droplet) in the analytical model given in Equation 4.22. The evaporated mass during the impingement is calculated from the side view images of the droplet, and is used in Equations 4.20, 4.23 and 4.26 to estimate the maximum spread factor.

It should be noted that the above correlations are able to capture the effects of all influential dimensionless parameters such as Weber number (We), Reynolds number (Re) and Bond number (Bo). The surface temperature effects are also considered in the form of evaporated mass (Q_e^*) and obtained contact angles (θ_1, θ_2) at respective temperatures. The present impingement scenario corresponds to an impact condition with $We = 50$, $Bo = 0.27$; and $Re = 3180$. The theoretical maximum spread factor at different temperatures are calculated using Equations 4.20 and 4.22 for single droplet and drop-on-drop impact respectively. The computed results are compared against experimental values as shown in Figure 4.34. The implemented theoretical models are found to be efficient in capturing the maximum spread values, and agreed well with experimental values within a deviation of 8% at all temperatures.

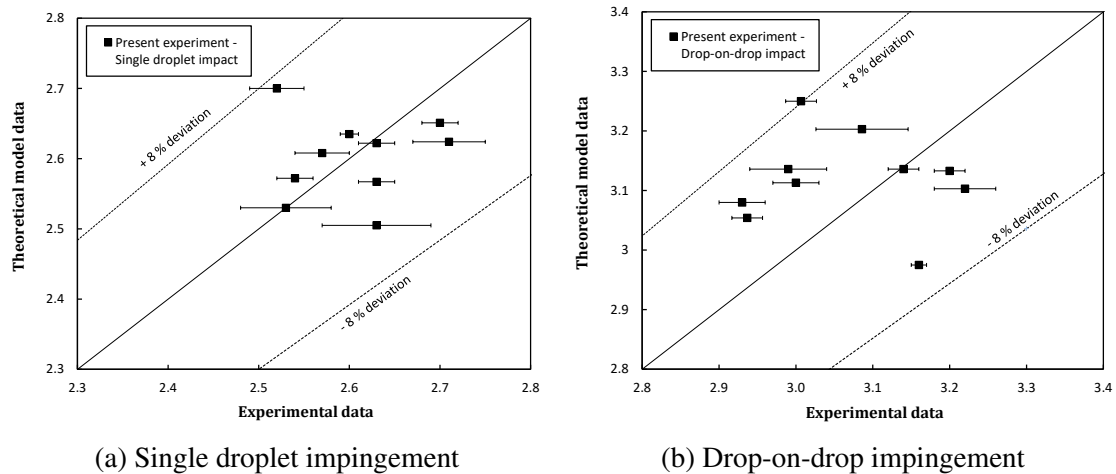


Fig. 4.34: Maximum spread factor: Experimental versus theoretical

Input heat transfer

As explained in Chapter 3, it is evident that the bulk of heat transfer takes place during the spreading phase, and is accompanied by convection heat transfer, which can be modelled using a Nusselt number correlation. Assuming the spreading droplet as a single impinging jet, Batzdorf (2015) developed a theoretical model for estimating the overall heat transferred during the spreading phase which is proportional to the convective heat transfer, and is reproduced below.

$$Q^* = 3b \frac{S_{max}^* (S_{max}^* - 1.1)}{(S_{max}^* - 0.6)} \frac{(1 + 0.005 Re^{0.55})^{0.5} Ja}{Re^{0.5} Pr^{0.58}} \tau_{max} \quad (4.32)$$

Here, Q^* is the effectiveness which is represented as

$$Q^* = \frac{\int_0^t (Q_{drop}) dt}{m h_{lv}} \quad (4.33)$$

where all relevant properties are calculated at the film temperature, and the constant 'b' is taken as 0.1 in order to fit the experimental data.

The above correlation was used for estimating the heat transfer during single and drop-on-drop impact over the hot surface. The maximum spread factor S_{max}^* and the corresponding non-dimensional time τ_{max} during the initial cycle which is of order $\tau_{max} \sim 2$ ($t = 5$ ms) for single droplet impingement and $\tau_{max} \sim 3$ ($t = 7.5$ ms) for drop-on-drop impact, are taken from the experimental observations. Nonetheless, for drop-on-drop impingement, it is found that the effective heat transfer takes place in the annulus region of the initial and post-impact droplet spread, as shown in Figure 4.31 (b). Hence, to obtain an accurate estimation of heat transfer, the *net spread factor* is more relevant and used in the Equation 4.32. Whereas for the single droplet impact, the spread factor and the corresponding time values are used. The theoretical results obtained is found to agree well with the experimental findings as shown in Figure 4.35. Especially for the drop-on-drop impact, the model is able to capture the heat transfer rate efficiently using *net spread factor*. The maximum deviation in the results are about 20 % and can be considered as a good approximation for heat transfer calculations.

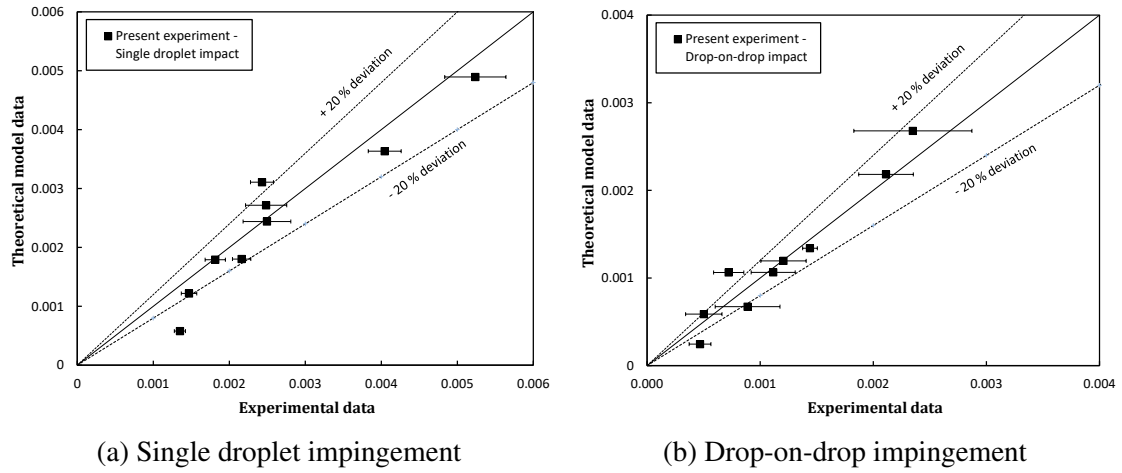


Fig. 4.35: Effectiveness: Experimental versus theoretical

Previous studies concerning the droplet impact over the heated surfaces are considered to validate the proposed correlations and examine the sensitivity of the constants ' a ' and ' b ' described in the Equations 4.20, 4.22, and 4.32. E.Teodori *et al.* (2018) carried out the thermographic analysis of interfacial heat transfer mechanisms on drop/wall interactions. Single droplets of water and ethanol and a heated stainless steel surface ($25\mu\text{m}$), are utilized. The study examined the effect of the surface temperature, liquid surface tension, and wettability on heat transfer processes during a single droplet impact. Jung *et al.* (2016) conducted heat transfer analysis of droplet collision over superheated surfaces and detected a dynamic Leidenfrost point based on the droplet heat transfer. In this work, water droplet impingement is carried out over the superheated platinum-coated sapphire glass maintained at temperatures of 176 - 226 °C. The details of the impingement studies, used for the present validation, are summarized in Table 4.4. The maximum spread factor, and the corresponding effectiveness, as per equation 4.33, is calculated using the data from references (E.Teodori *et al.*, 2018; Jung *et al.*, 2016) and compared with the theoretical values from Equations 3.17 and 4.32. The constants ' a ' and ' b ' are chosen such that the theoretical values fit well with the experimental outcomes.

Figures 4.36 (a) and (b) show the comparison of experimental observations with theoretical results of maximum spread factor and effectiveness, respectively. In the case of E.Teodori *et al.* (2018), the experimental conditions (liquid on the heated hydrophilic surface) are similar to the present work. so, the values of the constants $a = 15$ and $b = 0.1$ are considered. With these values, the correlations predicted the outcomes for the cases of the water droplet on the stainless steel surface (hydrophilic and super-hydrophobic)

Table 4.4: Experimental details of the considered literature cases in the analysis

Reference	Liquid-Surface	We	Re	Surface temperature (°C)	a	b
E.Teodori <i>et al.</i> (2018)	Water on stainless steel (hydrophilic)	22.8	1980	100	15	0.1
E.Teodori <i>et al.</i> (2018)	Water on stainless steel (hydrophilic)	22.8	1980	60	15	0.1
E.Teodori <i>et al.</i> (2018)	Water on coated stainless steel (superhydrophobic)	22.8	1980	100	15	0.1
E.Teodori <i>et al.</i> (2018)	Ethanol on stainless steel (hydrophilic)	50	1221	60	15	0.1
Jung <i>et al.</i> (2016)	Water on platinum coated sapphire (highly superheated)	6.3	1130	176	1	1.4
Jung <i>et al.</i> (2016)	Water on platinum coated sapphire (highly superheated)	6.3	1130	206	1	1.4
Jung <i>et al.</i> (2016)	Water on platinum coated sapphire (highly superheated)	6.3	1130	221	1	1.4
Present experiment	Water on Inconel surface (hydrophilic)	50	3180	22 - 175	15	0.1

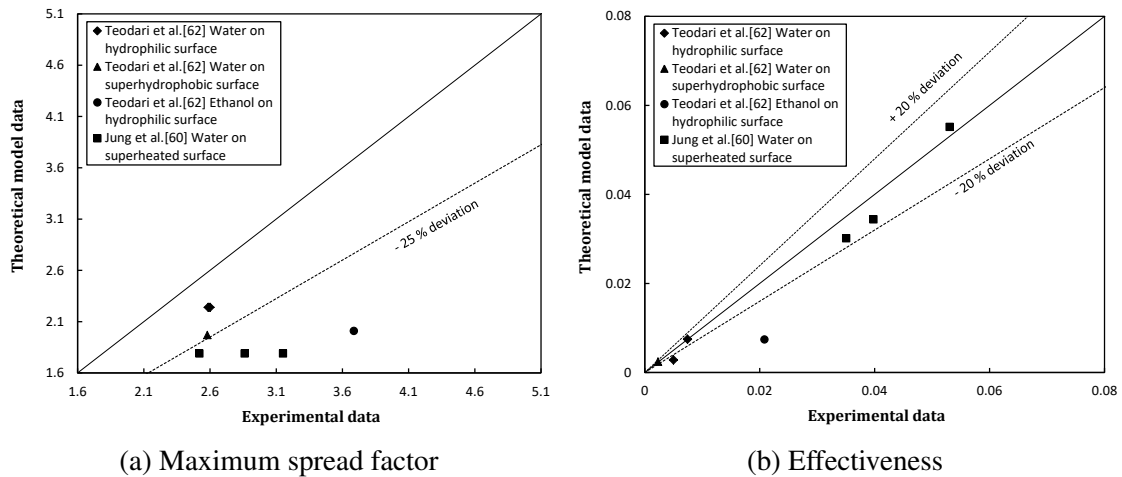


Fig. 4.36: Validation: Experimental versus theoretical

within the acceptable range. On the contrary, significant deviations in the results, are observed during the case of ethanol droplet impact over the heated surface. On the other hand, for the cases of Jung *et al.* (2016), the constants $a = 1$ and $b = 1.4$ are found to provide a better approximation for the experimental observations. While the model for the maximum spread factor under-predicts the results, the effectiveness is observed to be within 25 % deviation, as given in Figure 4.36. The discrepancy with the spread factor prediction is due to the boiling phenomena reported in the droplet. And there is a need to account these effects, which are not included in the present model.

Moreover, in the previous studies of Batzdorf (Batzdorf, 2015), the values $a = 8/3$ and $b = 4/3$, are adopted for FC-72 droplet collision over chromium surface and obtained a good approximation for the cases studied. During the present numerical work (see chapter 3) it is extended to the drop-on-drop impact of FC-72 and the values of the

same order, $a = 8/3$ and $b = 3.4$ are utilized to estimate the quantities. With these observations, it is determined that the analytical models are efficient in capturing the spread and heat transfer dynamics for the given constants ' a ' and ' b ', and these values are sensitive to the nature of the liquid, surface, and boiling regimes (wall superheat).

4.4 FC-72 liquid droplet impingement

A train of FC-72 droplets of diameter 1.2 mm is impacted at a constant flow rate of 60 DPM (droplets per minute) over a thin Inconel surface (of thickness $25 \mu\text{m}$) maintained at a constant temperature using a DC power supply. The droplets are generated using a micro p-pump and made to fall from a height of 5 mm under gravity with the constant flow rate. The impact velocity of the droplet, U , is calculated by tracking it in the high-speed images and is about 0.3132 m/s, which corresponds to a Weber number of 20 ± 1 and Reynold number of 986 ± 27 . Surface temperature is chosen as a parameter and varied from $29 \text{ }^\circ\text{C}$ (non-heated) till $105 \text{ }^\circ\text{C}$ (Dynamic Leidenfrost temperature), where complete de-wetting takes place upon impact for the given conditions. The schematic showing the present experimental apparatus is given in Fig.4.1. The droplet impingement is carried in ambient conditions with a room temperature of $25 \text{ }^\circ\text{C}$ and relative humidity of 55%.

A high-speed camera (*Photron fastcam SA3 120K*) with a frame rate of 10000 FPS (frames per second) and a spatial resolution of $20 \mu\text{m}/\text{pixel}$, is used to capture the side-view images, whereas the surface temperature is monitored using an infrared camera (*FLIR X6540sc*), triggered simultaneously, at 1000 FPS and with a spatial resolution of $136 \mu\text{m}/\text{pixel}$. The bottom of the surface is painted black to improve its response to the infrared camera. Upon impact over the surface, a droplet performs a series of cycles with spreading and receding phases until it settles down as a sessile droplet. For each configuration, i.e., the single droplet and drop-on-drop impact, the droplet dynamics is captured for one cycle of spreading and receding which corresponds to a time of 45 milliseconds (non-dimensional time $\tau = 12$) and the time interval between the droplets is nearly 1 second with present droplet flow rate.

The infrared camera is factory calibrated for the temperature range of 278 K to 673 K with an absolute uncertainty of ± 1 K. The relative uncertainty associated with

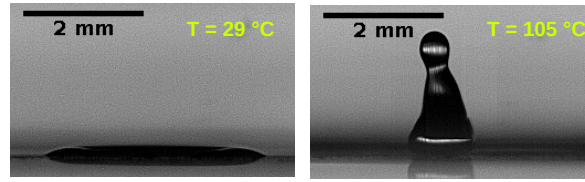


Fig. 4.37: FC-72 droplet behaviour ($t = 10$ ms) over a non-heated surface (29 °C) and at Dynamic Leidenfrost temperature (105 °C)

the heat generation Q_g is within 12% (maximum at $T = 105$ °C). At least three events of the droplet impact are carried out for each configuration, and the mean values of the outcomes are presented. The uncertainty associated with measurements of droplet spread factor, and input heat transfer is within 8 % and 16 % respectively.

4.4.1 Results and Discussion

The droplet spread hydrodynamics is analyzed from the side-view images, which are recorded using the high-speed camera. While the infrared camera captures the surface temperature variation from the underside of the surface. Being a highly volatile and wetting liquid, FC-72 displays different hydrodynamics at various temperatures. At a temperature of 105 °C, the FC-72 droplet completely de-wets the surface contrasting its highly wetting behaviour at room temperature. This temperature corresponding to the given impact conditions ($We = 20$, $Re = 986$) is the Dynamic Leidenfrost Point (DLP). A comparison of FC-72 droplet behaviour over a non-heated surface and at Dynamic Leidenfrost temperature is shown in Figure 4.37. Observations (Okawa *et al.*, 2012; Bernardin and Mudawar, 2002; Pedersen, 1970) revealed that there is a drastic decrease in heat transfer because of the droplet de-wetting above the Leidenfrost temperature (in film boiling regime). Thus, in the present work, the surface is only maintained at different temperatures to Dynamic Leidenfrost temperature. Also, it is noted that the drop-on-drop impact is no longer realized at Leidenfrost temperature, as the droplets bounce off by the time the trailing drop impacts onto the initial droplet. The spread hydrodynamics and heat transfer associated with the two consecutively impinging droplets is compared till the DLP. Various surface temperatures maintained in the study is shown in Table. 4.5.

An energy balance is applied at the surface, and the droplet input heat transfer is calculated considering the temporal change of the surface temperature, conduction

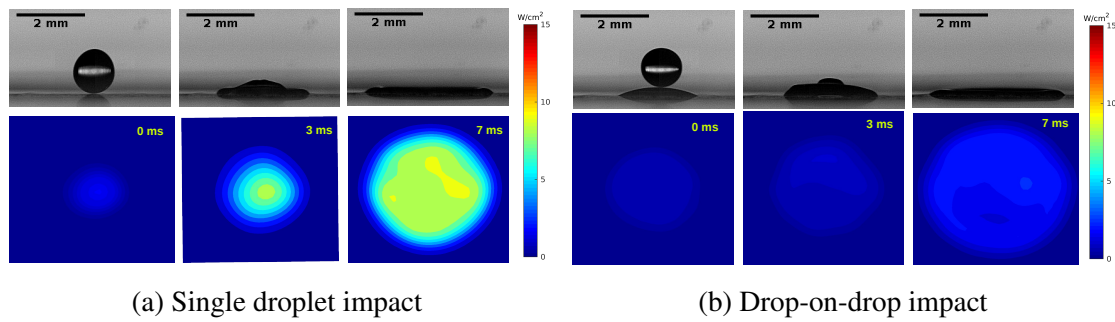


Fig. 4.38: Droplet impingement over the surface at a temperature of 57 °C

effects along with the surface and heat dissipation through convection and radiation heat transfers from the underneath of the surface. Figures 4.38a and 4.38b shows the droplet spread dynamics (side-view images) and corresponding droplet input heat transfer (from infrared images) for single droplet and drop-on-drop impact over the surface at a temperature of 57 °C respectively. It is observed that during the drop-on-drop impingement, the droplet input heat transfer is lower compared to a single droplet impact. The decrease in the surface mean temperature, and the increase in thermal resistance due to the presence of the second droplet reduced the droplet input heat transfer. Figure 4.39 presents the droplet-surface interaction at a temperature of 105 °C, where the droplets are bouncing on the surface due to the Leidenfrost effect. Because of the de-wetting, droplet input heat transfer from the surface is decreased. Details regarding the droplet dynamics are provided in the subsequent sections.

Spread hydrodynamics

Figures 4.40a and 4.40b presents the variation of the spread factor with non-dimensional time for single droplet and drop-on-drop impact, respectively. As soon as the droplet impacts the surface, it exhibits cycles of advancing and receding phases until it settles down as a sessile droplet. Observations revealed that the effect of the temperature is realized from the initial stage of droplet spreading, and the extent of spread decreases at high temperatures as it is evident in the receding phase in Figure 4.40. At Dynamic Leidenfrost Point (DLP), a low spread factor is recorded due to the surface de-wetting, which consequently affects the input heat transfer. The cycles of spreading and receding are more distinguishable at higher temperatures compared to a non-heated surface due to a change in surface wetting characteristics with temperature, i.e., super-wetting over

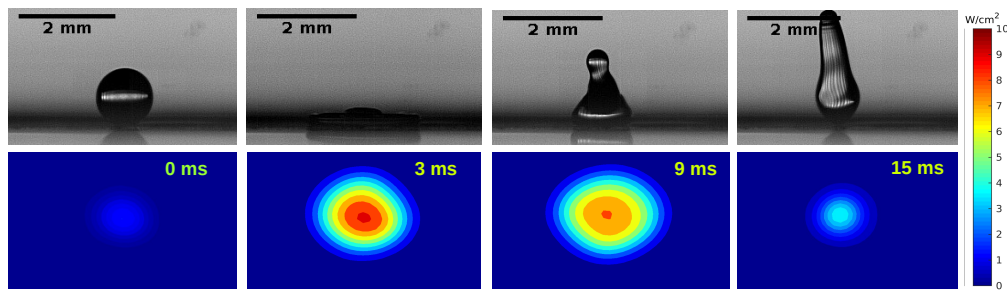


Fig. 4.39: Single droplet impingement over the surface at a temperature of 105 °C : Dynamic Leidenfrost Point

Table 4.5: Various surface temperatures used in the present study ($T_{sat} = 56$ °C)

S.No	Temperature (°C)	Degree of Superheat(°C)
1	29 (Non-heated)	27 (Subcooling)
2	57	1 (Superheat)
3	70	14 (Superheat)
4	78	22 (Superheat)
5	94	38 (Superheat)
6	99	43 (Superheat)
7	105 (DLP)	49 (Superheat)

a non-heated surface changed to non-wetting behavior at DLP.

While in drop-on-drop configuration, the overall maximum spread is high, but the change in spread factor is low compared to single droplet impact. The more the change in spread factor, the high the effective area of the surface interacted with the droplet. Thus, due to the presence of a sessile droplet, the change in spread factor decreases, resulting in low droplet input heat transfer rate. Figure 4.41 provides the temporal variation of change in spread factor at various temperatures. On the other hand, with the increase in temperature, the quantity of sessile droplet being evaporated increases. Thus the extent of coalescence of impacting droplet with the sessile drop is reduced at high temperatures, resulting in the heat transfer improvement.

Heat transfer characteristics

The droplet input heat transfer, which dictates the extent of cooling of the surface, is calculated and examined during the single droplet and drop-on-drop impingement at different temperatures. Figures 4.42a and 4.42b shows the variation of average droplet input heat transfer and found that the temperature rise leads to an increase in the input

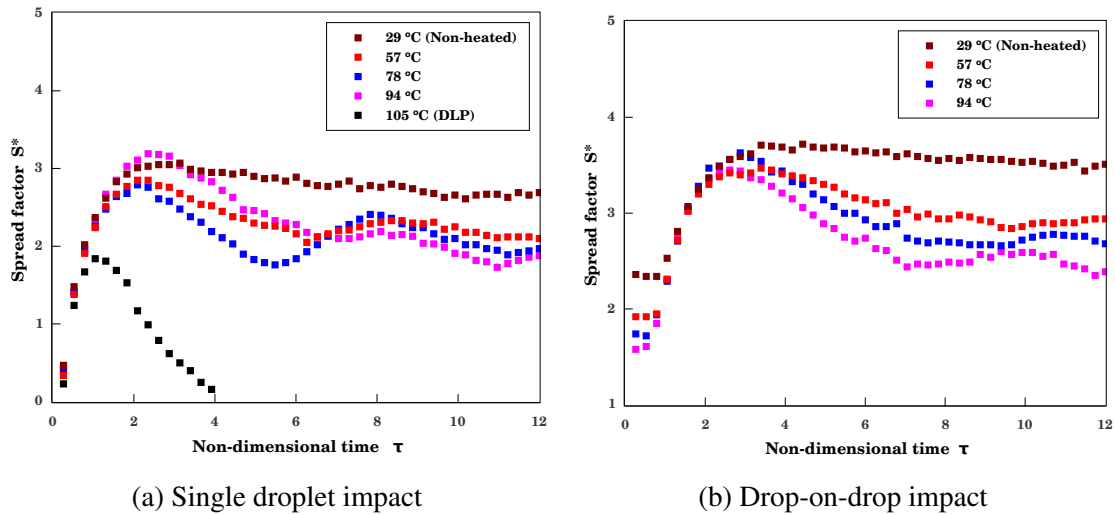


Fig. 4.40: Spread factor versus Time

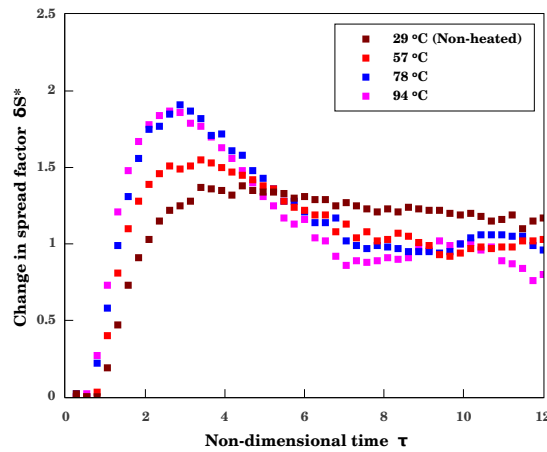


Fig. 4.41: Drop-on-drop impact: Net Spread factor versus Time

heat transfer in both cases. However, as soon as it reaches the Dynamic Leidenfrost Point, there is a significant reduction in heat transfer which indicates the boiling regime change from, typically, nucleate boiling to a transition to the film boiling. Also, the maximum heat transfer is taking place during the advancing phase (spreading) of the initial cycle at all temperatures in both the configurations. However, the comparison among the single and drop-on-drop configurations reveal that, at all temperatures, there is a decrease in droplet input heat transfer for the drop-on-drop collision. An increase in the thermal resistance due to the presence of two droplets (see Chapter 3) and the decrease in surface mean temperature due to the initial droplet, are affecting the droplet heat transfer during the drop-on-drop collision.

A similar trend is observed, as shown in Figs. 4.43a and 4.43b, even in terms of dimensionless heat transfer, that there is a decline in heat transfer during single droplet

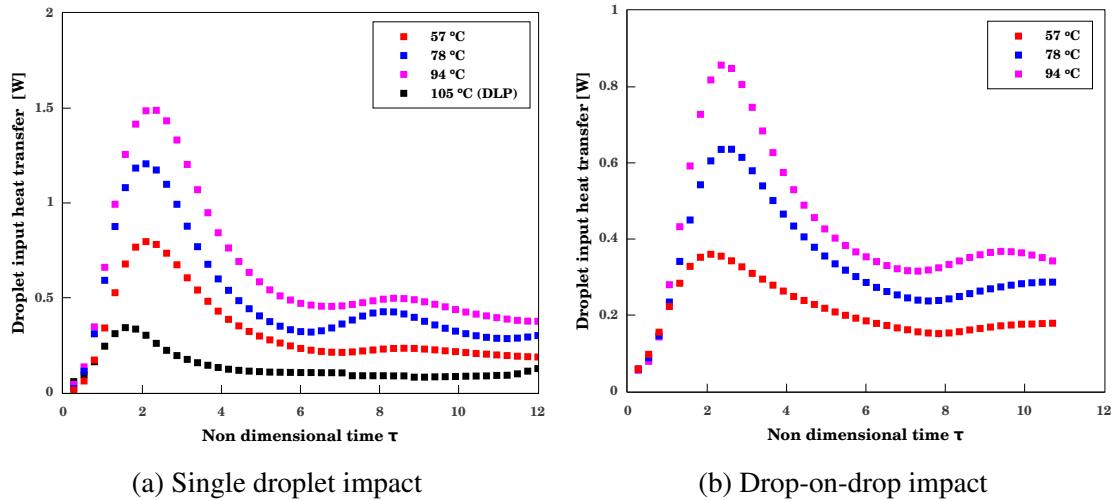


Fig. 4.42: Input heat transfer versus Time

at Leidenfrost temperature. Also, the overall droplet input heat transfer decreases during drop-on-drop impingement at all corresponding temperatures when compared to single droplet impact.

To realize the boiling regimes associated with droplet impact with present conditions ($We = 20$ and $Re = 986$), the dimensionless input heat transfer observed during the single droplet impact at various temperatures, considered in the study, are plotted against the wall superheat (excess surface temperature) provided in Tab.4.5. Figure 4.44 shows the boiling regimes perceived from previous studies (Liang and Mudawar, 2017) based on the observed droplet input heat transfer. Since the high-speed imaging of bubble formation inside the drop is out of reach with the employed experimental methodology, the regime is approximated based on the slope of the curve plotted in the Fig.4.44. The rapid change in the slope, i.e., increase in heat transfer is an indication of nucleate boiling leading to the critical heat flux value followed by a transition region (Leidenfrost Point) to the film boiling. Even though the droplet is above the saturation temperature, bubble nucleation will form only at the desired wall superheat conditions. Thus, for the present impact conditions, Film evaporation will be prominent until a wall superheat of 40K followed by nucleate, transition, and film boiling.

The other essential parameter required to enhance the understanding of cooling during the droplet impingement is the surface temperature variation. A centre temperature is used to track the changes in the surface temperature and it is the initial impact point of the droplet over the surface. Observation revealed that this impact

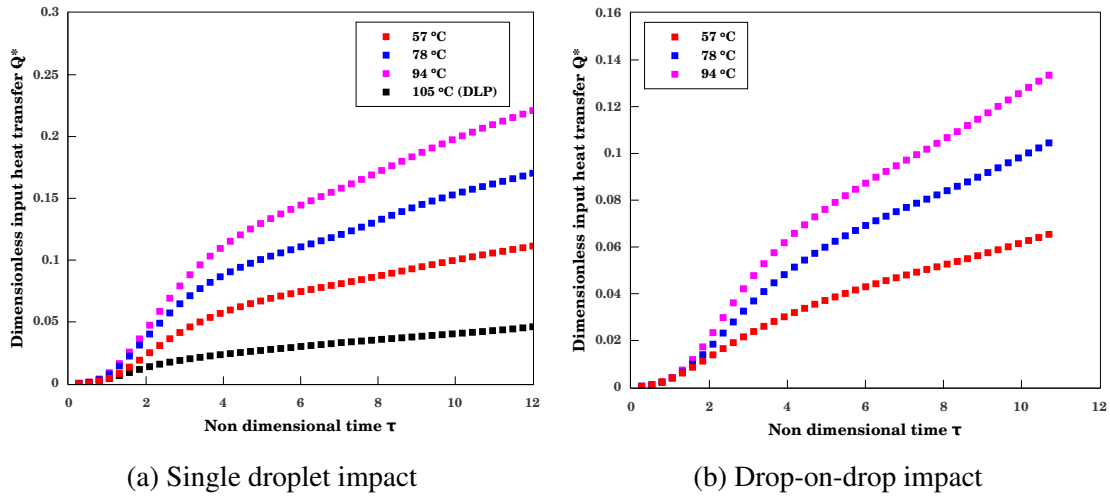


Fig. 4.43: Dimensionless input heat transfer versus Time

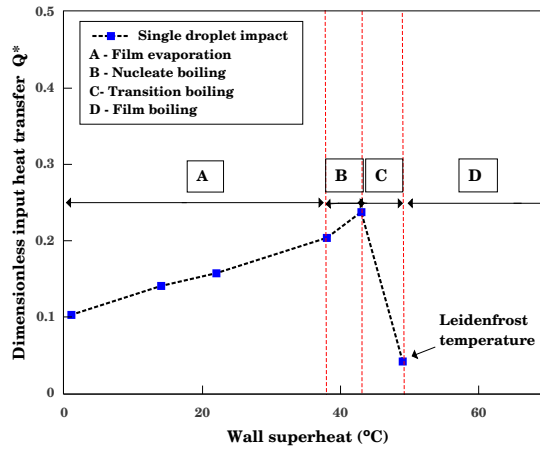


Fig. 4.44: Single droplet impingement: Boiling regimes ($We = 20$ and $Re = 986$)

point temperature is the lowest temperature point in the droplet-surface interaction area. Figures.4.45a and 4.45b presents the variation of surface centre temperature during single and drop-on-drop impact at various temperatures. It is observed that the maximum cooling effect, i.e., the reduction in surface temperature, is achieved in the initial cycle of spreading and receding itself, for the single droplet impact (which is $t = 40$ ms) at all the given temperatures. Thus after the initial cycle of droplet impingement, the surface temperature is already decreased and maintains a constant value until the second droplet impacts with the surface. Subsequently, there is always a lower cooling effect for the trailing droplet in a droplet train impingement because of the reduction in temperature during the initial droplet interaction with the surface. This observation may change by varying other factors, such as using a high droplet flow rate, which can be concluded with a few more experimental investigations.

However, the effective area, where a considerable amount of heat transfer takes place, is improved in the case of drop-on-drop impact. Figures 4.46a shows the dimensionless effective area versus non-dimensional time, concluding that the effective area, which is being cooled, is improved during the drop-on-drop impact compared to single droplet impingement. At a given temperature, the rise in the spread factor due to the two droplets is resulting in an increased effective cooling area.

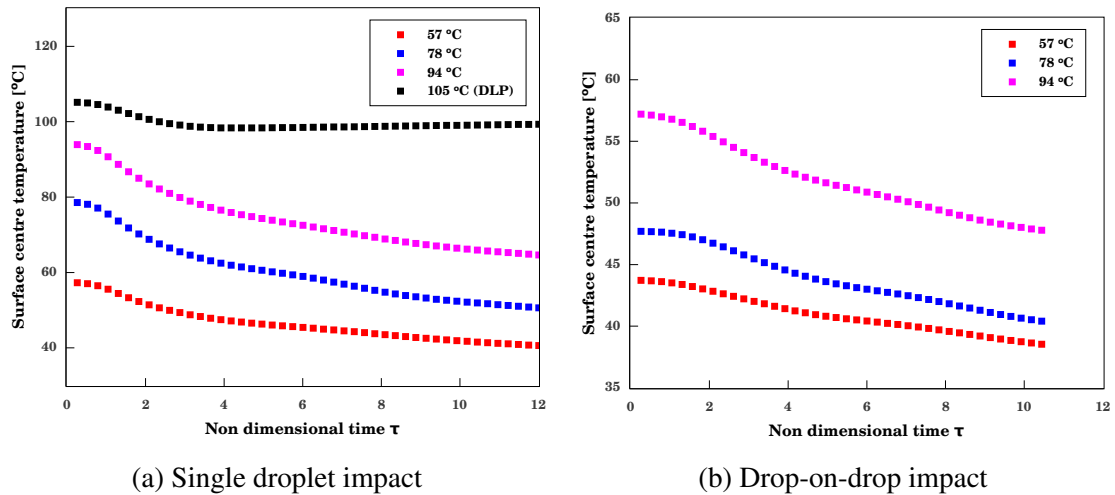


Fig. 4.45: Surface centre temperature versus Time

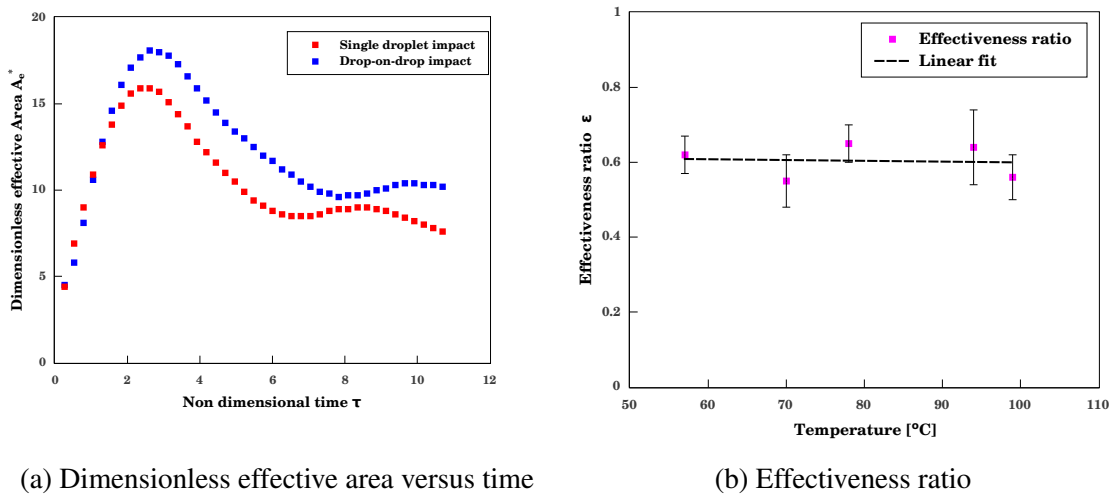


Fig. 4.46: FC-72 droplet impingement over a heated surface

Effectiveness ratio

To compare the surface cooling effect, the effectiveness ratio is calculated at various temperatures considered in the study and plotted, as shown in Fig. 4.46b. It is interesting to find that the ratio is nearly constant, around 0.6, in all observed regimes

and confirmed that there is always a decrease in the droplet heat transfer during the drop-on-drop impingement. The initial cooling occurred due to the first droplet, results in the reduction of surface mean temperature, which can justify the low droplet heat transfers. Also, on the other hand, there is an increase in thermal resistance for heat transfer due to the droplet coalescence, affecting the overall heat flow during the second droplet interaction with the hot surface.

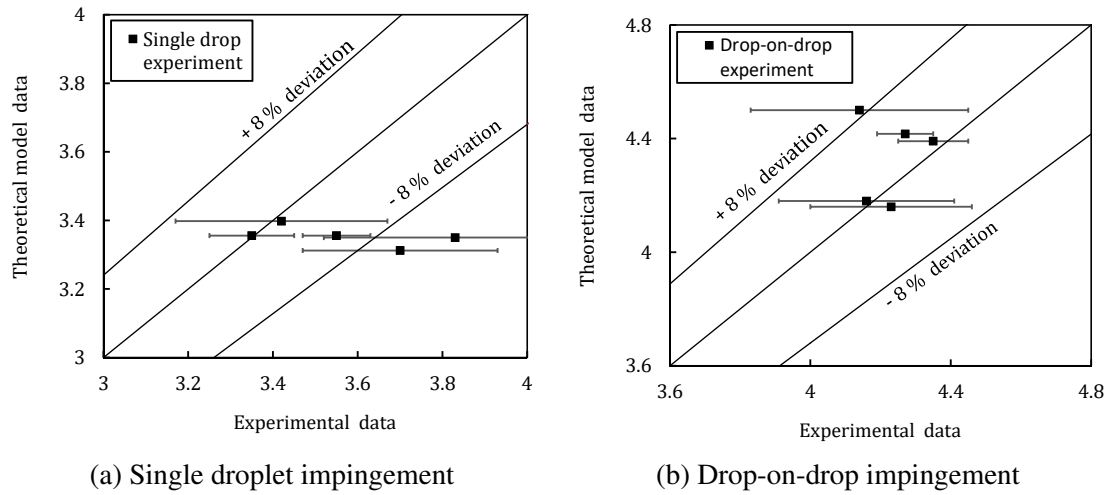


Fig. 4.47: Maximum spread factor: Experimental versus theoretical

4.4.2 Analytical modelling

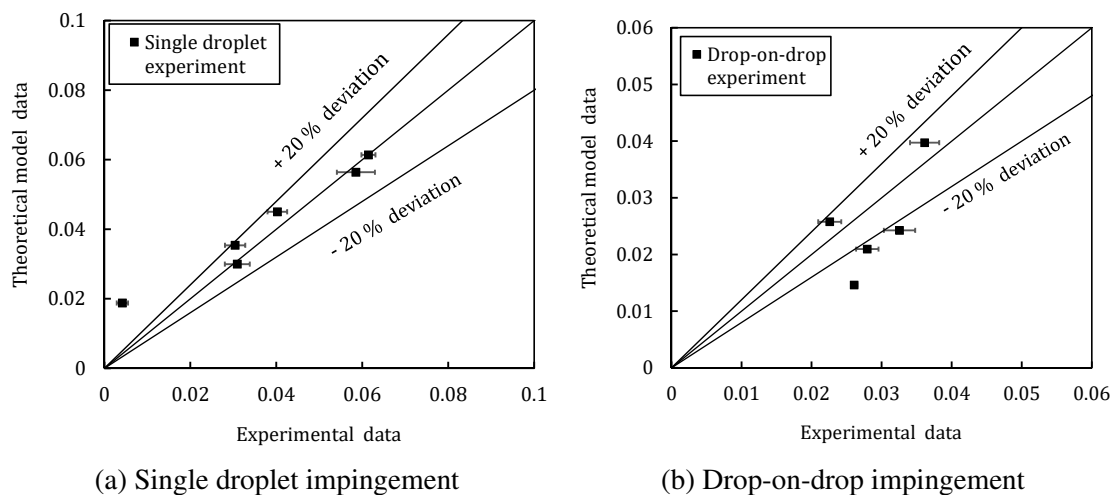


Fig. 4.48: Effectiveness: Experimental versus theoretical

In this section, the maximum spread factor and corresponding heat transfer during the FC-72 droplet impingement are calculated using the proposed analytical models. Equations 4.20, 4.22 and 4.32 are used, and a comparison with the experimental data

are presented in Figures 4.47 and 4.48. From section 4.3.2, it is observed that the constants ' a ' and ' b ' are sensitive and taking different values based on the nature of the liquid, surface, and boiling regime. The values $a = 2.67$ and $b = 0.5$ have given a good validation with the present experimental data, which complies with the previous studies using FC-72. (see chapter 3 and Batzdorf (2015)).

4.5 Closure

The present chapter discussed the experimental investigation of two consecutively impinging droplets over a heated surface in air-vapour medium. The details of experimental methodology and the outcomes of Water and FC-72 droplets impingement over a hot surface are provided. The next chapter discusses the numerical implementation of droplet impingement over a hot surface in air-vapour medium.

CHAPTER 5

NUMERICAL STUDY: DROPLET IMPACT OVER A HEATED SURFACE IN AIR-VAPOUR MEDIUM

5.1 Introduction

In this chapter, a numerical model is implemented in CFD open-source software OpenFOAM to simulate the droplet impingement in air-vapour medium (atmospheric conditions). By tracking the vapour concentration in the ambient air, the droplet evaporation is calculated, which is assumed to be driven by concentration gradients at the liquid-gas interface. Initially, to evaluate the efficiency of the model in capturing the evaporated mass, a sessile droplet evaporation case is simulated and compared with the literature's experimental results. Following that, simulations of a single droplet impingement over a heated surface is carried out to validate against the experimental observations of FC-72 droplet impact. A static and dynamic contact angle (contact line evaporation model) analysis is performed to realise the effect of contact angle hysteresis on spread and heat transfer dynamics. In the end, for a drop-on-drop impact scenario, a parametric study is carried out by varying the time interval between the two consecutively impinging droplets (droplet flow rate). The time interval considered in the study is of the order of droplet's spread-cycle time, i.e., milliseconds which corresponds to a droplet flow rate is of order 10^4 to 10^5 droplets per minute (DPM). The spread dynamics and corresponding droplet heat transfer for the single droplet (leading) and drop-on-drop (trailing droplet) are compared.

5.2 Numerical model

The numerical approach explained in chapter 3 is followed in this section. A phase change solver is implemented in the open-source CFD toolbox OpenFOAM with the VOF interface capturing technique. The event of drop-on-drop impingement is

modelled through the conservation of mass, momentum, and energy equations. Here a one-field approach is adopted, i.e., a single velocity, pressure, and temperature fields are implemented for both liquid and gas phases.

$$\rho(\nabla \cdot \vec{u}) = \dot{\rho} \quad (5.1)$$

$$\frac{\partial(\rho\vec{u})}{\partial t} + \nabla \cdot (\vec{u} \cdot \rho\vec{u}) = -\nabla p + \nabla \cdot [\mu(\nabla\vec{u} + (\nabla\vec{u})^T)] + \vec{f}_g + \vec{f}_\sigma \quad (5.2)$$

$$\frac{\partial(\rho c T)}{\partial t} + \nabla \cdot (\rho c \vec{u} T) = \nabla \cdot (k \nabla T) + \dot{h} \quad (5.3)$$

Where $\dot{\rho}$ and \dot{h} represents the evaporation mass and energy source terms respectively due to phase change of fluid. Here \vec{f}_g and \vec{f}_σ are the source terms which accounts for gravity and surface tension respectively. In this model, liquid and gases are assumed to be completely incompressible, and dissipation term in the energy equation is neglected. To capture the liquid-gas interface, an additional equation in terms of volume fraction α is solved.

$$\frac{\partial\alpha}{\partial t} + \nabla \cdot (\vec{u}\alpha) = \frac{\dot{\rho}}{\rho}\alpha \quad (5.4)$$

Where α is defined as the ratio of volume of liquid to the volume of the cell. Thus it assumes a value of 1 and 0 for the phases of liquid and gas respectively, and forms the interface between 0 and 1. All the properties (γ) at the interface cells can be calculated as volume weighted properties of the pure phases.

$$\gamma = \gamma_l\alpha + \gamma_v(1 - \alpha) \quad (5.5)$$

The surface tension source term \vec{f}_σ is given in terms of the interface curvature using continuum surface force model proposed by Brackbill *et al.* (1992)

$$\vec{f}_\sigma = \sigma K_c \nabla \alpha \quad (5.6)$$

Where curvature K_c , in terms of volume fraction α is given as

$$K_c = \nabla \cdot \frac{\nabla \alpha}{|\nabla \alpha|} \quad (5.7)$$

5.2.1 Evaporation model

Apart from the above equations, to track the mass concentration of vapour in the air during the droplet evaporation, a mass concentration equation is used as follows

$$\frac{\partial Y}{\partial t} + \nabla \cdot (\vec{u}Y) = \nabla \cdot (D_{AB} \nabla Y) + \frac{\dot{\rho}}{\rho} \quad (5.8)$$

Where Y is the mass concentration, D_{AB} is the diffusion coefficient and $\dot{\rho}$ is the evaporative mass flux due to the evaporation based on the Fick's law of diffusion is given as

$$\dot{\rho} = \frac{D_{AB} \rho_{gas} \nabla Y \delta_{int}}{1 - Y} \quad (5.9)$$

Where ρ_{gas} is density of the gas mixture and δ_{int} is the local interface density calculated at the identified interface. The concentration gradient at the interface is calculated as

$$\nabla Y = \frac{Y_v - Y_{int}}{d_{v,int}} \quad (5.10)$$

Y_v , Y_{int} and $d_{v,int}$ are the vapour concentration in neighbour cell, at the interface and distance to the neighbouring cell.

The vapour concentration is obtained using the saturated pressure condition corresponding to interface temperature. Wagner equation is used to calculate the saturated pressure p_{sat} which is given as

$$\ln \left(\frac{p_{sat}}{p_c} \right) = \frac{A' \left(1 - \frac{T}{T_c} \right) + B' \left(1 - \frac{T}{T_c} \right)^{1.5} + C' \left(1 - \frac{T}{T_c} \right)^3 + D' \left(1 - \frac{T}{T_c} \right)^6}{\frac{T}{T_c}} \quad (5.11)$$

T_c and p_c are the critical temperature and pressure respectively and the vapour concentration at the interface is calculated as

$$Y_{int} = \frac{p_{sat}}{p_{total}} \quad (5.12)$$

Where, p_{sat} and p_{total} is the saturation pressure corresponding to the interface temperature, and total atmospheric pressure respectively. The constants A' , B' , C' and D' are the Wagner constants which take specific values for a given liquid as shown in Table 5.1.

Table 5.1: Wagner coefficients for FC-72 and liquid Methanol

Constants	FC-72	Methanol
A'	-8.87027	-8.53690
B'	2.71065	0.73287
C'	-7.28479	-3.02500
D'	6.03269	1.36500

The interface temperature T_{int} is updated using the energy balance at the liquid-gas interface which is given as

$$\dot{\rho}_i h_{lv} V_i = S_{int,i} (k_l \nabla_{int} T_l + k_v \nabla_{int} T_v) \quad (5.13)$$

Where $\dot{\rho}_i$, $S_{int,i}$ and V_i are evaporative mass flux, surface area and volume of the i^{th} cell near the interface respectively and the local temperature gradients on liquid and gas phase sides are taken as

$$\nabla_{int} T_l = \frac{T_l - T_{int}}{d_{l,int}} \quad (5.14)$$

$$\nabla_{int} T_v = \frac{T_v - T_{int}}{d_{v,int}} \quad (5.15)$$

$d_{l,int}$ and $d_{v,int}$ represents the distances to the interface of the closest cell neighbour on either sides of the interface.

5.3 Validation of the model

5.3.1 Sessile droplet evaporation

The present numerical model is validated using a sessile droplet evaporation case. The simulated evaporated mass is evaluated by comparing with available literature's experimental data. Chen *et al.* (2017) performed numerical and experimental investigation of sessile droplet evaporation over non-heated substrates to study the transient effects and mass convection. A methanol droplet evaporation over the PTFE substrate is conducted. The droplet volume is around $3 \mu\text{l}$ with a contact radius of 1.75 mm and static contact angle of 36° . The ambient temperature is around 298 K and the relative humidity is taken as 0 % (methonal gas in ambient).

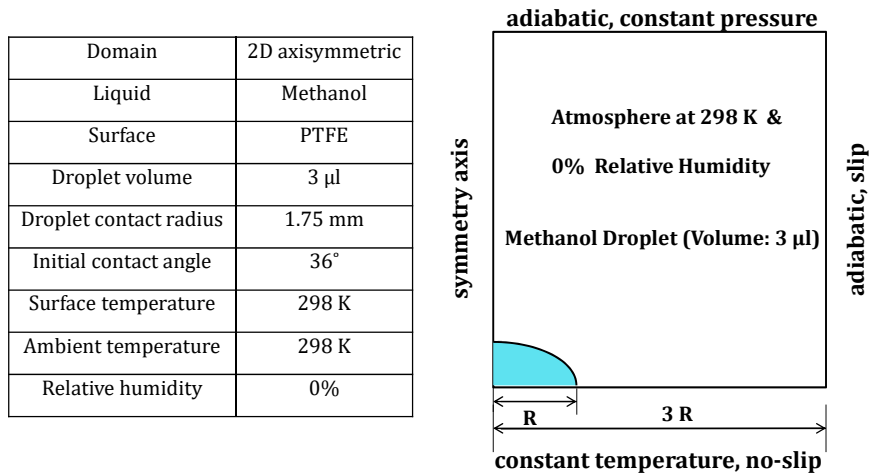


Fig. 5.1: Sessile droplet evaporation: Case details and numerical domain

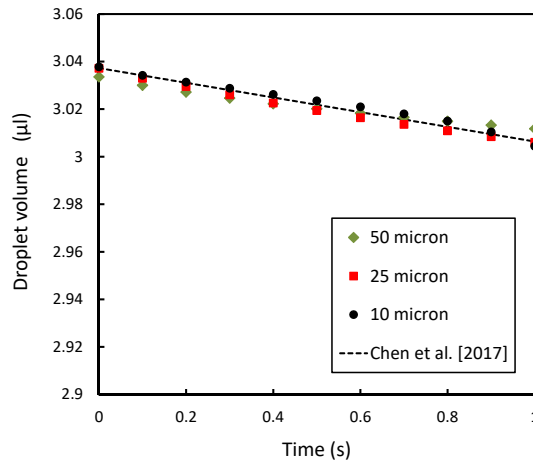


Fig. 5.2: Droplet volume versus time

The described case is simulated in a 2D-axisymmetric domain where three uniform grid sizes 50, 20 and 10 micron are used to check for the grid sensitivity. The details of the case and the domain are given in Figure 5.1. The droplet volume will decrease with time upon evaporation and it is driven by the concentration gradients being set up at the liquid-gas interface. Figure 5.2 shows a comparison of present numerical results with the experimental observations. It is observed that the volume at an instant is captured well with the present model and are in good agreement with the experimental values.

5.3.2 Single droplet impact over a heated surface

The in-house experimental observations made using the FC-72 droplet impingement over the heated Inconel surface are used to validate the numerical model. A droplet of 1.2 mm diameter is impinged over the heated surface with a impact velocity of 0.3132

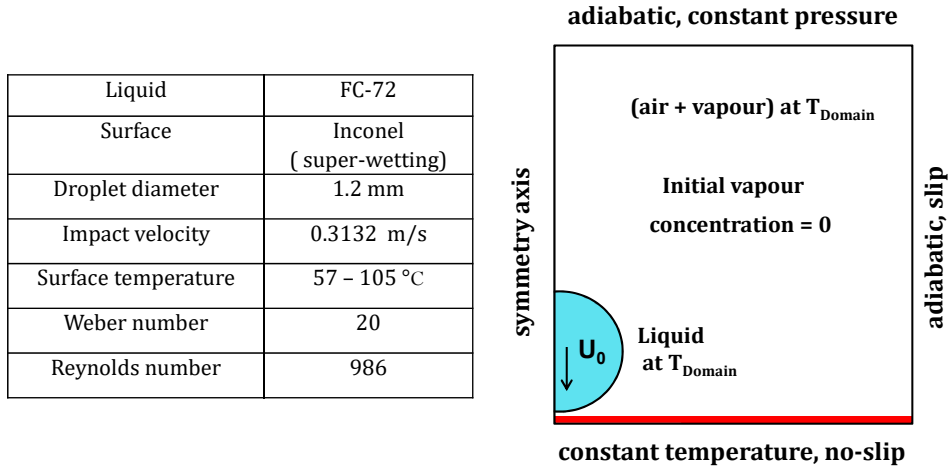


Fig. 5.3: Single droplet impact: Case details and numerical domain

m/s which corresponds to a Weber number of 20 and Reynolds number of 986. The surface temperature is the parameter and varied from 29 °C to (non-heated) to 105 °C (Dynamic Leidenfrost point). The ambient temperature is around 25 °C and initial ambient vapour concentration is taken as zero (FC-72 vapour). Figure 5.3 presents the case details and schematic of the numerical domain. A 2-D axisymmetric domain with 4 mm x 4 mm size is considered for the present simulation and at the wall, a constant temperature boundary condition is applied. The thermophysical properties of FC-72 liquid are presented in Table 3.1 (Chapter 3). As the domain size is small and physically very near to the surface, the temperature is higher than the surroundings and estimated to be equivalent to a average temperature T_m which is given as

$$T_m = \frac{T_\infty + T}{2} \quad (5.16)$$

Where T_∞ and T are the ambient and surface temperatures respectively. The droplet and the domain field temperature is patched at the following temperature conditions.

For $T_m < T_{sat}$

$$T_{Domain} = T_m \quad (5.17)$$

$T_m > T_{sat}$

$$T_{Domain} = T_{sat} \quad (5.18)$$

Grid independence study

To test the grid sensitivity, three sizes of uniform grid 4, 8 and 10-micron are considered. A single droplet impact over a heated surface with temperature of 70 °C is conducted. The outcomes of the droplet dynamics are measured in terms of maximum spread factor, dimensionless input and evaporation heat transfers as shown in Figures 5.4 a, 5.4 b and 5.5 respectively. The percentage deviation in the outcomes for 8 and 10-micron from the 4-micron case is presented in Table 5.2. From the analysis, the 8-micron is observed to be efficient in capturing the droplet dynamics with a reasonable computation load and time. Thus, the 8-micron uniform grid size is employed through out this numerical study.

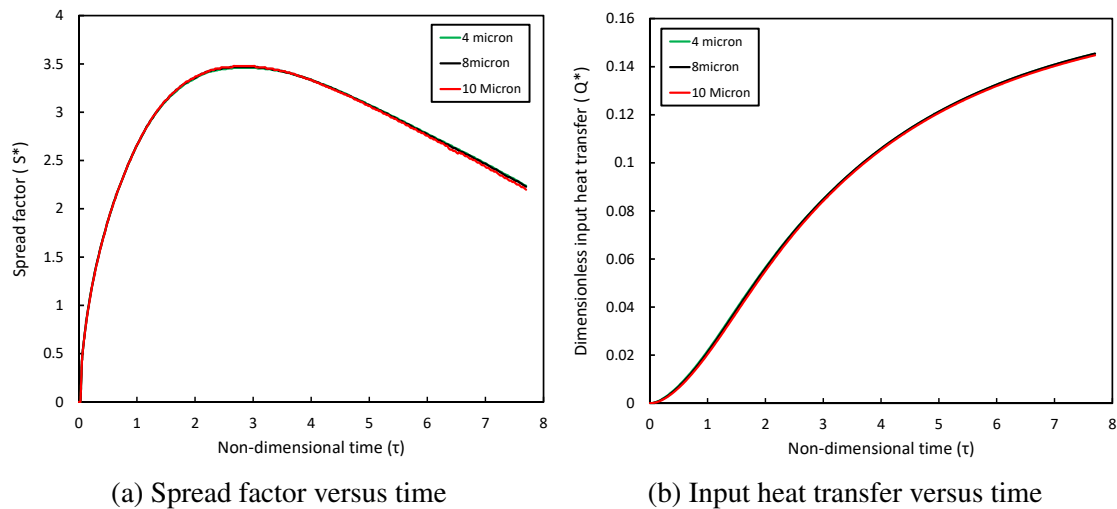


Fig. 5.4: Grid independence study: FC-72 droplet impact over the surface with temperature $T = 70$ °C

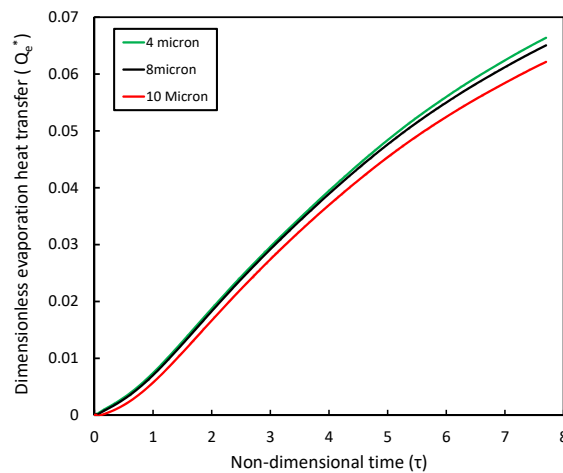


Fig. 5.5: Evaporation heat transfer versus time

Table 5.2: Grid independence study: Comparison of the outcomes with 4-micron grid size.

Cell size	Maximum spread	Input heat transfer	Evaporation heat transfer
8 micron	0.5 %	0.1 %	2 %
10 micron	0.4 %	0.5 %	6 %

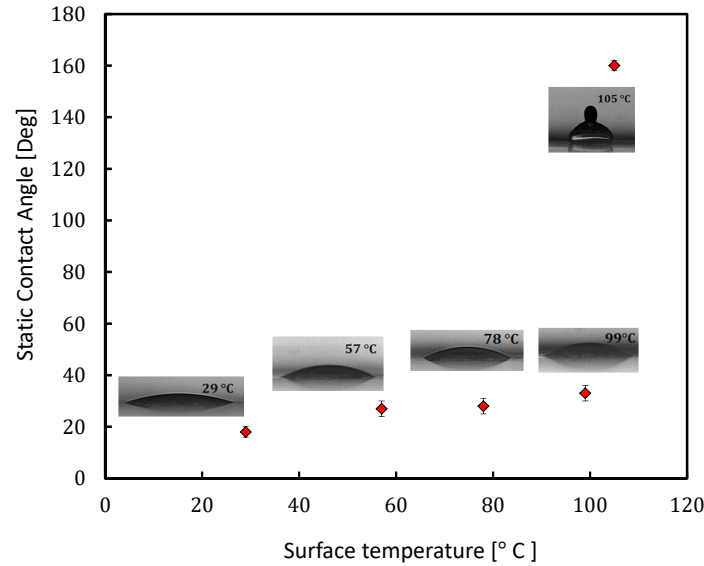


Fig. 5.6: Static contact angle versus temperature

Contact angle analysis

A special attention is given to treat the wall with appropriate contact angle so that the accurate spread dynamics is predicted. Two contact angle analysis are carried out, i.e., static and dynamic contact angle analysis.

During static contact angle analysis (SCA), the three-phase contact angle is measured from the high-speed images at the respective temperature and provided to the simulation. The technique, as explained in Chapter 4.2.2, is used to estimate the angle. Figure 5.6 shows the computed contact angles at different temperatures using the image post-processing. It is clear that the contact angle is increased with the temperature for the FC-72 droplet which is super-wetting ($\theta = 17^\circ$) on non-heated surface to a non-wetting ($\theta = 160^\circ$) spherical droplet at the Leidenfrost point.

For the dynamic contact angle analysis (DCA), contact line evaporation model explained in Chapter 3.3.1, is implemented. In this model, the contact angle dependence on contact line velocity and wall superheat is captured, and a regression curve is fitted to the data which is coupled to the governing equations. However, the

model is limited to the low wall superheat, where the spreading liquid displays a thin film and the generated data is sensitive to the nature of liquid-solid pair. Here, the FC-72 droplet is impinged upon Inconel surface has the super-wetting nature (at low wall superheat) and the required data to be used in contact line evaporation model is not available in the literature. So, the data employed for the FC-72 droplet impacted onto Chromium surface (super-wetting) is used in the current work.

The effect of these two contact angle models on the spread factor and input heat transfer is shown in Figure 5.7a and 5.7b respectively. The spread factor is over-estimated during the static contact angle analysis (SCA) and thereby resulted in over-prediction of the input heat transfer. It is evident that contact line evaporation model ensures the better prediction of droplet dynamics as it is accounting the effect of the contact line velocity and wall temperature on the contact angle. It is proposed that the contact line evaporation model is implemented for the low wall superheat conditions (where thin film condition is satisfied), and for a non-wetting situation, i.e., Leidenfrost point, a static contact angle is employed as the wall boundary condition.

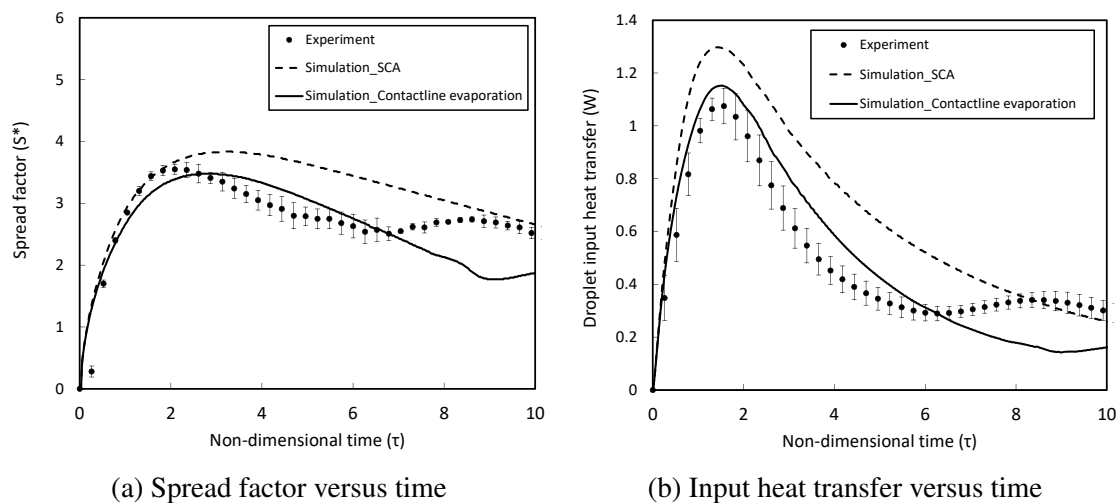


Fig. 5.7: Contact angle analysis: FC-72 droplet impact over the surface with temperature $T = 70\text{ }^{\circ}\text{C}$

Results and Discussion

Figures 5.8 and 5.9 show the comparison of the experiment and numerical simulation of droplet impact over the hot surface with temperature $T = 57\text{ }^{\circ}\text{C}$ and $105\text{ }^{\circ}\text{C}$ respectively. Weber number, $We = 20$ and Reynolds number, $Re = 986$ are maintained during the impingement. Contact line evaporation model is used for the case with $T = 57\text{ }^{\circ}\text{C}$

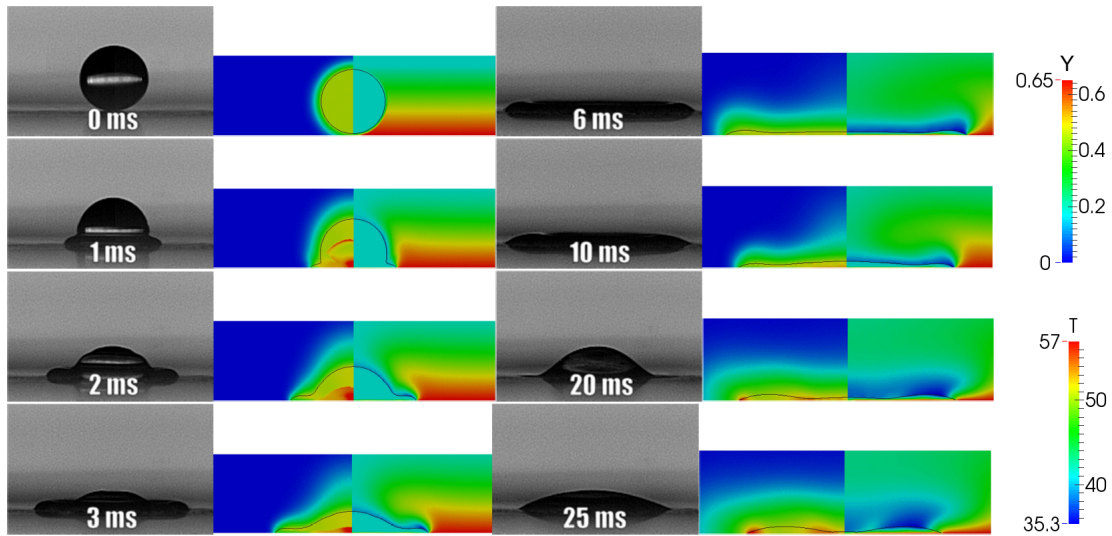


Fig. 5.8: Comparison of the experiment ($T = 57\text{ }^{\circ}\text{C}$, $We = 20$, $Re = 986$), and simulation with concentration (left) and temperature (right) contours

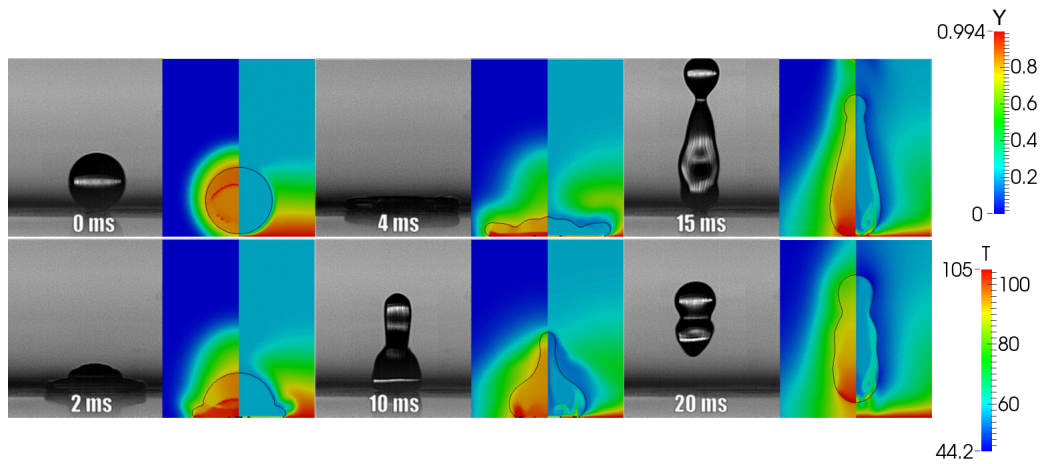


Fig. 5.9: Comparison of the experiment ($T = 105\text{ }^{\circ}\text{C}$, $We = 20$, $Re = 986$), and simulation with concentration (left) and temperature (right) contours

whereas for the impingement at $T = 105\text{ }^{\circ}\text{C}$, a static contact angle of value 160° is utilized.

As per the observations from the simulation as shown in Figure 5.8, the spread dynamics of the droplet is reproduced well during the advancing and receding phases. But, as shown in Figure 5.10a, there are minor discrepancies in predicting cycle time because of experimental conditions such as surface non-homogeneity, which are not taken into account during the numerical study. Nonetheless, the overall performance of the model in estimating the heat transfer is good as presented in Figure 5.10b. Similarly, for the case of droplet impact at $T = 105\text{ }^{\circ}\text{C}$ (Dynamic Leidenfrost Point), the dynamics such as the spreading droplet profiles, the Lift-off time, and satellite droplet generation

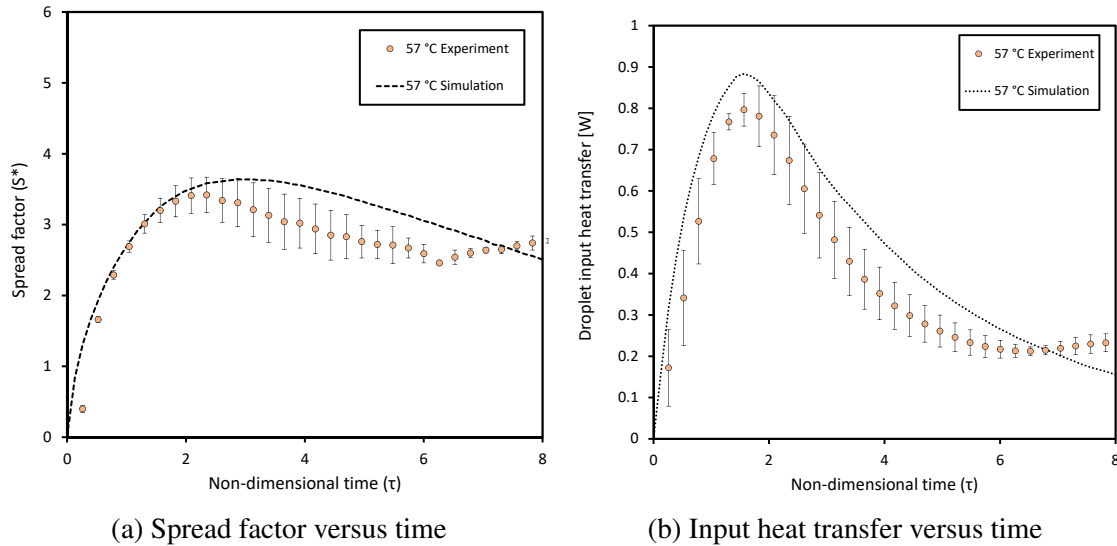


Fig. 5.10: FC-72 droplet impingement over the heated surface ($T = 57\text{ }^{\circ}\text{C}$, $We = 20$, $Re = 986$)

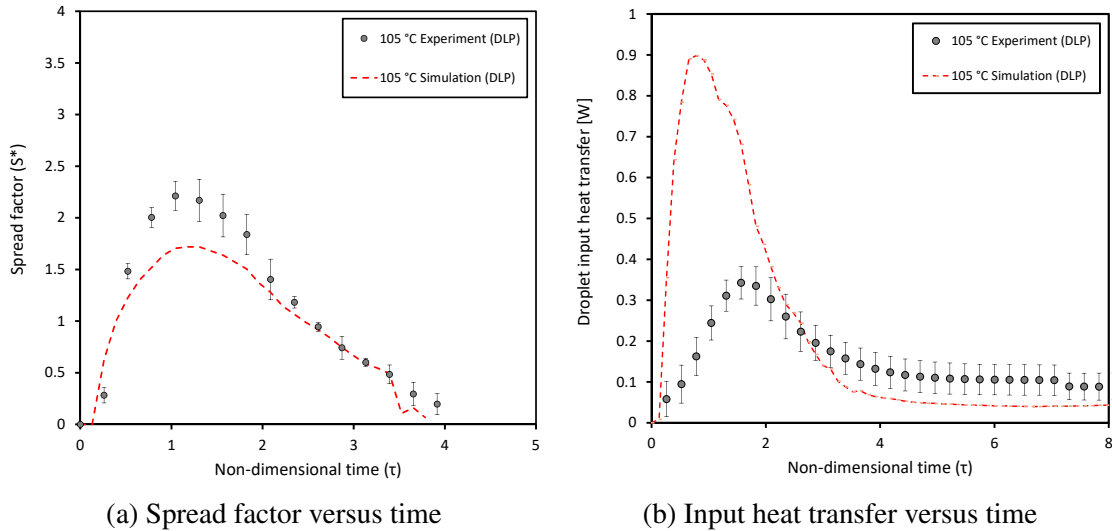


Fig. 5.11: FC-72 droplet impingement over the heated surface ($T = 105\text{ }^{\circ}\text{C}$, $We = 20$, $Re = 986$)

(Figure 5.9 at time = 15 ms) are captured by the numerical model. Figures 5.11a and 5.11b present the spread and heat transfer behaviour during the impact at Leidenfrost point ($T = 105\text{ }^{\circ}\text{C}$). A reasonable prediction of spread and heat transfer is achieved during the simulation. The deviation in heat transfer prediction is due to the inaccurate vapour thickness realised during the simulation. At Leidenfrost temperature, the vapour layer formed reduces the heat being conducted into the droplet. The model under-predicts the vapour layer thickness which resulted in high input heat transfer rates. More studies in future need to be carried out to over the problem with an emphasis on wall boundary condition and high grid resolution with minimum computation load.

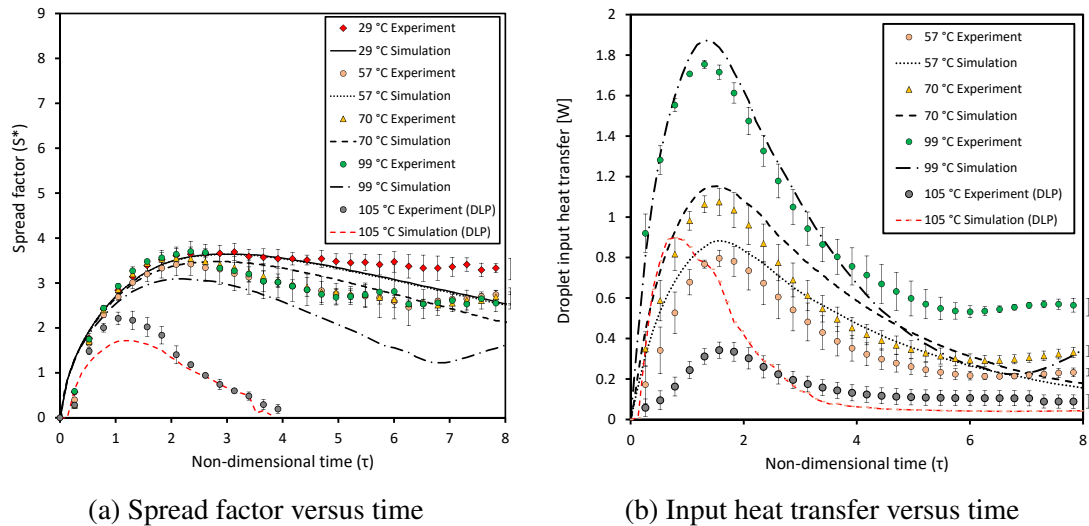


Fig. 5.12: FC-72 droplet impingement over the heated surface ($We = 20$, $Re = 986$)

Figure 5.12a and 5.12b shows the comparison of spread factor and corresponding input heat transfer obtained during simulations with experimental observations at all surface temperatures. The performance of the model is satisfactory and the intriguing details of the impact dynamics are captured well during the numerical analysis.

5.3.3 Parametric study: Two consecutively impinging droplets at different time intervals over a hot surface

In chapter 4, an experimental investigation of the train of two droplets are conducted, and the flow rate maintained is around 20-60 droplets per minute (DPM). Thus the time interval maintained between the droplets is about 1 to 3 seconds. By this time, the leading droplet becomes sessile and cools the surface, which results in a reduction of the heat transfer during the trailing droplet impingement over this sessile droplet. There is a need to study the interaction of two droplets when they are both in motion. Thus, the spread dynamics will get affected, resulting in different droplet heat transfer phenomena. It can be accomplished at high droplet flow rates where the time interval between the droplets should be the order of milliseconds. In experiments, handling such a flow rate with a homogeneous droplet volume is not possible and out of reach with the adopted methodology. Therefore a numerical investigation is implemented to perform the proposed analysis. In this section, the consecutively impinging droplets over a hot surface are numerically simulated. Here the maintained time intervals are of an order of spreading cycle time which is milliseconds (droplet flow rate = 10^4 to 10^5 DPM).

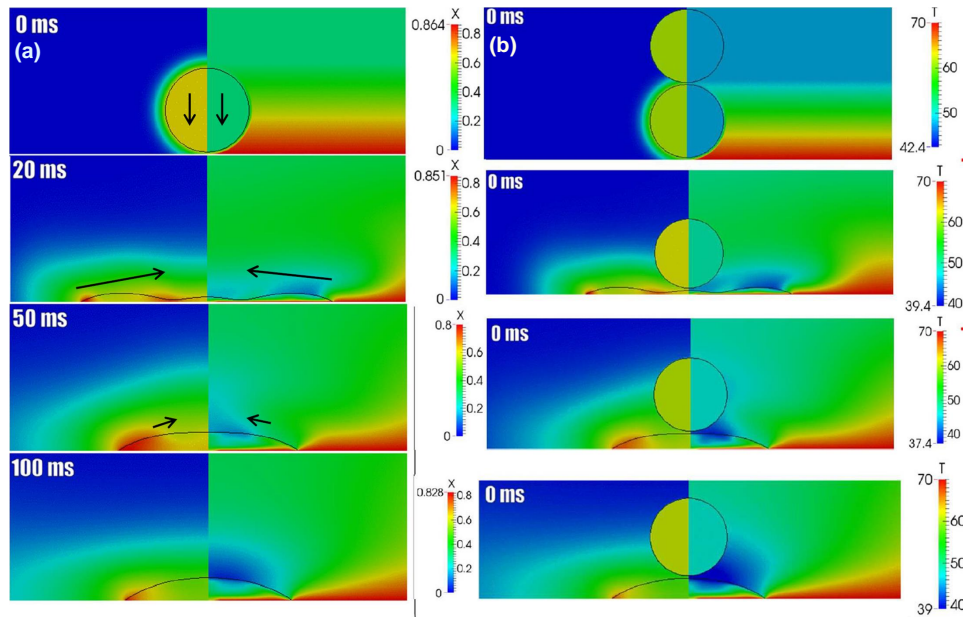


Fig. 5.13: Parametric study : (a) Different instants of single droplet impact ($T = 70$ °C, $We = 20$, $Re = 986$) (b) Consecutively impinging droplets (Drop-on-drop impact) at these instants

The aim is to study the effect of leading droplet's phase, i.e., advancing or receding phase on spread and heat transfer characteristics during the drop-on-drop impact. In this study, the cooling effect by the first droplet is neglected by imposing a constant temperature boundary condition (which is far from the actual experimental condition). This enables us to recognise the sole effect of initial droplet's velocity direction on spread hydrodynamics and corresponding heat transfer qualitatively. A case with single droplet of FC-72 liquid with the diameter of 1.2 mm and impacting velocity of 0.3132 m/s is selected. The pre-impacting conditions of the impingement are with a surface temperature $T = 70$ °C, Weber number $We = 20$ and Reynolds number $Re = 986$. As shown in Figure 5.13, four time instants, $t = 0, 20, 50,$ and 100 ms (millisecond), of the impinged leading droplet are chosen and the trailing droplet is made to impact on it. The case details and the numerical domain considered in the study are presented in Figure 5.14. A uniform grid size of 8-micron is considered in the simulation and a constant temperature condition is imposed on the wall. The domain temperature is initiated with a mean temperature $T_m = 47.5$ °C calculated as per the equation 5.16, and a corresponding vapour concentration is computed from the Wagner equation. The contact angle hysteresis is handled by including the contact line evaporation model during the numerical analysis.

Liquid	FC-72
Surface	Inconel (super-wetting)
Droplet diameter	1.2 mm
Impact velocity	0.3132 m/s
Surface temperature	70 °C
Domain temperature	47.5 °C
Weber number	20
Reynolds number	986

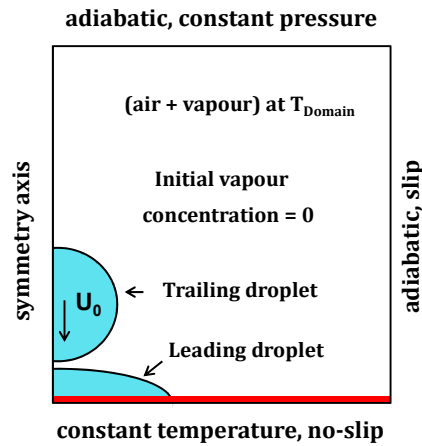


Fig. 5.14: Parametric study : Case details and the numerical domain

Results and Discussion

The effect of leading droplet's phase on overall impact dynamics is taking the four instants, as shown in Figure 5.13a, where at $t = 0$ ms, the droplet is about the impact which is said to be at the beginning of advancing (spreading) phase. At this stage, it is associated with a high velocity, which aids in the spreading of the droplet over the surface. At the time, $t = 20$ ms, the droplet completes the spreading and starts to retract back with a velocity resulted from the combined effects of capillary and viscous forces. The third instant is at $t = 50$ ms, where it is in the second cycle of receding and is about to become a sessile droplet. Finally, at the time, $t = 100$ ms, the droplet settles down to become a static droplet.

Figure 5.15 shows the drop-on-drop impingement behaviour for the collision at the time, $t = 0$ ms, where both the trailing and leading droplets are in an advancing stage, and their velocities complements each other's spreading. It leads to an enhancement in the maximum spread diameter during the impingement, thereby increased the input heat transfer. In the case of drop-on-drop impact at the time, $t = 20$ ms, the leading droplet is in opposite direction to the impacting droplet as shown in Figure 5.16. Eventually, the total liquid spreads with a low velocity ensuing a decrease in maximum spread diameter and heat transfer.

Figures 5.17 and 5.18 compares the simulated cases in terms of spread factor, STV, dimensionless input and evaporation heat transfers. It is noted that the presented outcomes are for the drop-on-drop impact (trailing droplet impact onto leading droplet) and compared to a isolated (single) droplet at the same impact conditions. It is

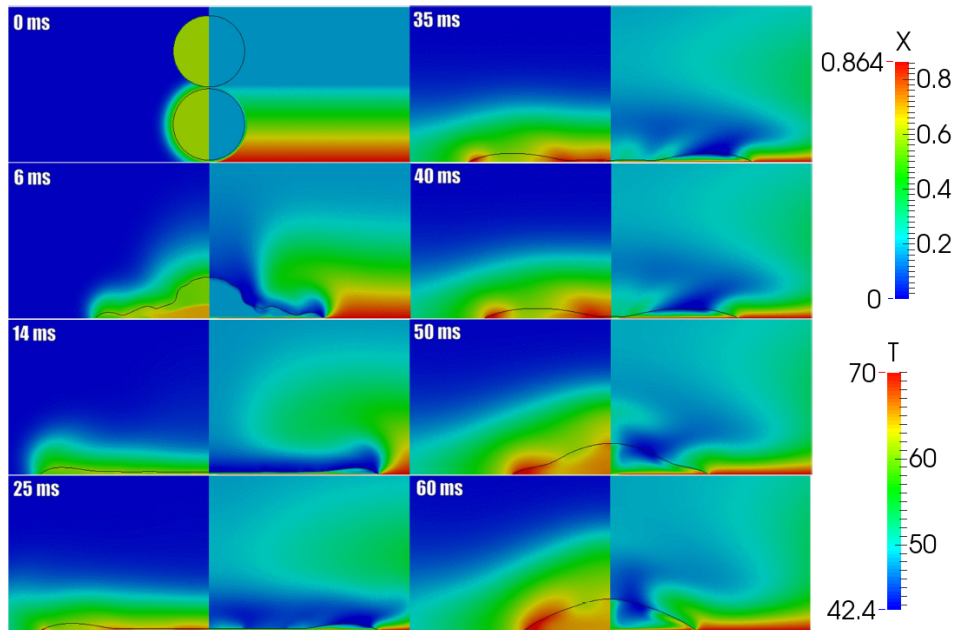


Fig. 5.15: Drop-on-drop impact with time interval of 0 ms, $T = 70\text{ }^{\circ}\text{C}$, $We = 20$, $Re = 986$: Contours of concentration (left) and temperature (right)

revealed that the leading droplet velocity and its direction (advancing or receding phase) has a prominent role in altering the spread dynamics of the impingement which influences the droplet heat transfer. As shown in Figure 5.17a, the dynamics with a high and low spread factors are registered when drop-on-drop impact is carried at the time instants of, $t = 0\text{ ms}$ and 20 ms respectively. And the intermediate values are exhibited during the impingements at the time, $t = 50$ and 100 ms , where the leading droplet is almost a static liquid film. It is interesting to find that the drop-on-drop heat transfers are more than the single droplet impingement contrary to their behaviour at low flow rates as discussed in Chapter 4. For the droplet flow rates of the order of 100 DPM (Chapter 4), the leading droplet has sufficient time to cool the surface and reducing the surface mean temperature, while for the high flow rates, the droplets are interacting with each other in their initial stage of impingement. Figures 5.17b and 5.18a is showing the dimensionless input and evaporation heat transfers of the drop-on-drop impact compared with the single droplet impact. It is understand that the heat transfer characteristics are highly influenced by the spread factors when the both the droplets are in motion. Once the droplet becomes static, the surface area-to volume ratio, i.e., the film thickness of the droplet dictates the input heat flow which is evident for the cases at the time instants $t = 50$ and 100 ms , as shown in Figure 5.18b.

The cumulative input and evaporation heat transfers for the drop-on-drop impact

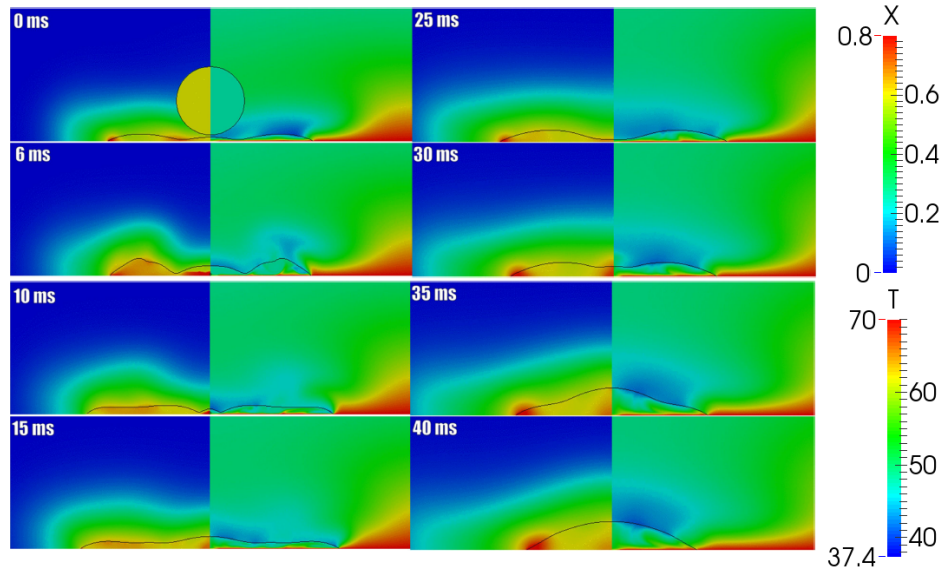


Fig. 5.16: Drop-on-drop impact with time interval of 20 ms, $T = 70\text{ }^{\circ}\text{C}$, $We = 20$, $Re = 986$: Contours of concentration (left) and temperature (right)

Table 5.3: Summary of the constants and other conditions used in the analytical model

S.No	Study	Liquid	Surface	Time interval between droplets (s)	Wall boundary condition	Spread factor used in eq.4.32	Constant a	Constant b
1	Numerical I	FC-72	Chromium (super-wetting)	Not considered	Constant temperature	Maximum spread factor	2.67	3.4
2	Experiemental I	Water	Inconel (wetting)	3	Constant temperature (with heat generation)	Maximum net-spread factor	15	1
3	Experiemental II	FC-72	Inconel (super-wetting)	1	Constant temperature (with heat generation)	Maximum net-spread factor	2.67	0.5
4	Numerical II	FC-72	Chromium/ Inconel (super-wetting)	0.001 to 0.1	Constant temperature	Maximum spread factor	2.67	0.5

at different time intervals and their comparison with single droplet are presented in Figure 5.19. It emphasizes that for a drop-on-drop (for trailing/second droplet) impact with a time intervals of the order of spread-cycle (milliseconds) will always exhibit higher heat transfers than the single droplet impact. They are governed by the leading droplet phase and resultant film thickness (STV). The effectiveness ratio ϵ , which is the ratio of cumulative input heat transfer during drop-on-drop impact to the single droplet impact, is calculated for the investigated cases and shown in the Figure 5.20. It manifests that the heat transfer during the drop-on-drop impact is higher than the single droplet impact and strongly dependent on the leading droplet velocity and the phase. A high effectiveness ratio is recorded when the leading droplet is in advancing phase and it is low in the case of droplet impact in receding phase.

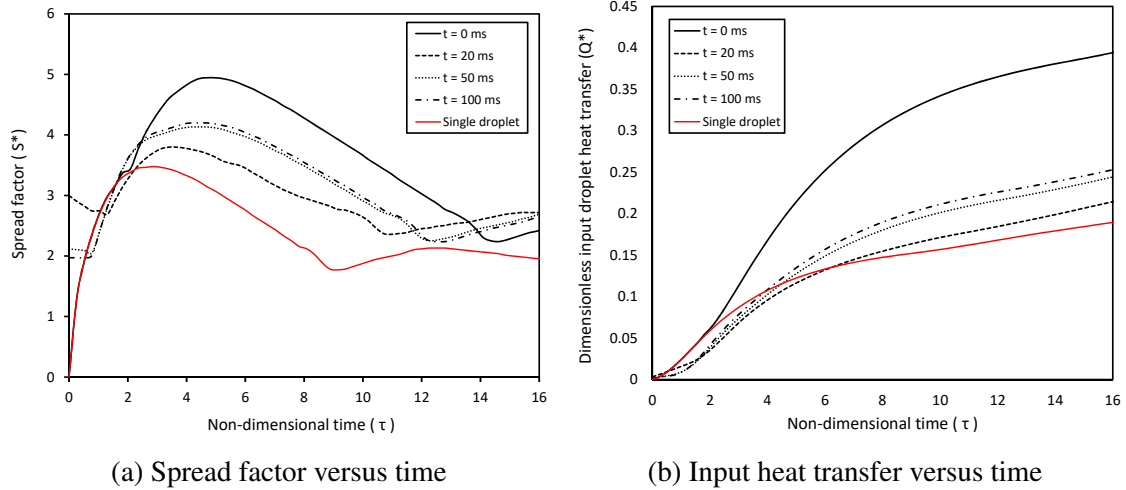


Fig. 5.17: Parametric study of Drop-on-drop impact over the surface with temperature $T = 70\text{ }^{\circ}\text{C}$, $We = 20$, $Re = 986$: Spread factor and input heat transfer variation with time

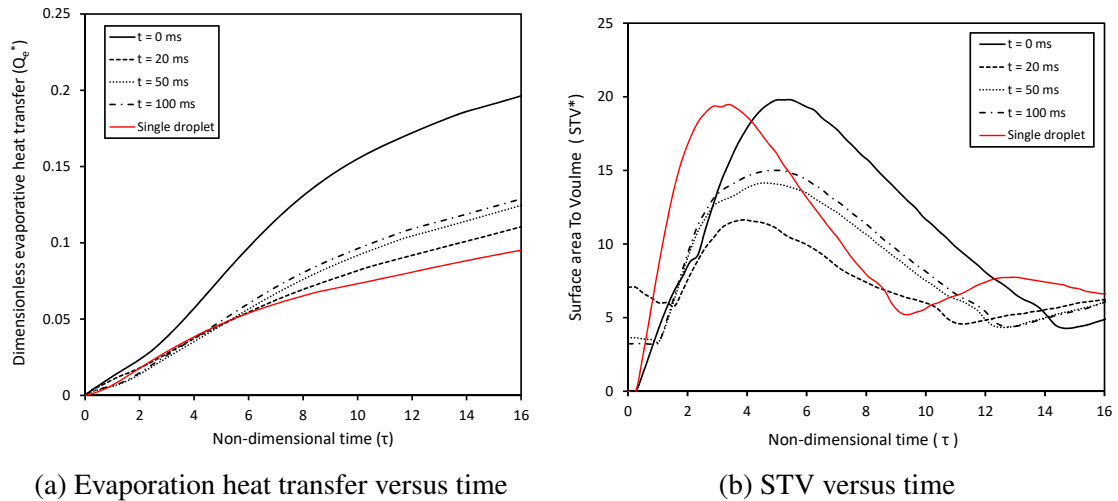


Fig. 5.18: Parametric study of Drop-on-drop impact over the surface with temperature $T = 70\text{ }^{\circ}\text{C}$, $We = 20$, $Re = 986$: Evaporation heat transfer and STV variation with time

5.3.4 Analytical modelling

Using the proposed analytical models for the maximum spread factor and effectiveness, the calculated theoretical values are compared with experimental data as shown in Figure 5.21. The values $a = 2.67$ and $b = 0.5$ are used in the equations 4.20, 4.22 and 4.32.

The correlation for the maximum spread factor showed a better prediction of numerical results. In contrast, a considerable deviation is observed in estimation of effectiveness for the cases with time interval $t = 0$ and $t = 20$ milliseconds. Upon

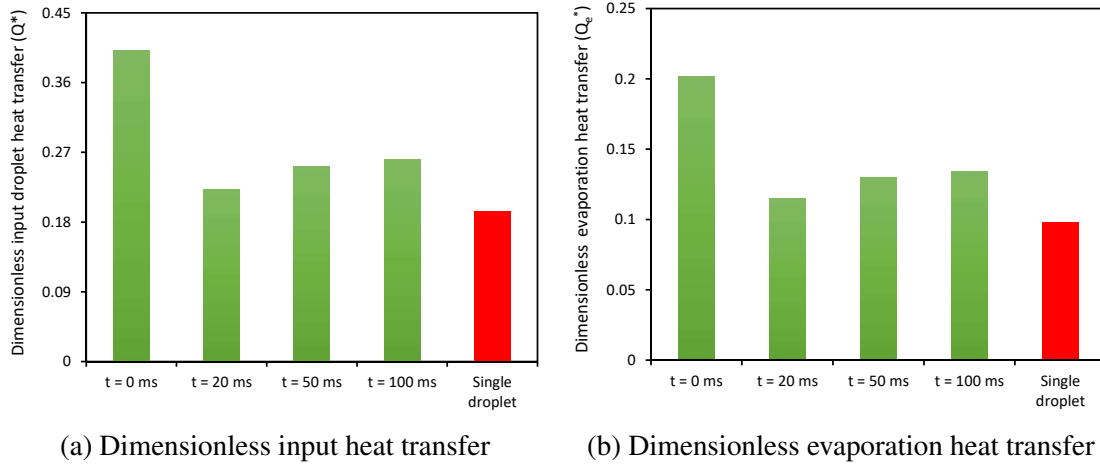


Fig. 5.19: Parametric study of Drop-on-drop impact over the surface with temperature $T = 70\text{ }^\circ\text{C}$, $We = 20$, $Re = 986$: Dimensionless input and evaporation heat transfer variation with time

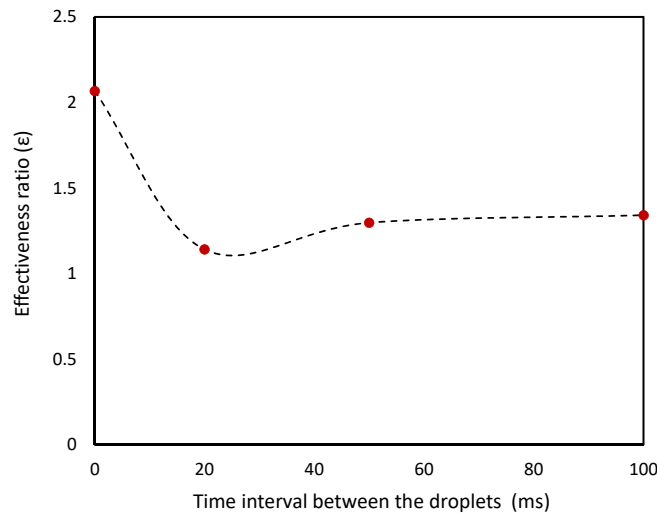


Fig. 5.20: Parametric study: Effectiveness ratio

analysis, it is realised that the value of ' b ' is sensitive to the flow rate and limits the applicability of the model. A summary of constants ' a ' and ' b ' through out the studies are provided in Table 5.3. From this overview, it is understood that the proposed models require the values to be evaluated for a given system of liquid-surface, heating conditions, and flow rate. However, with the knowledge of the constants ' a ' and ' b ', models are able to provide better estimates of maximum spread and heat transfer.

5.3.5 Closure

In this chapter, a numerical model is implemented to study the dynamics of two consecutively impinging droplets over a hot surface in the air-vapour medium. The

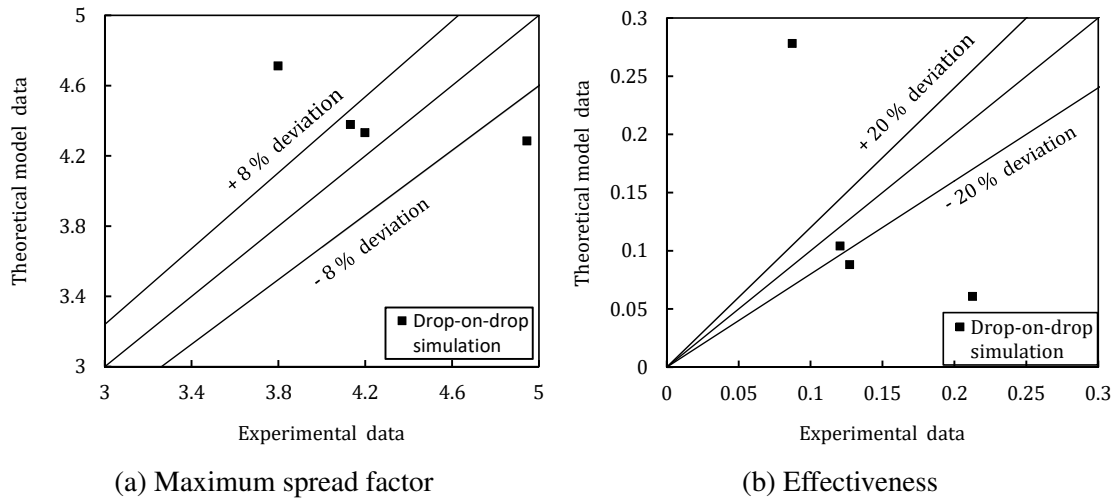


Fig. 5.21: Experimental versus theoretical

mathematical formulation, validation of the model using sessile droplet evaporation and single droplet impingement, are discussed. In the end, a parametric study is conducted to realise the effect of the time interval between the droplets on the outcomes of the impact dynamics. In the next chapter, the conclusions of the present studies and the scope of future work are presented.

CHAPTER 6

CONCLUSIONS AND SCOPE FOR FUTURE WORK

6.1 Introduction

The present work focusses on the experimental and numerical investigation of multiple droplet impingement over a heated surface. One of the interesting and significant configurations of multiple droplet interaction is the consecutive impingement of a train of droplets. For the analysis, the initial two droplets of the droplet train are considered, and the spread and heat transfer characteristics of each droplet impact is studied as two separate scenarios as a single droplet and drop-on-drop impingement.

6.1.1 Numerical study: Droplet impact over a heated surface in vapour medium

The preliminary numerical simulations are conducted using a phase change solver implemented in open-source CFD toolbox OpenFOAM with the VOF interface capturing technique. These initial studies are aimed at understanding the spread and heat transfer dynamics for a single droplet and drop-on-drop impact over a hot surface in a vapour medium. The cooling effect of the leading droplet (sessile droplet) is neglected by simultaneously activating the droplet falling and the surface heating. Thus, the dynamics of a single droplet interacting with a dry and wetted hot surface is captured with the study. Different phases involved during the single droplet and drop-on-drop impact are presented. Influential parameters such as Weber number (We), Bond number (Bo), Jakob number (Ja), and the radius ratio (R^*) affecting the drop-on-drop impingement are identified, and a parametric study is carried out. In the end, analytical models predicting maximum spread and droplet heat transfer during a single droplet impact are extended to drop-on-drop impingement. The conclusions of the study can be summarized as follows.

1. It is observed that under same impact conditions, drop-on-drop configuration exhibits a high spread factor compared to single drop impingement. However, the maximum of the net spread factor (δS^*), and large heat transfer rates are observed for the single drop case as it is associated with high spread surface area to volume ratio i.e., low thermal resistance.
2. In order to study the effect of Weber number, three cases were taken where all other dimensionless parameters are maintained constant. This research showed that a larger Weber number (within splashing limit) case have high spread factor and cycle durations which favours better heat transfer rates.
3. The influence of wall superheat in terms of Jakob number(Ja) and gravitational effects using Bond number (Bo) were analyzed. As expected, the rise in Jakob number increases the heat transfer and promotes the evaporation process. Consequently, the corresponding spread factor and cycle periods are reduced.
4. A similar trend was observed during the change of Bond number. A hyper gravity case (High Bo) increases the spread which allows more heat to transfer into droplet and enhances the evaporation rate. Thus spread dynamics induces better heat transfer rates.
5. Simulations were also carried out by varying the diameter of the sessile droplet i.e., the radius ratio (R^*), to investigate its influence on the evaporation process. It was found that the coalescing effect increases for large diameter case, which hinders the overall spread factor. Furthermore, the rate of heat transfer is affected due to the high thermal resistance.
6. An analytical model is developed to find the maximum spread factor using conservation of energy principle. The Nusselt number based correlation available in the literature, was used to estimate the total input heat transfer. Better predictions of maximum spread and heat flow during the spreading phase are obtained using the developed analytical model.

6.1.2 Experimental study: Droplet impact over a heated surface in air-vapour medium

With the inputs from the preliminary simulations, an experimental investigation of train of two droplets are conducted. The initial studies are performed using Deionised water followed by FC-72 liquid droplet impingement.

Water droplet impingement

At constant impact conditions ($We = 50$, $Re = 3180$), and flow rate of 20 droplets per minute (DPM), the behaviour is captured by high-speed imaging and infrared thermography. Deionized water droplets are impinged over the heated Inconel surface, and the surface temperature is chosen as a parameter, and varied from 22 °C (non-heated) to 175 °C. The impingement scenario is classified as single droplet and drop-on-drop configurations over the hot surface and compared for relevant parameters. Outcomes such as spread factor, droplet input heat transfer, surface temperatures, effectiveness or cooling efficiency, and dynamic contact angle are obtained and compared. The following conclusions are made from the study.

1. The effect of temperature on spread dynamics is dominant from the initial cycle of spreading for both configurations. However, the maximum spread factor trends indicate that the spread factor is significantly affected by surface temperature during single droplet impingement compared to drop-on-drop impact.
2. High heat transfer rates are observed in the vicinity of the three-phase contact line, and input heat transfer rates are strongly influenced by the surface temperature during single droplet, as well as drop-on-drop impact over the surface.
3. Comparison of droplet input heat transfer between the configurations confirms that there is a reduction in the trailing droplet heat transfer, during drop-on-drop collision, compared to the leading droplet. The pre-cooling due to sessile droplet

(initial) interaction and decrease in surface area-to-volume ratio is attributed to the low heat transfer rates observed during the drop-on-drop impact.

4. The extent of surface area being cooled has increased during drop-on-drop impingement, and the region corresponds to the *net spread factor* i.e., the annulus portion between the initial and post-impact spread is found to provide effective heat transfer during the impingement.
5. The dynamic contact angle variation is provided, for different surface temperatures, and the effect of temperature on contact angle is weak for both the configurations. Also, there is only a marginal increase of static contact angle over the heated surface due to the non-volatility of water.
6. To compare the input heat transfer rates among the configurations, an effectiveness ratio is defined as the ratio of dimensionless input heat transfer during drop-on-drop impact to a single droplet impingement. This parameter was found to be constant (around 0.62) for all surface temperatures concluding the reduction in heat transfer during drop-on-drop impact.
7. Relevant analytical models available in literature were identified, and used to predict the maximum spread factor and heat transfer rates during the spreading phase for the present impingement configurations. The models captured the spread and heat transfer dynamics with a deviation of 8 % and 20 %, respectively.

FC-72 droplet impingement

A millimeter-sized FC-72 droplet stream is impacted at a constant impact conditions ($We = 20$ and $Re = 986$) and a flow rate of 60 DPM (droplets per minute) over a thin heater foil. Surface temperature is chosen as a parameter, and droplet-train interaction is studied by considering the initial two droplets of the stream. The configurations, i.e., single and drop-on-drop impingement, are investigated using high-speed photography and infrared thermography. Spread dynamics and heat flux distributions over the

surface are realized during the single and drop-on-drop impingement. The Dynamic Leidenfrost temperature for the impact conditions is identified, and the heat transfer characteristics are studied up to the Leidenfrost temperature. The following conclusions are drawn from the study.

1. Experimental observations revealed that the surface temperature has a considerable effect on spread factor during both the configurations and the droplet heat transfer increases with a rise in surface temperature.
2. The comparison shows that the droplet input heat transfer is reduced for drop-on-drop impact compared to single droplet impingement. Increased thermal resistance and decrease in the surface mean temperature due to the sessile droplet presence is resulted in the decrease of heat transfer.
3. A boiling curve is approximated, and regimes are classified based on the input heat transfer values. An effectiveness ratio is defined to quantify the droplet heat transfer reduction during the drop-on-drop impingement. It is found that the effectiveness ratio is nearly constant, around 0.6 at all considered temperatures and boiling regimes.

6.1.3 Numerical study: Droplet impact over a heated surface in air-vapour medium

A numerical model is implemented to simulate the droplet impact over a heated surface in air-vapour medium (multi-component system). The two-phase solver is implemented in OpenFOAM with the VOF interface capturing technique, and the evaporation of the droplet is computed based on the concentration gradients at the interface. The model is validated using a sessile droplet evaporation case, and the present experimental observations of single droplet impingement. A contact angle analysis is carried out to examine the effect on spread and heat transfer dynamics during the impingement. Later on, a parametric study of two consecutively impinging droplets over a hot surface is performed by varying the time interval between the

droplets, which is the order of spread-cycle time (milliseconds). The following conclusions are made from the study.

1. A static contact angle and the contact line evaporation model (Dynamic contact angle) are employed in the simulation. Results show that the static contact angle model over-predicted the spread factor and the corresponding heat transfer, whereas the contact line evaporation model produced a better estimation of the droplet dynamics.
2. During the drop-on-drop impingement with different time intervals between the droplets, a high droplet heat transfer is observed when the leading droplet is in the advancing phase. At the same time, a low value is observed when it is in the receding phase.
3. The phase and the velocity of the leading droplet alters the spread dynamics and thereby the droplet heat transfer.
4. When the time interval between the droplets is of the order of spread-cycle time (milliseconds), the heat transfer during trailing droplet impact is always higher than the leading droplet (single droplet).

6.2 Major conclusions of the present study

1. During the drop-on-drop impingement, three phases are identified, namely coalescing, advancing, and receding phases. The spread and heat transfer characteristics of the drop-on-drop impact over a hot surface firmly depend on parameters such as impacting velocity (Weber number), surface temperature (Jakob number), the sessile droplet radius (radius ratio) and the surrounding medium (air/vapour). The maximum spread diameter and film thickness (STV) are significant outcomes of the impingement process, which dictates the droplet input and evaporation heat transfer.

2. In the case of two consecutively impinging droplets over the heated surface, the heat transfer during each droplet interaction is inspected. It is found that during the heat transfer during the trailing droplet impact is affected by the parameters such as Weber number (We), surface temperature, and droplet flow rate (time interval between the droplets).
3. High Weber number increases the maximum spread factor and also the net spread factor during the trailing droplet impact (drop-on-drop), which aids in increasing the droplet heat transfer.
4. The increase in surface temperature results in high heat transfer into a droplet, and it ensues rapid droplet evaporation affecting the spread dynamics.
5. When the droplet flow rate is of the order of 100 DPM (time interval in seconds), there is an increase in surface cooling by the leading droplet by reducing the surface mean temperature. Thus, the trailing droplet heat transfer is low and found to be constant in all boiling regimes.
6. When the droplet flow rate is of the order of $10^4 - 10^5$ DPM (time interval in milliseconds), the two droplets found to be interacting at the early stages of their spread-cycle. Thus, the trailing droplet heat transfer is higher than a single droplet and controlled by the phase (advancing or receding) and the velocity of the leading droplet.
7. The implemented analytical models for predicting the maximum spread factor and droplet heat transfer are efficient in capturing the dynamics with reference to the experimental and numerical investigations of droplet impingement.

6.3 Suggestions for future work

The motivation of the present work is to understand the underlying physics of the spray cooling process. Within the scope of this work, the spread and heat transfer dynamics of drop-on-drop impact is studied. It is required to investigate the other configurations of

spray cooling to develop more analytical and numerical resources to predict the process. The following are the few suggestions for future work.

1. The implemented numerical model has to be extended by including the heat condition effects in the solid to provide more insights into the phenomena.
2. The present study of drop-on-drop impact can be conducted using different range of liquids such as heterogeneous mixtures and nanofluids.
3. Configurations such as simultaneous and droplets impinging with variable off-set distance over a hot surface can be studied. Observations made from the single and drop-on-drop impacts can be compared to understand the heat transfer during the droplet stream impingement.
4. Numerical investigation into phenomena of boiling in the multiple droplet configurations, such as simultaneous droplets, can be an interesting study.
5. Experimental studies of multiple droplet impact with variable surface wettabilities is a topic of interest in many industrial applications. Also, studies of droplet impingement over complex surfaces such as micro and nanostructures provide greater scope for future work.

6.4 Closure

In this chapter, the summary of each numerical and experimental analysis with an individual conclusion is provided. In the end, the major conclusions of the overall study and scope for future work are presented.

REFERENCES

1. **Arnaldo del Cerro, D., I. G. Marín, G. R. B. E. Römer, B. Pathiraj, D. Lohse, and A. J. Huis in 't Veld** (2012). Leidenfrost point reduction on micropatterned metallic surfaces. *Langmuir*, **28**(42), 15106–15110.
2. **Avedisian, C. and J. Koplik** (1987). Leidenfrost boiling of methanol droplets on hot porous/ceramic surfaces. *International Journal of Heat and Mass Transfer*, **30**(2), 379 – 393. ISSN 0017-9310.
3. **Batzdorf, S.** (2015). *Heat transfer and evaporation during single drop impingement onto a superheated wall*. Ph.D. thesis, Technische Universität.
4. **Batzdorf, S., J. Breitenbach, C. Schlawitschek, I. V. Roisman, C. Tropea, P. Stephan, and T. Gambaryan-Roisman** (2017). Heat transfer during simultaneous impact of two drops onto a hot solid substrate. *International Journal of Heat and Mass Transfer*, **113**, 898 – 907. ISSN 0017-9310.
5. **Berberović, E., I. V. Roisman, S. Jakirlić, and C. Tropea** (2011). Inertia dominated flow and heat transfer in liquid drop spreading on a hot substrate. *International Journal of Heat and Fluid Flow*, **32**(4), 785 – 795. ISSN 0142-727X.
6. **Bernardin, J. and I. Mudawar** (1999). The Leidenfrost point: experimental study and assessment of existing models. *Journal of Heat Transfer*, **121**(4), 894–903.
7. **Bernardin, J. D. and I. Mudawar** (1997). Film boiling heat transfer of droplet streams and sprays. *International Journal of Heat and Mass Transfer*, **40**(11), 2579–2593.
8. **Bernardin, J. D. and I. Mudawar** (2002). A cavity activation and bubble growth model of the leidenfrost point. *Journal of Heat Transfer*, **124**(5), 864–874.
9. **Bernardin, J. D., C. J. Stebbins, and I. Mudawar** (1996). Effects of surface roughness on water droplet impact history and heat transfer regimes. *International Journal of Heat and Mass Transfer*, **40**(1), 73 – 88. ISSN 0017-9310.
10. **Bernardin, J. D., C. J. Stebbins, and I. Mudawar** (1997). Mapping of impact and heat transfer regimes of water drops impinging on a polished surface. *International Journal of Heat and Mass Transfer*, **40**(2), 247 – 267. ISSN 0017-9310.
11. **Bertola, V. and K. Sefiane** (2005). Controlling secondary atomization during drop impact on hot surfaces by polymer additives. *Physics of Fluids*, **17**(10), 108104.
12. **Brackbill, J., D. B. Kothe, and C. Zemach** (1992). A continuum method for modeling surface tension. *Journal of computational physics*, **100**(2), 335–354.
13. **Breitenbach, J., I. V. Roisman, and C. Tropea** (2018). From drop impact physics to spray cooling models: a critical review. *Experiments in Fluids*, **59**(3), 55. ISSN 1432-1114.

14. **Bussmann, M., J. Mostaghimi, and S. Chandra** (1999). On a three-dimensional volume tracking model of droplet impact. *Physics of Fluids*, **11**(6), 1406–1417.
15. **Celata, G. P., M. Cumo, A. Mariani, and G. Zummo** (2006). Visualization of the impact of water drops on a hot surface: effect of drop velocity and surface inclination. *Heat and Mass Transfer*, **42**(10), 885. ISSN 1432-1181.
16. **Celestini, F., T. Frisch, and Y. Pomeau** (2013). Room temperature water Leidenfrost droplets. *Soft Matter*, **9**, 9535–9538.
17. **Chandra, S. and C. Avedisian** (1991). On the collision of a droplet with a solid surface. *Proc. R. Soc. Lond. A*, **432**(1884), 13–41.
18. **Chandra, S., M. di Marzo, Y. Qiao, and P. Tartarini** (1996). Effect of liquid-solid contact angle on droplet evaporation. *Fire Safety Journal*, **27**(2), 141 – 158. ISSN 0379-7112.
19. **Chatzikyriakou, D., S. Walker, C. Hale, and G. Hewitt** (2011). The measurement of heat transfer from hot surfaces to non-wetting droplets. *International journal of heat and mass transfer*, **54**(7), 1432–1440.
20. **Chatzikyriakou, D., S. P. Walker, G. F. Hewitt, C. Narayanan, and D. Lakehal** (2009). Comparison of measured and modelled droplet – hot wall interactions. *Applied Thermal Engineering*, **29**(7), 1398–1405.
21. **Chen, Y., W. Hu, J. Wang, F. Hong, and P. Cheng** (2017). Transient effects and mass convection in sessile droplet evaporation: The role of liquid and substrate thermophysical properties. *International Journal of Heat and Mass Transfer*, **108**, 2072–2087.
22. **Cui, Q., S. Chandra, and S. McCahan** (2001). The effect of dissolving gases or solids in water droplets boiling on a hot surface. *Journal of heat transfer*, **123**(4), 719–728.
23. **Di Marzo, M. and D. D. Evans** (1989). Evaporation of a water droplet deposited on a hot high thermal conductivity surface. *Journal of Heat Transfer*, **111**(1), 210–213.
24. **D.V.Zaitsev, D. P. Kirichenko, V. S. Ajaev, and O. A. Kabov** (2017). Levitation and self-organization of liquid microdroplets over dry heated substrates. *Physical review letters*, **119**(9), 094503.
25. **E.Teodori, P. Pontes, A. Moita, and A. Moreira** (2018). Thermographic analysis of interfacial heat transfer mechanisms on droplet/wall interactions with high temporal and spatial resolution. *Experimental Thermal and Fluid Science*, **96**, 284–294.
26. **Francois, M. and W. Shyy** (2003). Computations of drop dynamics with the immersed boundary method, part 2: Drop impact and heat transfer. *Numerical Heat Transfer, Part B: Fundamentals*, **44**(2), 119–143.
27. **Fujimoto, H., T. Ogino, H. Takuda, and N. Hatta** (2001). Collision of a droplet with a hemispherical static droplet on a solid. *International journal of multiphase flow*, **27**(7), 1227–1245.
28. **Fujimoto, H., A. Y. Tong, and H. Takuda** (2008). Interaction phenomena of two water droplets successively impacting onto a solid surface. *International Journal of Thermal Sciences*, **47**(3), 229 – 236. ISSN 1290-0729.

29. **Fukai, J., Y. Shiiba, T. Yamamoto, O. Miyatake, D. Poulikakos, C. Megaridis, and Z. Zhao** (1995). Wetting effects on the spreading of a liquid droplet colliding with a flat surface: experiment and modeling. *Physics of Fluids*, **7**(2), 236–247.
30. **Fukai, J., Z. Zhao, D. Poulikakos, C. M. Megaridis, and O. Miyatake** (1993). Modeling of the deformation of a liquid droplet impinging upon a flat surface. *Physics of Fluids A: Fluid Dynamics*, **5**(11), 2588–2599.
31. **Ge, Y. and L.-S. Fan** (2006). 3-d modeling of the dynamics and heat transfer characteristics of subcooled droplet impact on a surface with film boiling. *International Journal of Heat and Mass Transfer*, **49**(21), 4231 – 4249. ISSN 0017-9310.
32. **Gumulya, M., R. P. Utikar, V. Pareek, M. O. Tade, S. Mitra, and G. M. Evans** (2014). Modelling of the interaction between a falling n-heptane droplet and hot solid surface. *Chemical Engineering Science*, **116**, 23–37.
33. **Hardt, S. and F. Wondra** (2008). Evaporation model for interfacial flows based on a continuum-field representation of the source terms. **227**, 5871–5895.
34. **Harlow, F. H. and J. P. Shannon** (1967). The splash of a liquid drop. *Journal of Applied Physics*, **38**(10), 3855–3866.
35. **Healy, W., J. Hartley, and S. Abdel-Khalik** (2001). On the validity of the adiabatic spreading assumption in droplet impact cooling. *International Journal of Heat and Mass Transfer*, **44**(20), 3869 – 3881. ISSN 0017-9310.
36. **Herbert, S., S. Fischer, T. Gambaryan-Roisman, and P. Stephan** (2013a). Local heat transfer and phase change phenomena during single drop impingement on a hot surface. *International Journal of Heat and Mass Transfer*, **61**(1), 605–614.
37. **Herbert, S., T. Gambaryan-Roisman, and P. Stephan** (2013b). Influence of the governing dimensionless parameters on heat transfer during single drop impingement onto a hot wall. *Colloids and Surfaces A: Physicochemical and Engineering Aspects*, **432**, 57–63.
38. **Holman, J., P. Jenkins, and F. Sullivan** (1972). Experiments on individual droplet heat transfer rates. *International Journal of Heat and Mass Transfer*, **15**(8), 1489 – 1495. ISSN 0017-9310.
39. **Josserand, C. and S. Thoroddsen** (2016). Drop impact on a solid surface. *Annual Review of Fluid Mechanics*, **48**(1), 365–391.
40. **Jung, J., S. Jeong, and H. Kim** (2016). Investigation of single-droplet/wall collision heat transfer characteristics using infrared thermometry. *International Journal of Heat and Mass Transfer*, **92**, 774–783.
41. **Kabov, O. A., D. V. Zaitsev, D. P. Kirichenko, and V. S. Ajaev** (2017). Interaction of levitating microdroplets with moist air flow in the contact line region. *Nanoscale and microscale thermophysical engineering*, **21**(2), 60–69.
42. **Kandlikar, S. and M. Steinke**, High speed photographic investigation of liquid-vapor interface and contact line movement during CHF and transition boiling. volume 369. 2001.

43. **Ko, Y. S. and S. H. Chung** (1996). An experiment on the breakup of impinging droplets on a hot surface. *Experiments in Fluids*, **21**(2), 118–123. ISSN 1432-1114.
44. **Kunkelmann, C. and P. Stephan** (2009). Cfd simulation of boiling flows using the volume-of-fluid method within openfoam. *Numerical Heat Transfer, Part A: Applications*, **56**(8), 631–646.
45. **Kunkelmann, C. and P. Stephan** (2010). Numerical simulation of the transient heat transfer during nucleate boiling of refrigerant hfe-7100. *International Journal of Refrigeration*, **33**(7), 1221–1228.
46. **Kwon, H.-m., J. C. Bird, and K. K. Varanasi** (2013). Increasing Leidenfrost point using micro-nano hierarchical surface structures. *Applied Physics Letters*, **103**(20), 201601.
47. **Lee, J., J. Kim, and K. T. Kiger** (2001). Time-and space-resolved heat transfer characteristics of single droplet cooling using microscale heater arrays. *International Journal of Heat and Fluid Flow*, **22**(2), 188–200.
48. **Liang, G. and I. Mudawar** (2017). Review of drop impact on heated walls. *International Journal of Heat and Mass Transfer*, **106**, 103 – 126. ISSN 0017-9310.
49. **Limbeek, M. A. V., M. Shirota, P. Sleutel, C. Sun, A. Prosperetti, and D. Lohse** (2016). Vapour cooling of poorly conducting hot substrates increases the dynamic Leidenfrost temperature. *International Journal of Heat and Mass Transfer*, **97**, 101 – 109. ISSN 0017-9310.
50. **Liu, H., E. J. Lavernia, and R. H. Rangel** (1993). Numerical simulation of substrate impact and freezing of droplets in plasma spray processes. *Journal of Physics D: Applied Physics*, **26**(11), 1900.
51. **Lunkad, S. F., V. V. Buwa, and K. Nigam** (2007). Numerical simulations of drop impact and spreading on horizontal and inclined surfaces. *Chemical Engineering Science*, **62**(24), 7214 – 7224. 8th International Conference on Gas-Liquid and Gas-Liquid-Solid Reactor Engineering.
52. **Marengo, M., C. Antonini, I. V. Roisman, and C. Tropea** (2011). Drop collisions with simple and complex surfaces. *Current Opinion in Colloid and Interface Science*, **16**(4), 292 – 302. ISSN 1359-0294.
53. **Marzo, M. D., P. Tartarini, Y. Liao, D. Evans, and H. Baum** (1993). Evaporative cooling due to a gently deposited droplet. *International Journal of Heat and Mass Transfer*, **36**(17), 4133 – 4139. ISSN 0017-9310.
54. **McGinnis, F. and J. Holman** (1969). Individual droplet heat-transfer rates for splattering on hot surfaces. *International Journal of Heat and Mass Transfer*, **12**(1), 95 – 108. ISSN 0017-9310.
55. **Minamikawa, T., H. Fujimoto, T. Hama, and H. Takuda** (2008). Numerical simulation of two droplets impinging successively on a hot solid in the film boiling regime. *ISIJ International*, **48**(5), 611–615.
56. **Minas, L. and B. Ellison**, *Energy efficiency for information technology: How to reduce power consumption in servers and data centers*. Intel Press, 2009.

57. **Moreira, A., A. Moita, and M. Panão** (2010). Advances and challenges in explaining fuel spray impingement: How much of single droplet impact research is useful? *Progress in Energy and Combustion Science*, **36**(5), 554 – 580. ISSN 0360-1285.
58. **Mundo, C., M. Sommerfeld, and C. Tropea** (1995). Droplet-wall collisions: experimental studies of the deformation and breakup process. *International journal of multiphase flow*, **21**(2), 151–173.
59. **Naber, J. D. and P. V. Farrell**, Hydrodynamics of droplet impingement on a heated surface. *In SAE Technical Paper*. SAE International, 1993.
60. **Nakoryakov, V., S. Misyura, and S. Elistratov** (2012). The behavior of water droplets on the heated surface. *International Journal of Heat and Mass Transfer*, **55**(23), 6609 – 6617. ISSN 0017-9310.
61. **Nikolopoulos, N., A. Theodorakakos, and G. Bergeles** (2007). A numerical investigation of the evaporation process of a liquid droplet impinging onto a hot substrate. *International Journal of Heat and Mass Transfer*, **50**(1), 303–319.
62. **Okawa, T., K. Nagano, and T. Hirano** (2012). Boiling heat transfer during single nanofluid drop impacts onto a hot wall. *Experimental Thermal and Fluid Science*, **36**, 78 – 85. ISSN 0894-1777.
63. **Pasandideh-Fard, M., S. Aziz, S. Chandra, and J. Mostaghimi** (2001). Cooling effectiveness of a water drop impinging on a hot surface. *International Journal of Heat and Fluid Flow*, **22**(2), 201 – 210. ISSN 0142-727X.
64. **Pasandideh-Fard, M., Y. Qiao, S. Chandra, and J. Mostaghimi** (1996). Capillary effects during droplet impact on a solid surface. *Physics of fluids*, **8**(3), 650–659.
65. **Pattamatta, A., M. Freystein, and P. Stephan** (2014). A parametric study on phase change heat transfer due to Taylor-Bubble coalescence in a square minichannel. *International Journal of Heat and Mass Transfer*, **76**, 16–32.
66. **Pedersen, C.** (1970). An experimental study of the dynamic behavior and heat transfer characteristics of water droplets impinging upon a heated surface. *International Journal of Heat and Mass Transfer*, **13**(2), 369 – 381. ISSN 0017-9310.
67. **Potash, M. and P. Wayner** (1972). Evaporation from a two-dimensional extended meniscus. *International Journal of Heat and Mass Transfer*, **15**(10), 1851 – 1863.
68. **Prosperetti, A. and H. N. Oguz** (1993). The impact of drops on liquid surfaces and the underwater noise of rain. *Annual Review of Fluid Mechanics*, **25**(1), 577–602.
69. **Qiao, Y. M. and S. Chandra** (1997). Experiments on adding a surfactant to water drops boiling on a hot surface. *Proceedings of the Royal Society of London. Series A: Mathematical, Physical and Engineering Sciences*, **453**(1959), 673–689.
70. **Raj, R., C. Kunkelmann, P. Stephan, J. Plawsky, and J. Kim** (2012). Contact line behavior for a highly wetting fluid under superheated conditions. *International Journal of Heat and Mass Transfer*, **55**(9), 2664 – 2675.
71. **Rein, M.** (1993). Phenomena of liquid drop impact on solid and liquid surfaces. *Fluid Dynamics Research*, **12**(2), 61 – 93. ISSN 0169-5983.

72. **Rioboo, R., C. Tropea, and M. Marengo** (2001). Outcomes from a drop impact on solid surfaces. *Atomization and sprays*, **11**(2).
73. **Ruiz, O. E. and W. Z. Black** (2002). Evaporation of water droplets placed on a heated horizontal surface. *Journal of heat transfer*, **124**(5), 854–863.
74. **Schneider, C. A., W. S. Rasband, and K. W. Eliceiri** (2012). NIH image to imagej: 25 years of image analysis. *Nature methods*, **9**(7), 671.
75. **Schremb, M., S. Borchert, E. Berberovic, S. Jakirlic, I. V. Roisman, and C. Tropea** (2017). Computational modelling of flow and conjugate heat transfer of a drop impacting onto a cold wall. *International Journal of Heat and Mass Transfer*, **109**, 971 – 980.
76. **Schweizer, N.** (2010). *Multi-Scale Investigation of Nucleate Boiling Phenomena in Microgravity*. Ph.D. thesis, Technische Universität, Darmstadt.
77. **Šikalo, Š., H. D. Wilhelm, I. V. Roisman, S. Jakirlić, and C. Tropea** (2005). Dynamic contact angle of spreading droplets: Experiments and simulations. *Physics of Fluids*, **17**(6), 1–13.
78. **Staat, H. J. J., T. Tran, B. Geerdink, G. Riboux, C. Sun, J. M. Gordillo, and D. Lohse** (2015). Phase diagram for droplet impact on superheated surfaces. *Journal of Fluid Mechanics*, **779**, R3.
79. **Stephan, P. and C. Busse** (1992). Analysis of the heat transfer coefficient of grooved heat pipe evaporator walls. *International Journal of heat and mass transfer*, **35**(2), 383–391.
80. **Strotos, G., M. Gavaises, A. Theodorakakos, and G. Bergeles** (2008a). Numerical investigation of the cooling effectiveness of a droplet impinging on a heated surface. *International Journal of Heat and Mass Transfer*, **51**(19), 4728 – 4742. ISSN 0017-9310.
81. **Strotos, G., M. Gavaises, A. Theodorakakos, and G. Bergeles** (2008b). Numerical investigation on the evaporation of droplets depositing on heated surfaces at low Weber numbers. *International Journal of Heat and Mass Transfer*, **51**(7), 1516 – 1529. ISSN 0017-9310.
82. **Tarozzi, L., A. Muscio, and P. Tartarini** (2007). Experimental tests of dropwise cooling on infrared-transparent media. *Experimental Thermal and Fluid Science*, **31**(8), 857 – 865. ISSN 0894-1777.
83. **Tran, T., H. J. J. Staat, A. Prosperetti, C. Sun, and D. Lohse** (2012). Drop impact on superheated surfaces. *Phys. Rev. Lett.*, **108**, 036101.
84. **Tryggvason, G., B. Bunner, A. Esmaeeli, D. Juric, N. Al-Rawahi, W. Tauber, J. Han, S. Nas, and Y.-J. Jan** (2001). A Front-Tracking Method for the Computations of Multiphase Flow. *Journal of Computational Physics*, **169**(2), 708–759.
85. **Villegas, L. R., R. Alis, M. Lepilliez, and S. Tanguy** (2016). A ghost fluid/level set method for boiling flows and liquid evaporation: Application to the leidenfrost effect. *Journal of Computational Physics*, **316**, 789 – 813.

86. **Villegas, L. R., S. Tanguy, G. Castanet, O. Caballina, and F. Lemoine** (2017). Direct numerical simulation of the impact of a droplet onto a hot surface above the leidenfrost temperature. *International Journal of Heat and Mass Transfer*, **104**, 1090 – 1109.
87. **Wakefield, J., C. F. Tilger, and M. A. Oehlschlaeger** (2016). The interaction of falling and sessile drops on a hydrophobic surface. *Experimental Thermal and Fluid Science*, **79**, 36–43.
88. **Wang, A.-B., C.-H. Lin, and C.-C. Chen** (2000). The critical temperature of dry impact for tiny droplet impinging on a heated surface. *Physics of Fluids*, **12**(6), 1622–1625.
89. **Wang, A.-B., C.-H. Lin, and C.-C. Cheng** (2005). Pattern analysis of a single droplet impinging onto a heated plate. *Heat Transfer Asian Research*, **34**(8), 579–594.
90. **Xiong, T. and M. Yuen** (1991). Evaporation of a liquid droplet on a hot plate. *International Journal of Heat and Mass Transfer*, **34**(7), 1881 – 1894. ISSN 0017-9310.
91. **Yarin, A.** (2006). Drop impact dynamics: Splashing, spreading, receding, bouncing. *Annual Review of Fluid Mechanics*, **38**(1), 159–192.
92. **Yarin, A. and D. Weiss** (1995). Impact of drops on solid surfaces: self-similar capillary waves, and splashing as a new type of kinematic discontinuity. *Journal of fluid mechanics*, **283**, 141–173.

LIST OF PUBLICATIONS BASED ON THE RESEARCH

Papers in Refereed Journals

1. **Guggilla, G.**, A. Pattamatta and R. Narayanaswamy (2018). Numerical investigation into the evaporation dynamics of drop-on-drop collisions over heated wetting surfaces. *International Journal of Heat and Mass Transfer*, 123, 1050-1067.
2. **Guggilla, G.**, R. Narayanaswamy and A. Pattamatta (2020). An experimental investigation into the spread and heat transfer dynamics of a train of two concentric impinging droplets over a heated surface. *Experimental Thermal and Fluid Science*, 110, 109916.

Presentations in Conferences

1. **Ganesh Guggilla**, Arvind Pattamatta and R. Narayanaswamy, Numerical investigation into evaporation dynamics of drop-on-drop collision over a heated surface, *24th National and 2rd ISHMT–ASTFE Heat and Mass Transfer Conference*, BITS Pilani, India, 27-30 December, 2017.
2. **Ganesh Guggilla**, Arvind Pattamatta and R. Narayanaswamy, Numerical evaluation of contact angle models for single droplet impingement over superheated surfaces, *Proceedings of the 11th Australasian Heat and Mass Transfer Conference (AHMTC11)*, RMIT University, Melbourne, Australia, 9-10 July, 2018.
3. **Ganesh Guggilla**, Arvind Pattamatta and R. Narayanaswamy, Heat transfer characteristics of droplet-jet interactions over a hot surface: From Film evaporation to LeidenFrost Point, *ASME - IMECE (International Mechanical*

Engineering Congress and Exposition), Salt lake city, Utah, U.S.A, 8-14 November, 2019.

4. **Ganesh Guggilla**, Arvind Pattamatta and R. Narayanaswamy, A parametric study of experimental investigation into spread and evaporation dynamics of droplet train impingement over a heated surface, *25th National and 3rd International ISHMT-ASTFE Heat and Mass Transfer Conference*, IIT Roorkee, India, 28-31, December, 2019.

CURRICULUM VITAE

1. **NAME** : Guggilla Ganesh
2. **DATE OF BIRTH** : 1, July 1992
3. **EDUCATIONAL QUALIFICATION**

2013 BACHELOR OF TECHNOLOGY (B.Tech)

Institution : JNTUH college of Engineering, Jagtial, Telangana
Specialization : Mechanical Engineering

MASTER OF SCIENCE & DOCTOR OF PHILOSOPHY (M.S & Ph.D)

Institution : Indian Institute of Technology Madras, Tamil Nadu
Specialization : Mechanical Engineering
Registration date : 06, January 2015

DOCTOR OF PHILOSOPHY (Ph.D)

Joint Doctoral Programme
Institution : Curtin University, Western Australia
Specialization : Mechanical Engineering
Registration date : 01, July 2017

DOCTORAL COMMITTEE

CHAIRPERSON

Dr. N. Ramesh Babu,
Professor and Head,
Department of Mechanical Engineering,
IIT Madras.

GUIDE

Dr. Arvind Pattamatta,
Associate Professor,
Department of Mechanical Engineering,
IIT Madras.

Dr. Ramesh Narayanaswamy,
Associate Professor,
Department of Mechanical Engineering,
Curtin University

MEMBERS

Dr. Sateesh Gedupudi,
Assistant Professor,
Department of Mechanical Engineering,
IIT Madras.

Dr. Srikrishna Sahu,
Assistant Professor,
Department of Mechanical Engineering,
IIT Madras.

Dr. Prasad Patnaik B.S.V.,
Professor,
Department of Applied Mechanics,
IIT Madras.